DEFORMATION AND RUPTURE OF CYLINDRICAL SHELLS UNDER DYNAMIC LOADING

by

Michelle S. Hoo Fatt
S.B. in Mechanical Engineering, Massachusetts Institute of Technology (1987)
S.M. in Ocean Engineering, Massachusetts Institute of Technology (1990)

Submitted to the Department of Ocean Engineering
in partial fulfillment of the requirements for the degree of

Doctor of Philosophy in the field of Structural Mechanics

at the

MASSACHUSETTS INSTITUTE OF TECHNOLOGY

June 1992

Signature redacted

Author .....
Department of Ocean Engineering
June 12, 1992

Certified by ..... Signature redacted .....
Professor Tomasz Wierzbicki
Professor
Thesis Supervisor

Accepted by ..... Signature redacted .....
A. Douglas Carmichael
Chairman, Departmental Committee on Graduate Students

DEFORMATION AND RUPTURE OF CYLINDRICAL SHELLS UNDER DYNAMIC LOADING

by

Michelle S. Hoo Fatt

S.B. in Mechanical Engineering, Massachusetts Institute of Technology (1987)

S.M. in Ocean Engineering, Massachusetts Institute of Technology (1990)

Submitted to the Department of Ocean Engineering
on June 12, 1992, in partial fulfillment of the
requirements for the degree of
Doctor of Philosophy in the field of Structural Mechanics

Abstract

The dynamic plastic response and failure of unstiffened and ring-stiffened cylindrical shells subjected to dynamic loads were studied. The proposed solution methodology, based on a simple computational model of the shell and the concept of equivalence parameters, incorporated two main load-resisting mechanisms in the shell: stretching in the longitudinal direction and bending in the circumferential direction. From this method, the complicated two-dimensional cylindrical shell problem was reduced to a one-dimensional problem of a string-on-foundation. In particular, the magnitude of the transient and final shape of the transverse deflections of the shell undergoing impact and explosive-type loading were predicted. In order to predict shell failure, the solution for the transient deflection was coupled with a simple fracture criterion - the critical strain to rupture. Both exact and approximate solutions for the impact and impulsive loading of the unstiffened shell were compared and gave similar results for high velocity impact and impulsive loading. In the ring-stiffened shell, the overall deflection profile was shown to consist of both a global and local (between stiffeners) deflection fields thereby revealing a complex interplay between the stiffener and the bay. Furthermore, a parametric study on the stiffened shell showed that string-on-foundation model for which ring-stiffeners are represented by lumped masses and springs is a promising method of analyzing the structure.

Thesis Supervisor: Professor Tomasz Wierzbicki
Title: Professor

Dedication

I dedicate this thesis to two women: my mother and Row Selman.

Acknowledgement

There are many people who I need to acknowledge, but the most important one of them all is my advisor and mentor, Tom Wierzbicki. Despite the fact that most of our time was spent arguing, I was very fortunate to have met and worked with such a unique person. I have never learned (and probably will never learn) as much from anyone as I did from Tom Wierzbicki. To me, he remains one of the greatest teacher of all time!

Although I did not get to work closely with him until the very end, I would also like to acknowledge Professor Frank McClintock for pointing out inconsistencies where they appear and teaching me of even better ways of writing technical information. It is not often that one gets the attention of an engineering professor who is not only skilled in mechanics but also in the art of writing, and for this reason I am lucky.

I thank Mr. William McDonald and Dr. Minos Moussouros of the Naval Surface Warfare Center (White Oak) for providing both financial and educational support that was needed to keep this research ongoing. In particular, I dearly acknowledge Minos for supervising my work on both the dimple ring model and the contribution of the shear work rate. The research was supported by the Office of Naval Research under Contract No. N000 14-89-C-0301.

During my Ph.D. studies and the development of the thesis, I had the privilege of working with three other people, Professor R. Rosales (Applied Mathematics Department, MIT), Dr. Ion Suliciu, and Dr. Miheala Suliciu (both from the Institute of Mathematics of the Romanian Academy, Romania). Through our meetings and heated discussions, I was able to obtain some knowledge about non-linear wave mechanics and its application to plasticity. The impact of these three people on my work will become more evident when reading the thesis.

I would also like to thank Professor Norman Jones (University of Liverpool), Professor Steve Reid (UMIST), and Dr. Bill Stronge (Cambridge University) who were kind enough to allow me to visit their respective universities. By learning of their work, I was able to return to MIT with the valuable information needed to solve some of the problems presented in this thesis.

Finally, I would also like to acknowledge some very important people: Professor T. Francis Ogilvie, Row Selman, Muriel Bernier, and Judi Sheytanian. The final semester of Ph.D. studies was an unbearable time for me and without the critical advice from these people, I do not think I could of made it out in one piece. (Actually, I'm not sure I did.)

Contents

List of Figures

List of Tables

NOMENCLATURE

$c = \sqrt{\sigma_o/\rho}$ transverse wave speed

$\tilde{f} = \bar{T}/(\bar{q}l_c)$ normalized shear force

h plate thickness

h_b equivalent bending plate thickness

h_i equivalent inertia plate thickness

h_{NA} neutral axis

$2l$ length between bays

l_1, l_2 lengths to divide bay and stiffener

l_c characteristic length for normalization

l_o length between stationary hinges

$m = \rho h$ mass per unit area of cylinder

$\bar{m}$ equivalent mass per unit length

n integers

p pressure load

$\bar{p}$ equivalent line load

p_o pressure load amplitude

$\bar{q}$ bending resistance per unit length

r radial component

r_p radius of projectile

t time

t_f response time

u axial deformation

u_i components of displacements vector

v tangential displacement

w transverse or radial deflection

w_f final transverse deflection

x axial coordinate

$x_o = \bar{N}/\bar{q}$ characteristic length

z through thickness coordinate

$\dot{W}$ work rate

$\bar{F}$ axial force

F_n, G_n, H_n coefficients of eigenvalue expansion terms

$\bar{I}$ impulse

$\bar{I}_c$ critical impulse to rupture

$2L$ extent of pressure load

$\bar{M}$ stiffener mass

M_b total bending moment

M_c characteristic mass

M_o impacting mass

M_{pl} fully plastic bending moment

$M_{\alpha\beta}$ bending moment tensor

$\bar{N}$ equivalent tensile force

N_{pl} fully plastic membrane force

$N_{\alpha\beta}$ membrane force tensor

$\bar{Q}$ stiffener bending resistance

R shell radius

$\bar{T}$ shear force

T_i surface traction

$\bar{V}$ impulse velocity

V_c characteristic velocity

V_o impact velocity

α_o fixed hinge angle

β hinge angle

$\gamma = (c\bar{q}M_o)/(4\bar{m}\bar{N}V_o)$ critical parameter for impact

δ_f final central deflection

δ_g global central deflection

δ_l local central deflection

ϵ strain

ϵ_{av} average strain

ϵ_c critical rupture strain

ϵ_{max} maximum strain

θ circumferential coordinate

$\zeta = \bar{Q}/(\bar{q}l_c)$ stiffness ratio

$\eta = M_c/(\bar{m}l_c)$ mass ratio

Θ integrals in the circumferential coordinate

κ curvature

λ_n eigenvalues

$\mu = l_1/l_2$ length ratio

$\nu = V_c/c$ velocity ratio

2ξ length of deformed zone

$2\xi_f$ final length of deformed zone

ρ material density

σ stress

σ_o flow stress

τ decay constant

ϕ hinge angle

Ω jump in rotation

$\dot{()}$ *or* $()_t$ time derivative

$()'$ *or* $()_x$ derivative with respect to x

$\tilde{()}$ normalized quantity

$\bar{()}$ quantity integrated in θ-direction

Chapter 1

Introduction

Accurate predictions of the dynamic plastic deformation and rupture of unstiffened and stiffened cylindrical shells subjected to high intensity transient loading are of great importance in many industrial applications. In the offshore industry, for instance, tubular members such as the corner legs or bracing element of drilling platforms may undergo local damage due to collisions with supply vessels or dropped object impact. Nuclear and chemical industries are interested in the safety of piping systems and pressure/containment vessels subjected to accidental pressure burst, pipe whipping, or missile impact. Research in submarine survivability against underwater explosion is actively pursued by the defense industry. Finally, the aerospace industry is interested in limiting or containing damage that may occur to transport aircraft fuselages, rockets or space stations caused by different types of accidental loads.

Early research on dynamic buckling and failure of cylinders was restricted to axi-symmetric external radial pulse loading [1]. The corresponding analysis, however, is of limited applicability because axi-symmetric dynamic loading seldom occurs in practice. In real world situations loading is usually applied to one side of the cylinder and is characterized by various degrees of locality. It may consist of a projectile, missile or mass impact, stand-off explosion described by a pressure pulse or contact explosion which can be often approximated as an ideal impulsive loading.

Depending on the load intensity and the spatial distribution of contact pressures, various forms of damage may result ranging from large amplitude lateral deflections to

punch-through penetration, fracture initiation at the base plate or the so-called stiff interfaces (clamped boundaries/base of stiffeners) [2], progression of tearing fracture, and finally massive structural damage. Damage to stiffeners themselves may include tripping failure (lateral plastic instability) [3] and detachment from the base plate. With still increasing load intensity, fragmentation of the shell will occur [4]. Due to the complexities introduced by unsymmetric loading and the large displacements and rotations of the shell amplified by material nonlinearities, the problem does not easily lend itself to an analytical treatment. However, by introducing a suitable set of assumptions a simple and realistic shell model can be developed that captures two dominant deformation mechanisms in locally loaded shells: axial stretching and circumferential bending of a shell element. The model can be interpreted as a rigid-plastic string resting on rigid-plastic foundation in which the two mechanisms are present in the form of plastic axial resistance of the string and foundation resistance, respectively. This model will be shown to be very effective and powerful in solving a class of engineering problems involving impact and explosive loading. Over the past few years a great deal of credibility has been added to the model by showing that theoretically predicted deflection profiles and amount of structural damage agrees with experimental data [5, 6, 7].

Finding a closed-form analytical solution for the shell under large deflection non-symmetric loading is mathematically complex. Moreover, the case of pressure loading on a ring-stiffened shell is further complicated by ring-stiffeners, which may undergo tripping and fracture during the explosion. Because of the difficulties in finding closed-form solutions to a set of coupled shell differential equations, past researchers have resorted to using empirical methods [8] or by using computer codes [9]. Solutions for the elastic response of the unstiffened shell due to pressure loads have been found [10, 11, 12, 13, 14, 15], but very little has been done in addressing the plastic response of the shell [16, 17]. Moreover, Huang [18] and Geers [19, 20] have furnished analytical solutions to the linear elastic fluid-solid response of a submerged, infinite, circular cylindrical shell excited by transient acoustic waves. Geers and Yen [21] attempted to find the underwater inelastic response of a cylindrical shell by setting it up as a fluid-

solid interaction and using the finite element method (FEM) to model the structural behavior and the boundary element method (BEM) to model the surrounding fluid.

This thesis is concerned with the dynamic plastic response and failure of a cylindrical shell subjected to several types of localized dynamic loading. Based on justifiable assumptions on the rate of internal energy dissipation of the shell, an analytical solution for the shell deformation is found by developing a simple computational model. In particular, three specific problems will be analyzed in detail: (i) mass impact on metal tubes; (ii) pressure pulse loading of a stiffened cylinder; (iii) impulsive loading of a ring-stiffened shell. Parametric studies are performed on each solution and where possible, theoretical predictions are compared to experimental data.

Chapter 2

Literature Review

Literature on the transient response of cylinders to impact and impulsive loading is limited but has been rapidly growing over the past five years. Gefken [22] extended the earlier analysis by Lindberg and Florence [1] to one-sided inward radial pressure that varied as the cosine of the angular position around the shell and was uniform along the length. Experiments performed on short, fully clamped shells revealed that the response modes consisted of dynamic wrinkling in the hoop direction followed by large inward deflections of the shell. This type of behavior is characteristic for shells that are quite thin (radius to thickness ratio, $R/h = 240$).

Thicker shells or thin shells reinforced by ring stiffeners develop a single dent without any wrinkling. For example, local dimple deformation of thicker tubes ($R/h < 40$) subjected to missile impact were described by Stronge [23] and Corbett et al [24] and compared to static deflection under punch loading. Localization of plastic deformation was observed with increasing impact velocity.

Over the last few years general purpose nonlinear finite element codes were used to model and solve a class of dynamic shell problems. A successful application of DYNA-3D computer code was reported by Kirkpatrick and Holmes [25] and Prantil et al [26]. Work at the Stanford Research Institute over the last five years has recently been summarized by Holmes and Kirkpatrick [27]. Trinh and Gruda [28] presented a solution of a projectile impact problem on a cylindrical shell. The incorporation of a continuous damage model to DYNA-3D code opened a possibility of predicting

failure initiation and progression of fracture in thin cylinders and other structures [29].

Parallel to numerical studies, an entirely new and promising line of research has emerged based on the modeling of a cylindrical shell as a plastic string resting on plastic foundation. The analogy between a cylindrical shell under axisymmetric loading and a beam-on-foundation originated in elastic shell theory [30]. In 1977, the model was re-discovered by Calladine [31] in order to address problems of non-axisymmetric loading of elastic spherical and cylindrical shells. Then shortly after this, Reid [32] extended the beam-on-foundation model into the plastic range by studying the pinching of rigid-plastic tubes. Even more recently, Yu and Stronge [33, 34] used the beam-on-foundation model to calculate the deformation of a cylindrical shell undergoing projectile impact. To accommodate that class of problems for which the central deflection of the shell is of the order several times the shell thickness, it is proposed to extend the beam-on-foundation model even further into the plastic range so that the analogy is now made between a cylindrical shell and a string-on-foundation. Gurkok and Hopkins [35] have shown that finite deformations cause significant geometrical changes in a fixed rigid-plastic beam under transverse loads. When the central deflection of the beam is of the order of its thickness, membrane forces predominate thereby enhancing the beams load carrying capacity and rendering the beam to behave like a string (membrane state). The rigid-plastic cylindrical shell undergoing moderately large deflection would therefore behave more like a string-on-foundation rather than a beam-on-foundation.

The dynamic response of the plastic string (without foundation) was extensively studied during and after World War II [36, 37]. However, apart from the problem of the aircraft impact on a balloon barrage cable, no other practical applications of these solutions were found. The addition of a plastic foundation constant to the string has put the model in an entirely new perspective. While the string represents the average weighted axial strength of a shell, the foundation describes the shell resistance to lateral crushing. With the two major force-resisting mechanisms of the cylinder included in the formulation, the string-on-foundation appears to be a realistic (when

compared to experimental results) shell model for a variety of dynamic problems.

Mathematically the string-on-foundation problem is described by an inhomogeneous wave equation which due to the rigid-plastic assumption is subjected to nonlinear loading/unloading condition. Many interesting features of the initial value problems for this equation are revealed in recent publications. An exact solution to the inhomogeneous wave equation under mass impact boundary condition, recently derived by Rosales et al [38] using the method of characteristics, serves as a benchmark solution to various approximate solutions and also helps determine the range of validity of these approximations. In a study of projectile impact on a cylindrical shell, Wierzbicki and Hoo Fatt [39] used the exact results of the velocity field, a new concept of a propagating extensional hinge and the principle of conservation of linear momentum to predict the ballistic limit of the shell. The general methodology was subsequently used to predict the permanent damage that results from a drill-collar accidently falling on one of the tubular members of an offshore platform [40]. In the higher velocity range the theoretical maximum deflections calculated by Wierzbicki and Hoo Fatt [39] were shown to agree with experimental profiles measured by Stronge [23]. The theory has also been successfully used in finding the ballistic limit and post-perforation velocity for projectile impact into circular plates [7, 41]. Theoretical predictions of the ballistic limit were found to be within 10 percent of experimental results for thin aluminum and steel plates.

The string-on-foundation model has also been also used to analyze local plastic damage up to fracture of cylinders subjected to explosive loading. Suliciu et al [42] derived a closed form solution for the large amplitude transient shell response subjected to an exponentially decaying pressure pulse and an ideal impulse loading distributed as a cosine square function along the axis of the cylinder. Static strength and deformations of ring stiffened shells were studied by Onoufriou and Harding [43], Onoufriou et al [44], Ronalds and Dowling [45] and Hoo Fatt and Wierzbicki [6]. Finally, Hoo Fatt and Wierzbicki formulated and solved approximately the problem of impulsively loaded ring-stiffened shell [46]. The deflection profiles calculated from these solutions were shown to correlate well with limited experimental data, taken

from Reference [47].

In many practical applications, the pressure pulse loading results from an underwater explosion. The problem of fluid-solid interaction has received a great deal of attention in the literature. Most of the results were restricted to elastic response of shells, [18, 19]. More recently Geers and Yen [21] extended the analysis to the inelastic deformations. However, the range of deflections considered by Geers and Yen was by far smaller than the deflection permitted by the beam-on-foundation model. Clearly, more research is needed to close the gap between the technologies developed using large deflection theory without the fluid-solid interaction and that considering the fluid-solid interaction but restricted to small deflections. The analytical solution presented here may be considered as one attempt to form this bridge.

Chapter 3

Problem Formulation

The formulation is kept general so that the proposed methodology may be applied to both the unstiffened and ring-stiffened cylindrical shell subjected to high intensity, localized, dynamic loads - impact, pressure pulse, impulsive. Consider a long cylindrical shell of thickness h, radius R, and mass density ρ as shown in Figure 3-1. If the shell is ring-stiffened, the shell thickness would be a varying function of axial displacement x. Chapter 8 deals with such a shell. However, for simplicity we will represent the general shell as an unstiffened one and show how ring stiffeners are incorporated into the model in Chapter 8. The shell material is idealized as rigid, perfectly-plastic with flow stress σ_o. The cylinder is subjected to an applied pressure load $p(x, \theta, t)$ and undergoes radial deformation $w(x, \theta, t)$, where x, θ denotes the axial and circumferential coordinates and t denotes time. Later it will be seen that the maximum radial deflection becomes transverse deflection of the shell. The maximum amplitude of the transverse deflection is denoted by δ.

For the reader's convenience, the following sections define certain basic quantities and concepts:

Material In the range of moderately large deflection, elastic deformations are negligible compared with plastic deformations. Therefore, the material is assumed to be rigid-perfectly plastic, described by a flow stress σ_o. For an actual work-hardening material, the flow stress is understood as a constant, elevated stress corresponding to

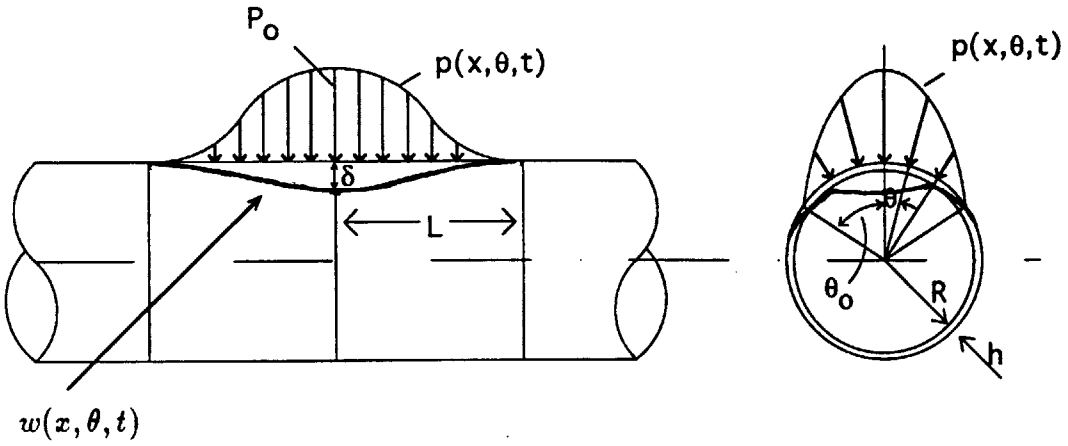

Figure 3-1: Geometry and loading of a cylindrical shell.

an average strain ϵ_{av} in the loading process, $\sigma_o = \sigma(\epsilon_{av})$.

The determination of σ_o requires an iterative procedure in which the problem is first solved to find an average strain, then the magnitude of the flow stress is suitably adjusted to match this average strain.

Loading In general the shell is loaded by an inward radial pressure $p(x, \theta, t)$. The size of the "patch" load is of an order of the shell radius or smaller so that the resulting deformations are highly localized. As shown in Fig. 3-1, the pressure distribution is assumed to have two planes of symmetry, at $x = 0$ and at $\theta = 0$, and a variable amplitude but a fixed shape. The pressure amplitude rises instantaneously to the maximum value p_o and then decays exponentially with a characteristic time constant τ, according to

$$p(x, \theta, t) = p_o e^{-\frac{t}{\tau}} f(x) g(\theta), \tag{3.1}$$

where $f(x)$ and $g(\theta)$ are known, dimensionless shape functions. In the case of impulsive loading, the pressure is taken to be zero and the loading is introduced to the shell through the initial condition for the shell velocity. In impact situations the loading is introduced through both the boundary condition (at the point of impact) and the initial condition (initial velocity at the point of impact). Illustrative examples of each type of loading mentioned above will be given in the subsequent chapters.

Stresses and Strains Corresponding simplifying assumptions on the stresses will be discussed dealing with the rate of internal energy dissipation in the shell.

Assuming plane stress and the Love-Kirchhoff hypothesis,

$$\dot{\epsilon}_{\alpha\beta} = \dot{\epsilon}^0_{\alpha\beta}(x, \theta) + z\dot{\kappa}_{\alpha\beta}(x, \theta), \qquad [\alpha, \beta] = [x, \theta], \tag{3.2}$$

Equilibrium The overall shell equilibrium is expressed via the principle of virtual velocities

$$\dot{W}_{ext} = \dot{W}_{int}, \tag{3.3}$$

where $\dot{W}_{ext}$ is the rate of external work and $\dot{W}_{int}$ is the rate of internal dissipation of energy. Equation (3.3) can be expressed in shell coordinates for which $dS_0 = dx R d\theta$:

$$\bar{F}\dot{u}|_{ends} + \bar{T}\dot{w}|_{ends} + \int_{S_0} T_i \dot{u}_i dS_0 + \int_{S_0} (-m\ddot{u}_i)\dot{u}_i dS_0 = h \int_{S_0} \sigma_{ij}\dot{\epsilon}_{ij} dS_0, \tag{3.4}$$

where the velocity vector are $\dot{u}_i[\dot{u}, \dot{v}, \dot{w}]$ corresponding to the x, θ, r axis, the dot denotes time derivative, $m = \rho h$ is the mass per unit area, σ_{ij} and $\dot{\epsilon}_{ij}$ denote components of stress and strain rate vector, and T_i a vector of surface tractions with components $T_i[0, 0, p]$ in the x, θ, r direction. In addition there may be an axial load $\bar{F}(t)$ applied along the axis of the tube and a concentrated shear load $\bar{T}(t)$ at the ends (the bars on these quantities will later denote quantities that are integrated in the circumferential direction). Notice also that rigid body velocities, $\dot{u}$ and $\dot{w}$, are assumed beyond the plastically deformed region of the shell. Hence the first two terms of Eq. (3.4) are not integrated over the surface area. The radial deflection w can also be interpreted as deflection in the transverse direction (see Fig. 3-1).

It is assumed that $u \equiv 0$. The justification of this approximate assumption follows from the symmetry of the problem $\dot{u}(x = 0) = 0$ and that outside the local deforming region the axial displacement of the shell is zero. Therefore $\dot{u}$ is small in the deforming region and can be neglected compared to the remaining components $\dot{v}$ and $\dot{w}$.
Using the Love-Kirchhoff assumption, Eq. (3.4) reduces to

$$\bar{T}\dot{w}|_{ends} + \int_{S_0} p\dot{w} dS_0 + \int_{S_0} -m(\ddot{w}\dot{w} + \ddot{v}\dot{v}) dS_0 = \int_{S_0} (N_{\alpha\beta}\dot{\epsilon}_{\alpha\beta} + M_{\alpha\beta}\dot{\kappa}_{\alpha\beta}) dS_0, \tag{3.5}$$

where $\dot{\epsilon}_{\alpha\beta}$ and $\dot{\kappa}_{\alpha\beta}$ are the generalized strain and curvature rate tensors, and $N_{\alpha\beta}$ and $M_{\alpha\beta}$ are the corresponding tensors of the membrane force and bending moment.

Here, a Lagrangian formulation is used so that the components of the strains and curvature rate vectors should be calculated in the material description.

For moderately large deflections, certain simplifying assumptions can be made to reduce the internal forces to only the membrane stretching and circumferential bending. These assumptions will be fully explained in the following section.

3.1 Assumptions and Simplifications

Most of our assumptions and simplifications will be concerned with the generalized forces and displacements of the shell and will be valid only for relatively thin shells, $20 < R/h < 150$. The rate of internal work dissipation in the shell is given explicitly by

$$\dot{W}_{int} = 2\int_0^{\xi} 2R \int_0^{\pi} (M_{xx}\dot{\kappa}_{xx} + M_{\theta\theta}\dot{\kappa}_{\theta\theta} + 2M_{x\theta}\dot{\kappa}_{x\theta} + N_{xx}\dot{\epsilon}_{xx} + N_{\theta\theta}\dot{\epsilon}_{\theta\theta} + 2N_{x\theta}\dot{\epsilon}_{x\theta})d\theta dx. \tag{3.6}$$

However, for shells undergoing moderately large deflection, $\delta/R < 0.2$, some of these energy components are negligible. The following simplifications are made in a step-by-step fashion:

1. Experiments show that the shell is can be assumed to be inextensible in the circumferential direction, $\dot{\epsilon}_{\theta\theta} = 0$. (For very thin shells, $R/h > 100$, this would not be the case.) Hence the rate of energy associated with hoop compression or tension is zero.

2. The rate of bending work rate in the axial direction is neglected, $M_{xx}\dot{\kappa}_{xx} = 0$. During early shell deformation, the curvature rate in the axial direction is small, $\dot{\kappa}_{xx} \approx 0$ (this assumption will be re-examined in Chapter 8). When the shell deflections are several time the magnitude of shell thickness, $\dot{\kappa}_{xx}$ increases but the axial bending forces M_{xx} becomes negligible (membrane state). The net result is that $M_{xx}\dot{\kappa}_{xx} = 0$ throughout deformation of the shell.

3. A previous analysis of a tube under knife loading [48] shows that the shear work rate components, $2M_{x\theta}\dot{\kappa}_{x\theta}$ and $2N_{x\theta}\dot{\epsilon}_{x\theta}$, are insignificant in the early stages of deformation, $\delta/R < 0.2$. This theory is further substantiated by previous work done on the crushing of tubes by Wierzbicki and Suh [5] in which the neglect of the shear energy terms led to the over-prediction of the force-deflection relation by some 10-15 percent when compared to experimental data.

   So far with respect to these three assumptions, the rate of internal energy dissipation reduces to

$$\dot{W}_{int} = 2\int_0^{\xi} 2R \int_0^{\pi} (M_{\theta\theta}\dot{\kappa}_{\theta\theta} + + N_{xx}\dot{\epsilon}_{xx}) d\theta dx. \tag{3.7}$$

4. The next assumption pertains to material behavior. A rigid-perfectly plastic, isotropic, and time independent material is assumed. Hence strain-hardening, strain-rate effects, and elastic vibrations are neglected. These effects tend to reduce deflections. The rigid-plastic assumption is further substantiated by the fact that calculations for this class of problem show that the strains are two orders of magnitude greater than the maximum elastic strains that metal shells can tolerate. Any elastic strains are negligible during deformation.

   An average flow stress σ_o, which lies somewhere between the yield and ultimate strength can be used to approximate a strain hardening material. As stated earlier, an iterative scheme by which the flow strength is calculated based on equal area under the stress-strain curve may be used for a more accurate analysis.

5. As in practical applications of limit analysis, a simplified interaction surface is assumed. In a more exact analysis N_{xx} and $M_{\theta\theta}$ are coupled through a yield condition,

$$f(M_{\alpha\beta}, N_{\alpha\beta}) = 0, \tag{3.8}$$

   which is assumed to be a plastic potential for the generalized strain rates

$$\dot{\kappa}_{\alpha\beta} = \dot{\lambda}\frac{\partial f}{\partial M_{\alpha\beta}}, \qquad \dot{\epsilon}_{\alpha\beta} = \dot{\lambda}\frac{\partial f}{\partial N_{\alpha\beta}}, \tag{3.9}$$

where $\dot{\lambda}$ is a proportionality constant. Then together with Eq. (3.9), the first two assumptions, $\dot{\epsilon}_{\theta\theta} = 0$ and $\dot{\kappa}_{xx} = 0$, can be used to express the yield condition in only four independent quantities. Using a yield condition, such as the Huber-Mises yield criterion, the interaction curve would be seen as nonlinear elliptic yield surface in four-dimensional surface. Instead of this complicated interaction surface, a square-type yield locus is assumed such that

$$|M_{\theta\theta}| = M_{pl}, \qquad |N_{xx}| = N_{pl}, \tag{3.10}$$

where $M_{pl} = \sigma_0 h^2/4$ is the fully plastic bending moment per unit length and $N_{pl} = \sigma_0 h$ is the fully plastic axial force per unit length. Thus the stress distributions at each cross-section normal to the principal direction are independent of each other.

Using this final simplification Eq. (3.7) reduces to

$$\dot{W}_{int} = 2\int_0^{\xi} 2R \int_0^{\pi} (|M_{pl}\dot{\kappa}_{\theta\theta}| + |N_{pl}\dot{\epsilon}_{xx}|)d\theta dx. \tag{3.11}$$

The absolute sign is added to ensure that the rate of energy dissipation is always positive, regardless of the sign of $\dot{\kappa}_{\theta\theta}$ or $\dot{\epsilon}_{xx}$.

The two terms on the right hand side of Eq. (3.11) represent the rate of bending energy in the circumferential direction (crushing of rings) and the rate of axial membrane energy (stretching of generators), respectively. In a previous analysis [49], a simplified shell model was built based these two components. The model consists of a series of unconnected rings and a bundle of unconnected generators. The rings and generators are loosely connected, but deformations are compatible.

3.2 Bending Work Rate

Under large plastic deformation of the rings, hinges develop in areas of localized plastic flow. The first term in Eq. (3.11) contains the rate of bending work in both continuous and discontinuous velocity fields. With the inclusion of plastic hinges, the rate of bending work per unit length $\dot{W}_b$ can be explicitly written as

$$\dot{W}_b = 2R \int_0^\pi |M_{pl} \dot{\kappa}_{\theta\theta}| d\theta dx + 2 \sum_i M_{pl}^{(i)} [\Omega]^{(i)}, \tag{3.12}$$

where $[\Omega]^{(i)}$ denotes a jump in the relative rotation rate across a stationary or moving hinge line. Note that the slopes must be continuous at the moving hinge in Eq. (3.12). The conditions for the kinematic continuity at a moving hinge can be found in Reference [50]. Furthermore, only the last term of Eq. (3.12) is used in the development of stationary hinge models.

3.3 Membrane Work Rate

Following moderately large deflection theory, a Lagrangian description of the axial strain rate is given by

$$\dot{\epsilon}_{xx} = \dot{u}' + w'\dot{w}', \tag{3.13}$$

where u is the deformation in the axial direction and the primes denote differentiation with respect to x. However, the cylinder is modeled under fixed end conditions and axial deformations may be neglected: $u = 0$. Substituting this into the expression for membrane work rate $\dot{W}_m$, one gets

$$\dot{W}_m = 2 \int_0^\xi 2R \int_0^\pi |N_{pl} w' \dot{w}'| d\theta dx. \tag{3.14}$$

The following section shows that with the use of equivalent parameters both the bending and membrane work terms can be reduced to a single integral in x.

Chapter 4

String-On-Foundation

The analogy of a cylindrical shell undergoing large plastic deformation and a string-on-foundation will be made here. First, however, the results from the previous chapter is substituted into the statement of global equilibrium

$$\bar{T}\dot{w}|_{ends} + 2\int_0^L 2R\int_0^\pi p(x,\theta,t)\dot{w}(x,\theta,t)d\theta dx = 2\int_0^\xi 2R\int_0^\pi |M_{pl}\dot{\kappa}_{\theta\theta}|d\theta dx + 2\int_0^\xi 2R\int_0^\pi N_{pl}w'\dot{w}'(x,\theta,t)d\theta dx + 2\int_0^\xi 2R\int_0^\pi m(\ddot{w}\dot{w}+\ddot{v}\dot{v})(x,\theta,t)d\theta dx \quad (4.1)$$

where L is the extent of the load on both sides of the symmetry plane. Notice that the thickness h in the ring-stiffened shell will vary in a piece-wise manner along the x-axis so that both M_{pl} and m are in general functions of position x.

4.1 The Concept of Equivalent Parameters

As in previous work [51], integration in the circumferential direction can be performed, provided that the velocity field in the circumferential direction is known. Development of the stationary hinge model not only gives a realistic deformation pattern for the collapse of each ring but it can be used to derive certain kinematic quantities that lend themselves to certain functions which will later on be defined as equivalent parameters. It will be shown that these functions are roughly constant in magnitude.

For this reason they are called equivalent parameters.

Equation (4.1) can be integrated in the θ-direction to give the following:

$$\bar{T}\dot{w}|_{ends} + 2\int_0^L \bar{p}(x,t)\dot{w}(x,t)dx = 2\int_0^{\xi} \bar{q}\dot{w}(x,t)dx + 2\int_0^{\xi} \bar{N}w'\dot{w}'(x,t)dx + 2\int_0^{\xi} \bar{m}\ddot{w}\dot{w}(x,t)dx, \tag{4.2}$$

where the following equivalent functions are introduced:
an equivalent line load,

$$\overline{p}(x,t)\dot{w}(x,0,t) = 2R\int_0^{\pi} p(x,\theta,t)\dot{w}(x,\theta,t)d\theta; \tag{4.3}$$

an equivalent bending resistance,

$$\overline{q}(x,t)\dot{w}(x,0,t) = 2R\int_0^{\pi} |M_{pl}\dot{\kappa}_{\theta\theta}|d\theta; \tag{4.4}$$

an equivalent tensile force,

$$\bar{N}\dot{w}'(x,0,t)\dot{w}'(x,0,t) = 2RN_{pl}\int_0^{\pi} w'\dot{w}'(x,\theta,t)d\theta; \tag{4.5}$$

an equivalent mass per unit length,

$$\overline{m}\ddot{w}(x,0,t)\dot{w}(x,0,t) = 2Rm\int_0^{\pi} (\ddot{w}\dot{w} + \ddot{v}\dot{v})(x,\theta,t)d\theta. \tag{4.6}$$

Notice that all the deformation in the circumferential direction is lumped into the deflection at $\theta = 0$ so that from here on, w will be only a function of x,t. As hinted earlier, a bar is used to denote a quantity that has been integrated in the circumferential direction. Calculation of these equivalent functions requires some assumptions on the deformation shape of the rings. Several possible deformation profiles in the cross-section of cylinders are shown in Fig. 4-1. Cylinders and rings subjected to a uniform symmetric inward radial pressure deform as shown in Fig. 4-1a. The process known as dynamic pulse buckling involves circumferential bending

superposed on hoop compression [1]. The remaining three deformation modes are inextensible in the hoop direction. The kinematic model shown in Fig. 4-1b was developed by Wierzbicki and Suh [5] for static tube indentation under a "knife"-type punch. It consists of a flat top section and two circular arcs. This model was extended by Moussouros and Hoo Fatt [52] for impact or local pressure loading by replacing the flat top portion with a circular arc thereby creating a "dimple" model, Fig. 4-1c. The kinematics used to describe the deformation of the dimple model became very complicated because several independent variables were needed to describe its deformation. A good approximation to the more realistic dimple model is an unsymmetric stationary hinge model, 4-1d. The stationary hinge model consists of five stationary plastic hinges with rigidly rotating and translating ring segments. Notice that the kinematic model shown in Fig. 4-1d is easier to deal with because it is essentially one-degree-of-freedom models. This means that central deflection w_0 or $w(\theta = 0)$ uniquely determines the kinematics of the problem provided the position of outside hinges.

The derivation of the bending resistance $\bar{q}$ is treated as a separate problem by first examining the crushing force of a ring (per unit width).

4.2 Equivalent Bending Resistance

Experimental observations [47] show that the cross-sectional shape of the cylinder is a dimpled profile as shown in Fig. 4-1c. A separate analysis using the upper bound limit analysis technique to find the crushing force was done using this profile [52]. However, the dimple model, though realistic, required several independent variables to completely describe its deformation and thus led to a very complicated minimization procedure. Minimization had to be done numerically. Recently, it was found that a stationary hinge model, for which the location of hinges is defined by the angle α_o shown Fig. 4-1d, can be described by only one independent variable, the maximum or central ($\theta = 0$) displacement of the ring, and gives similar results to the dimple model. Because of this one-parameter representation of the crushing force and ring

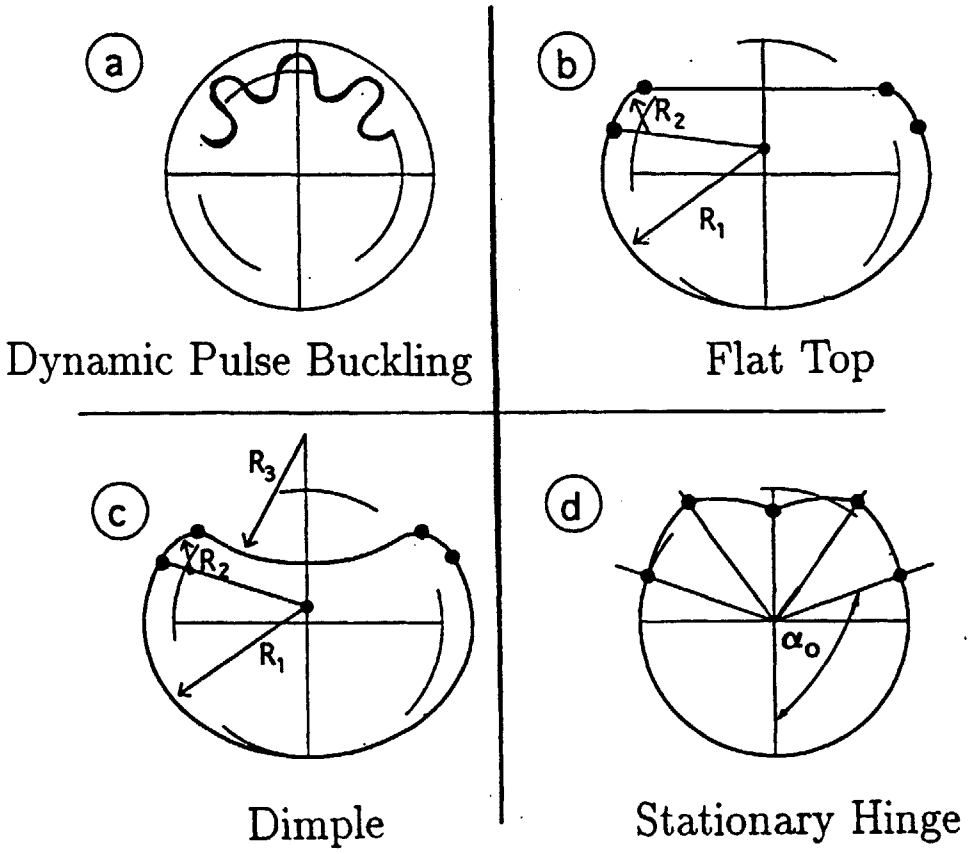

Figure 4-1: Possible cross-sectional shapes of the deformed shell.

kinematics, the stationary hinge model is favored and will be adopted in this analysis.

4.2.1 Non-axisymmetric stationary hinge model

The stationary hinge model described in Fig. 4-2 is non-symmetric and differs from the earlier one proposed by De Runtz and Hodge [53], which considers the symmetric crushing of tubes. The stationary hinge model is described by five hinges, A, B, C, D, and E, as shown in Fig. 4-2. The angle which describes the location of the fixed hinges, C and E, is given by α_o. The remaining hinges, A, B and D, are such that they bisect the upper portions of the ring. Therefore, $\overline{ED} = \overline{DA} = \overline{AB} = \overline{BC} = l_o$.

During deformation B and D rotate while A translates downward by a distance w_o, where $w_o = w(\theta = 0)$ is the central deflection of the isolated ring (see Fig. 4-2). Thus motion is simply described by the collapse of rigid bars $\overline{ED}, \overline{DA}, \overline{AB}$, and $\overline{BC}$. Notice that any point in the ring that lies within $\angle EOC$ does not deform.

The deformation $w(\theta)$ (see Fig. 4-4) can be described by a single time-like parameter w_o, given a fixed angle α_o. However, to simplify the derivation of the deflection profile around the ring, two intermediate angles will be defined in Fig. 4-2, ϕ and β. The initial values for these angles (corresponding to $w_o = 0$) are denoted ϕ_o and β_o (see Fig. 4-2).

Initially, $\angle AOB = \angle BOC = (\pi - \alpha_o)/2$ and both AOB and BOC form isosceles triangles such that $\angle OBA = \angle OCB = \pi/4 + \alpha_o/4$. The initial values of ϕ_o and β_o are therefore,

$$\phi_o = 3\alpha_o/4 - \pi/4 \qquad \text{and} \qquad \beta_o = \pi/4 - \alpha_o/4. \tag{4.7}$$

During deformation, w_o is related to ϕ and β. In the vertical direction,

$$w_o = AA' = AO - A'O. \tag{4.8}$$

Hence

$$w_o = R(cos\alpha_o + 1) - l_o(sin\beta + cos\phi), \tag{4.9}$$

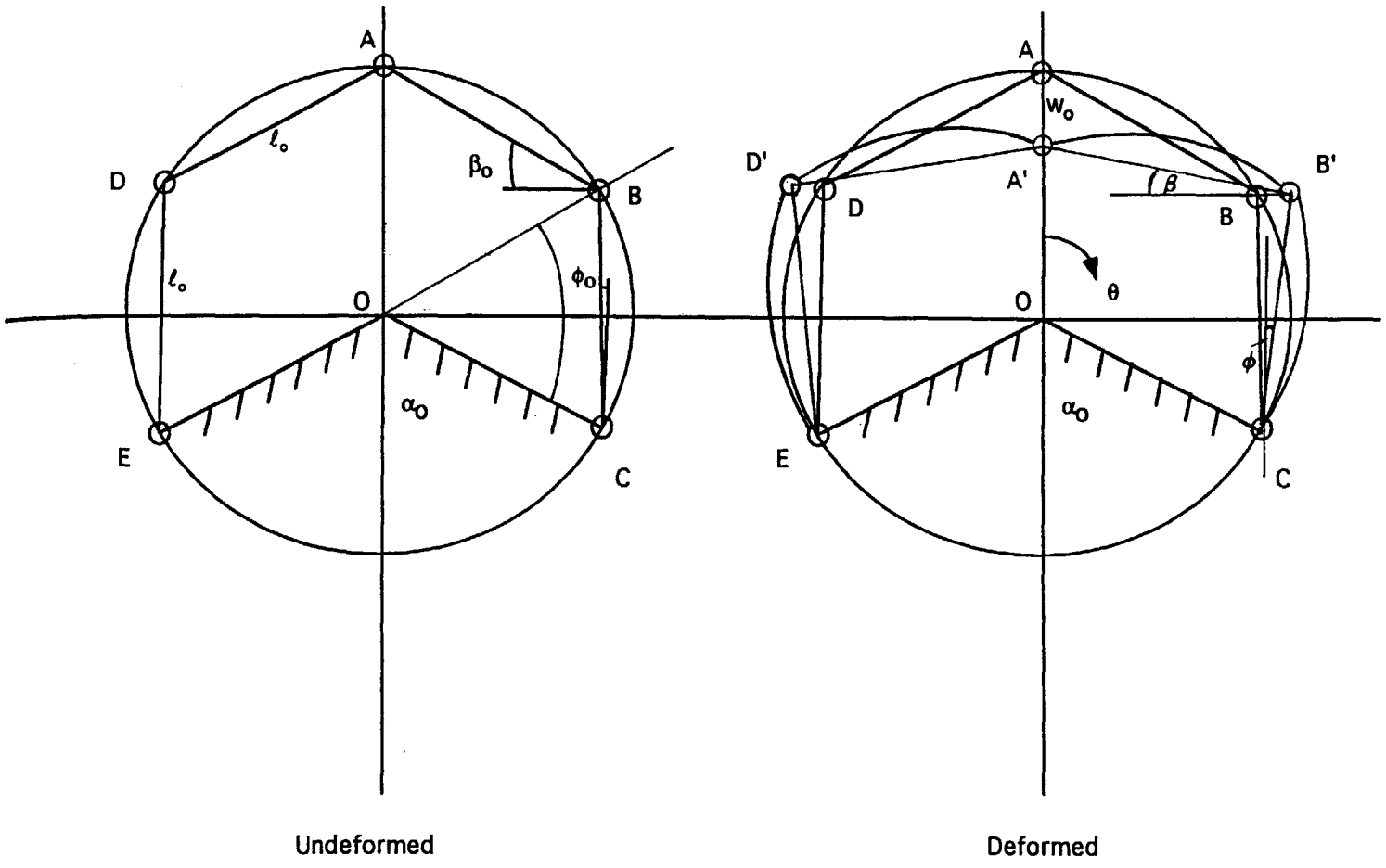

Figure 4-2: Non-axisymmetric stationary hinge model.

where $l_o = 2Rcos(\alpha_o + \phi_o)$.

Furthermore, taking components of $\overline{AB'}$ and $\overline{BC'}$ in the horizontal direction, β and ϕ are related to each other by

$$l_o cos\beta = l_o sin\phi + Rsin\alpha_o. \tag{4.10}$$

Note that again ϕ_o and β_o can be determined for a given α_o from Eqs. (4.9) and (4.10) by setting $w_o = 0$.

4.2.2 Ring resistance

The resistance due to bending of a force $\bar{q}$ is simply found by again using the principle of virtual work

$$\bar{q}.\dot{w}_o = 2[|2M_{pl}\dot{\phi}| + |2M_{pl}\dot{\beta}|]. \tag{4.11}$$

This equation can be further rewritten in terms of $\dot{\phi}$ by taking the time derivatives of Eqs. (4.9) and (4.10). From Eq. (4.10),

$$\dot{\beta} = -\frac{cos\phi}{sin\beta}\dot{\phi} \tag{4.12}$$

and also from Eq. (4.9),

$$\dot{w}_o = l_o \frac{cos(\phi - \beta)}{sin\beta}\dot{\phi}. \tag{4.13}$$

Substituting Eqs. (4.12) and (4.13) into Eq. (4.11) and canceling $\dot{\phi}$ on both sides of the equation, gives the normalized crushing force of the ring as

$$\frac{\bar{q}R}{M_{pl}} = \frac{2sin\beta[1 + |-\frac{cos\phi}{sin\beta}|]}{cos(\alpha_o + \phi_o)cos(\phi - \beta)}. \tag{4.14}$$

The absolute sign in Eq. (4.14) ensures that the rate of energy dissipation is always positive. For pressure loading, the value of α_o may be adjusted to match experimental profiles.

The normalized crushing force $\bar{q}R/M_{pl}$ for several values of α_o (solid line) is compared to that of the dimple model (dashed line) in Figure 4-3. Due to geometrical constraints, the stationary hinge model undergoes locking (no additional deflection can occur) for the smaller values of α_o (for instance, see $\alpha_o = 80^o$ and $\alpha_o = 85^o$). In fact, to achieve deflections of the order $w_o/R = 0.2$, α_o should be greater than $\pi/2$. In a more realistic ring deformation mechanism, the angle α_o should increase as the ring deforms. One may argue, however, that in such a case the ring model would no longer be a stationary one. For simplicity, α_o will be kept a constant value, $\alpha_o = \pi/2$. Incidently, $\alpha_o = \pi/2$ gives the lowest crushing force curve.

As in the dimple ring model, the bending resistance varies weakly with central deflection, and will be taken as a constant value given by

$$\bar{q} = \frac{8M_{pl}}{R}. \tag{4.15}$$

This crushing force is equal to the one used by Wierzbicki and Suh [5] in which a different non-symmetric ring model was used. The fact that these two forces are similar is an indication of the insensitivity to the assumed mode of deformation for non-symmetric ring models.

4.3 Calculation of Other Equivalent Parameters

In evaluating the other equivalent parameters, the deformation of each material point on the ring must be calculated. A Lagrangian description of the problem is used to describe deformation shown in Fig. 4-4. For a given deflection w_o, the deformation of each material point of the ring must be described in two regions $0 < \theta < (\pi - \alpha_o)/2$ and $(\pi - \alpha_o)/2 < \theta < \pi - \alpha_o$. In region $(\pi - \alpha_o)/2 < \theta < \pi - \alpha_o$, the entire arc BC undergoes rotation about hinge C. However, each material point on the arc BC rotates with a different radius of rotation depending on its location on arc BC. For instance, point P, located at $w = w(\theta_2)$, rotates with a radius $\overline{PC}$ to P'. A point in the region $0 < \theta < (\pi - \alpha_o)/2$ undergoes both rotation as well as translation about B'. A point Q, located at $w = w(\theta_1)$, undergoes translation and rotates about B'

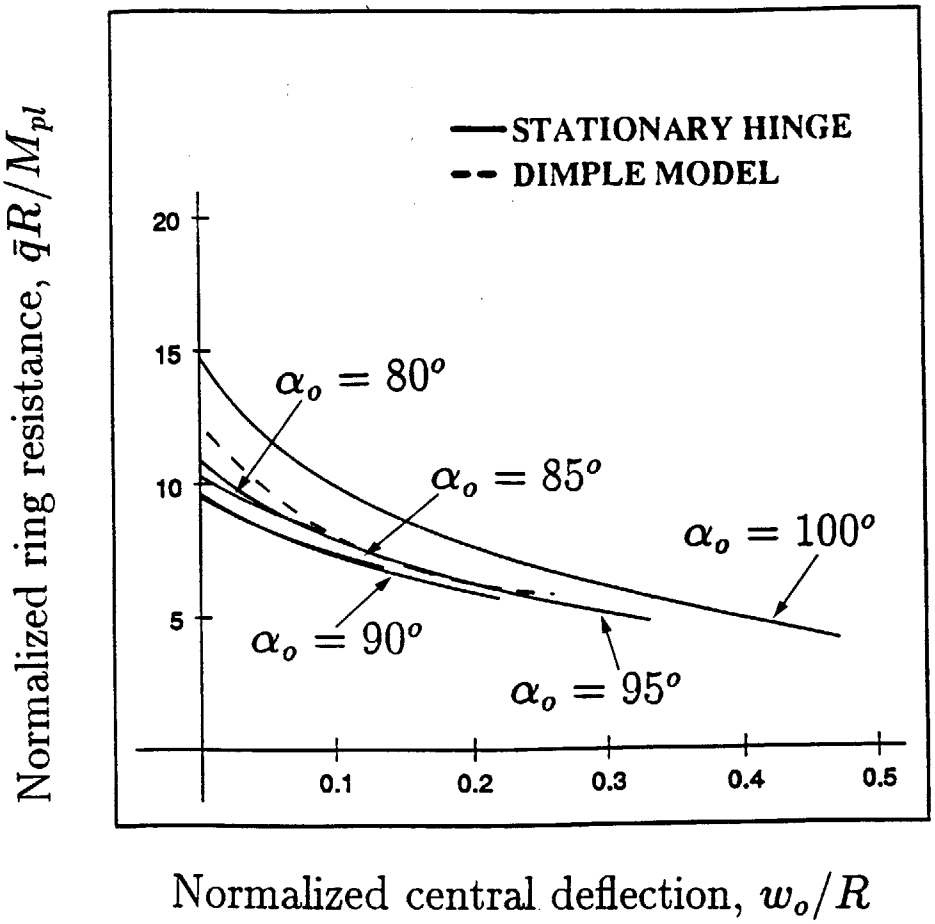

Figure 4-3: Ring resistance.

with radius $\overline{QB}$ to Q'. Formulas to describe $w(\theta)$ in the different regions are explicitly derived in Appendix A.

The other equivalent parameters, $\bar{p}$, $\bar{N}$, and $\bar{m}$, will be further defined in terms of new variables Θ_0, Θ_1, and Θ_2 which depend on the acceleration, velocity and displacement fields in the circumferential direction. The new quantities are defined as follows

$$\Theta_o = \int_0^\pi \frac{p}{p_o}\frac{\dot{w}}{\dot{w}_o}(\theta)d\theta, \tag{4.16}$$

$$\Theta_1 = \int_0^\pi \frac{w'\dot{w}'}{w_o\dot{w}_o}(\theta)d\theta, \tag{4.17}$$

$$\Theta_2 = \int_0^\pi \frac{\ddot{w}\dot{w}}{\ddot{w}_0\dot{w}_o}(\theta)d\theta. \tag{4.18}$$

The above parameters can be interpreted as integrated average values of the respective quantities with the associated velocity $\dot{w}_o$ as a weighting function. These parameters would depend on the central deflection w_o and therefore vary for each x-location.

Evaluation of the effective line pressure loading or Θ_0 requires a description of the distribution of dynamic pressure in the circumferential direction. This value differs for specific problems, but an example of how one would calculate Θ_0 for an assumed pressure distribution is given in Appendix B. However, the values of Θ_1 and Θ_2 only depend on the kinematics of the stationary hinge model. Using the expression for $(w/R)^2$ derived in Appendix A, the quantities $\dot{w}/\dot{w}_o(\theta)$, $w'\dot{w}'/(w_o\dot{w}_o)(\theta)$ and $\ddot{w}\dot{w}/(\ddot{w}_0\dot{w}_o)(\theta)$ are evaluated in Appendix B where the kinematics are more accurately expressed in vector components. These products obviously depend on the central deflection of the ring w_o. They are numerically intergated for each w_o (or x-location) and Fig. 4-5 shows how Θ_1 and Θ_2 vary with the central deflection of the ring w_o (or location x). Notice that there is very little dependence on w_o and for practical purposes both Θ_1 and Θ_2 can be taken as constant, both equal to 0.25.

Introducing Θ_0, Θ_1, and Θ_2, the equivalent parameters become

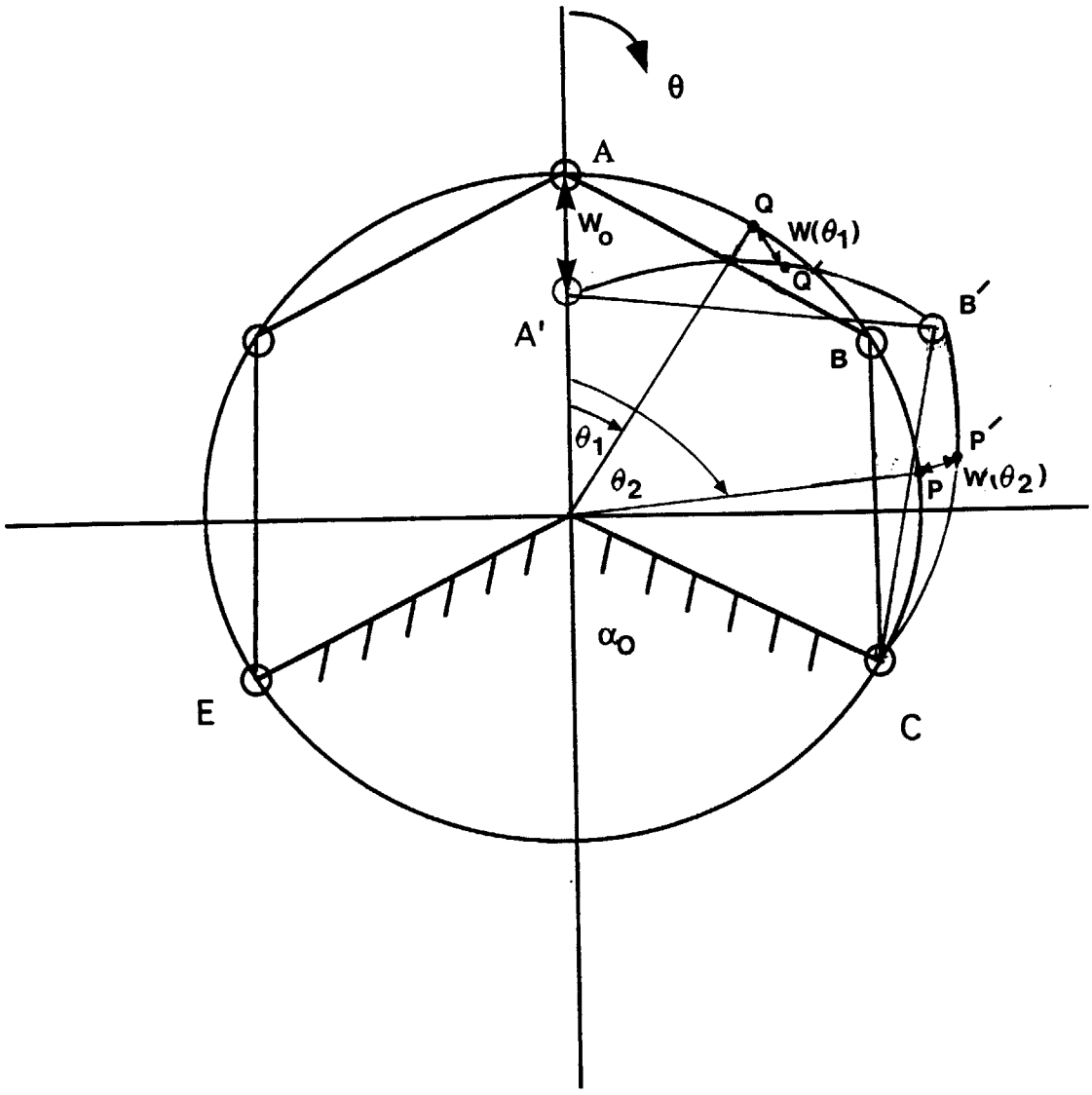

Figure 4-4: Kinematics of the deformed ring.

$$\bar{p} = 2Rp_o\Theta_o, \tag{4.19}$$

$$\bar{N} = 2RN_{pl}\Theta_1, \tag{4.20}$$

and

$$\bar{m} = 2Rm\Theta_2. \tag{4.21}$$

It should be pointed out again that the equivalent parameters $\bar{p}, \bar{q}, \bar{N}$ and $\bar{m}$ are not constant but depend on the central deflection w_0. However, in all cases their dependence on w_o is weak and in Table 4.1 average values of the respective quantities are given in the range of ring deflection $0 < w_0 < 0.4R$. The above intrinsic property of the ring model that renders the equivalent parameters approximately constant constitutes a corner stone of the string-on-foundation analogy. A more refined theory could be developed in which $\bar{p}, \bar{q}, \bar{N}$ and $\bar{m}$ will be known functions of an unknown deflection w_o. However, this will lead to a nonlinear partial differential equation and the mathematical simplicity of the present model would be lost.

4.4 The Wave Equation

Recall from Eq. 4.2 that

$$\bar{T}\dot{w}|_{ends} + 2\int_0^L \bar{p}\dot{w}dx = 2\int_0^\xi [\bar{q}\dot{w} + \bar{N}_{pl}w'\dot{w}' + \bar{m}\ddot{w}\dot{w}]dx. \tag{4.22}$$

Integrating Eq. (4.22) by parts

$$(\bar{T} - 2\bar{N}w')\dot{w}|_{ends} + 2\int_0^\xi (\bar{m}\ddot{w} - \bar{N}w'' + \bar{q} - \bar{p})\dot{w}dx = 0, \tag{4.23}$$

where $\bar{T}$ now represents an applied shear force at the end. From variational calculus, the system is reduced to the following partial differential equation:

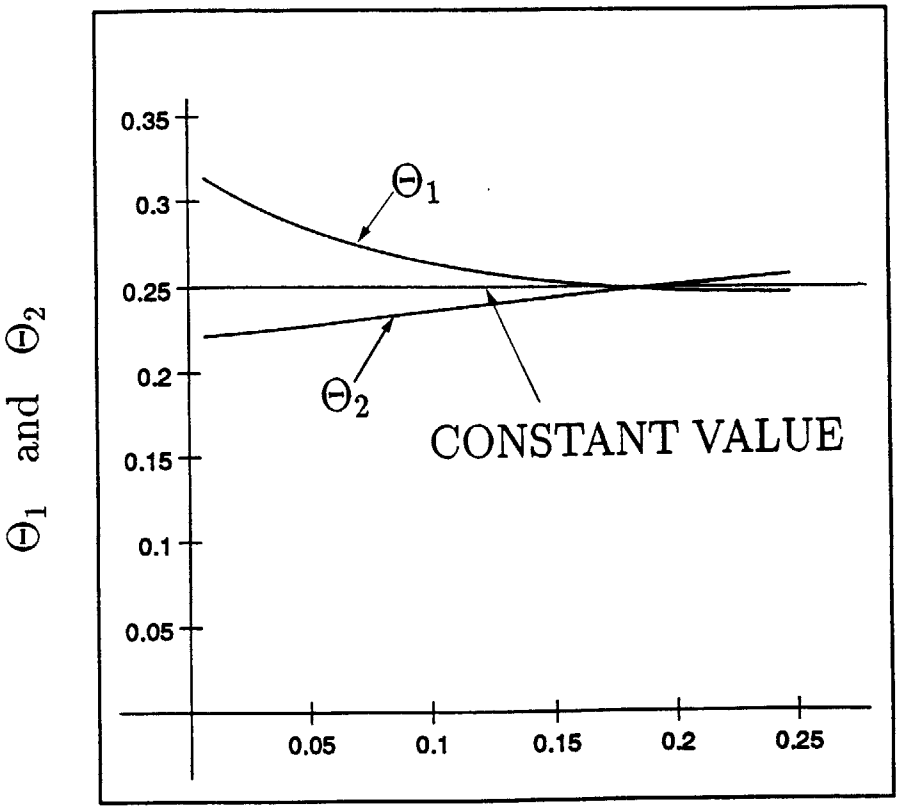

Figure 4-5: Variation of Θ_1 and Θ_2 with w_o/R.

Table 4.1: Equivalent parameters calculated for the stationary hinge model

$\bar{p}$	$\bar{q}$	$\bar{N}$	$\bar{m}$
$2Rp_0\Theta_0$	$8M_{pl}/R$	$0.5R\bar{N}_{pl}$	$0.5R\bar{m}$

$$\bar{m}\ddot{w} - (\bar{N}w')' + \bar{q} - \bar{p} = 0 \tag{4.24}$$

subject to the boundary conditions

$$w' = 0 \quad \text{at } x = 0 \tag{4.25}$$

and

$$2\bar{N}w' = T \quad \text{at } x = \xi. \tag{4.26}$$

Equation 4.24 is also subject to the initial conditions

$$w = 0 \quad \text{at } t = 0 \tag{4.27}$$

and

$$\dot{w} = 0 \quad \text{at } t = 0. \tag{4.28}$$

For impulsive or impact loading Eq. (4.28) would include the initial velocity. Equations (4.24) - (4.28) represent an initial-boundary value problem for an inhomogeneous wave equation with an inhomogeneous boundary condition at $x = \xi$. A similar problem that was formulated for a rigid-plastic cylinder undergoing projectile impact showed that the exact solution of the non-homogeneous wave equation [38] becomes complicated by certain non-linearities. These non-linearities are due mainly to the rigid plastic assumption of the material behavior. The complexity of this initial-boundary value problem also depends on the type of pressure loading.

The cylindrical shell under large plastic deformation can therefore be modeled

as a rigid-plastic string resting on a rigid-plastic foundation. If the deformations are small (less than shell thickness), bending effects must be included and the equation of motion to describe the shell deformation becomes very complex. Numerical schemes may be employed in finding solutions to such problems. The problem, however, becomes very simplified when the shell reaches its membrane state.

4.5 Dimensionless Parameters

To help perform parametric studies, a convenient set of dimensionless parameters will be defined. First, however, two groups of parameters can be distinguished in the transverse wave equation Eq. (4.24), the speed of the transverse wave c and a characteristic linear dimension x_0

$$c^2 = \frac{\bar{N}}{\bar{m}} = \frac{\sigma_0}{\rho}, \qquad x_0 = \frac{\bar{N}}{\bar{q}}. \tag{4.29}$$

It is convenient to non-dimensionalize some variables using the above characteristic parameters. A general characteristic length is denoted l_c. The characteristic length of the unstiffened shell under line load pressure is half of the extent of the load, $l_c = L$, while for the ring-stiffened shell it is half of the length of the bay, $l_c = l$. For projectile impact into an infinite cylinder, l_c is the ratio of the tensile to support strengths, x_o of Eq. (4.29).

A general characteristic mass M_c is defined such that for impact problems, M_c is the impacting mass M_o, and for impulsive loading of the stiffened shell, M_c is the lumped mass of the stiffener $\bar{M}$. A characteristic mass is not used in the problem of impulsive loading of the unstiffened shell.

Likewise, a general characteristic velocity V_c will be used such that for the impact problem $V_c = V_o$, and for the impulsive loading of the stiffened shell, $V_c = \bar{V}$.

The following dimensionless quantities are introduced:

$\tilde{x} = x/l_c$	axial coordinate
$\tilde{t} = tc/l_c$	time
$\nu = V_c/c$	velocity
$\tilde{w} = w\bar{N}/l_c^2\bar{q}$	transverse deflection
$\eta = M_c/\bar{m}l_c$	mass ratio
$\zeta = \bar{Q}/\bar{q}l_c$	stiffness ratio
$\tilde{f} = \bar{T}/\bar{q}l_c$	shear force
$\tilde{p} = \bar{p}/\bar{q}$	line load amplitude

In terms of these dimensionless quantities, the governing equations of the problem take the form

$$\tilde{w}_{\tilde{t}\tilde{t}} - \tilde{w}_{\tilde{x}\tilde{x}} - \tilde{p}(\tilde{x}, t) + 1 = 0 \tag{4.30}$$

and

$$\tilde{f} - \tilde{w}_{\tilde{x}} = 0 \qquad \text{at boundaries,} \tag{4.31}$$

subjected to the initial conditions,

$$\begin{aligned} \tilde{w}(\tilde{x}, 0) &= 0 \\ \tilde{w}_{\tilde{t}}(\tilde{x}, 0) &= \nu f(x). \end{aligned} \tag{4.32}$$

The subscripts denote differentiation with respect to the corresponding dimensionless variable and $f(x)$ is a function used to describe the shape of the initial velocity.

Chapter 5

Unloading Conditions

Plastically deforming bodies experience dissipative work. Therefore, final deformation is attained after unloading has begun. According to Eq. (3.11) the plastic deformation in the circumferential and axial directions has been decoupled. Therefore two separate unloading criteria must be imposed for the plastic flow in these two directions.

We define a uniaxial string or $\mathcal{U}$-unloading boundary by the condition of vanishing of axial strain rate

$$\dot{\epsilon}_{xx} = 0 \qquad \longrightarrow \qquad w'\dot{w}' = 0 \tag{5.1}$$

and a lateral support or $\mathcal{L}$-unloading boundary by requiring that the transverse velocity of the string becomes zero

$$\dot{w} = 0. \tag{5.2}$$

The $\mathcal{U}$-boundary is associated with the end of fully plastic tensile forces in the string, while the $\mathcal{L}$-boundary is related to the end of rigid plastic foundation deformation. Given a rigid-plastic material idealization, it is necessary that both $\dot{\epsilon}_{xx} > 0$ and $\dot{w} > 0$ for deformation to occur. From here on we will omit the subscript on the axial strain rate.

An unloading boundary is understood as a curve in the (x, t) plane for which either $\dot{\epsilon} = 0$ or $\dot{w} = 0$. In general $\mathcal{U}$- and $\mathcal{L}$-boundaries are different. At the $\mathcal{U}$ boundary

stretching of the string ceases because there can be no more plastic flow of the shell in the axial direction. A "frozen" section of the string can still undergo rigid body motion, $\dot{w} \neq 0$, so that the foundation can continue to be crushed. However, if the $\mathcal{L}$-boundary is met first, the motion of the string-on-foundation will stop.

Chapter 6

Projectile Impact into Cylinders

Consider an infinitely long cylinder being impacted by a mass M_o moving with velocity V_o. With the string-on-foundation model, the impacting mass and the cylinder are shown in Fig. 6-1.

The impacting mass strikes the cylinder at $x = 0$ and $t = 0$ and instantly generates two types of waves - longitudinal and transverse. The longitudinal wave for a rigid-perfectly plastic material travels at an infinite speed and pre-stresses the string to the yield value $\bar{N}$. This is followed by a transverse wave which propagates at finite speed $c = \sqrt{\sigma_o/\rho}$. It is the transverse wave that deflects the string and leaves a permanent local deflection in the shell.

The moving mass produces a shear force in the string which in turn decelerates the mass. Thus, considering half of the string, one gets

$$\bar{T} = -\frac{M_o}{2}\ddot{w}(0,t), \tag{6.1}$$

or in dimensionless form

$$\tilde{f} = -\frac{\eta}{2}\tilde{w}_{\tilde{t}\tilde{t}}(0,\tilde{t}). \tag{6.2}$$

The initial-boundary value problem is formulated by setting the pressure term $\tilde{p}$ in Eq. (4.30) equal to zero to give

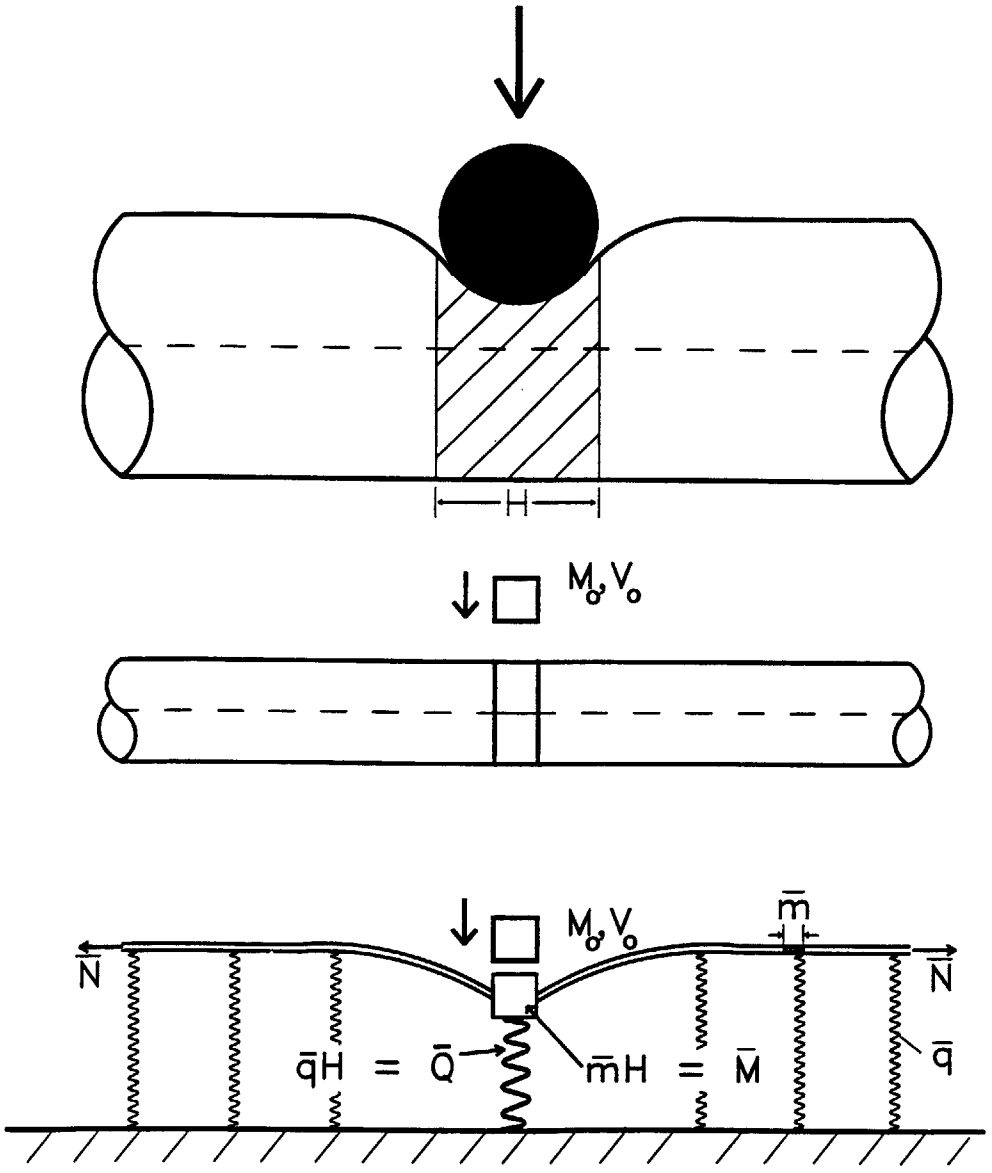

Figure 6-1: Impact of a spherical projectile on an infinite tube and a simple computational model.

$$\tilde{w}_{\tilde{t}\tilde{t}} - \tilde{w}_{\tilde{x}\tilde{x}} + 1 = 0 \qquad \tilde{x} < \tilde{t}, \tag{6.3}$$

It should be emphasized that under the rigid-plastic assumption, Eq. (6.3) is only valid for $\tilde{\epsilon}_{\tilde{t}} > 0$ and $\tilde{w}_{\tilde{t}} > 0$.

Substituting Eq.(6.2) into Eq. (4.31) also gives

$$\frac{\eta}{2}\tilde{w}_{\tilde{t}\tilde{t}} + \tilde{w}_{\tilde{x}} = 0 \qquad \text{at } \tilde{x} = 0. \tag{6.4}$$

The other boundary condition at the wave front is replaced by the conditions of kinematic and dynamic continuity, which together in the dimensionless form take the form of only one condition

$$[\tilde{w}_{\tilde{x}}] + [\tilde{w}_{\tilde{t}}] = 0 \qquad \text{at } \tilde{x} = \tilde{t}. \tag{6.5}$$

Additionally, homogeneous initial conditions must be satisfied

$$\tilde{w}(\tilde{x}, 0) = 0 \tag{6.6}$$

and

$$\tilde{w}_{\tilde{t}}(\tilde{x}, 0) = \begin{cases} \nu & \text{at } \tilde{x} = 0 \\ 0 & \text{for } |\tilde{x}| > 0 \end{cases} \tag{6.7}$$

Note that in the present problem the linear dimension l_c in the definitions of dimensionless quantities is set equal to the characteristic length $x_0 = \bar{N}/\bar{q}$.

6.1 Summary of the Exact Solution

Rosales et al [38] used the method of characteristics to derive an exact solution of the problem. Rather than rederive his solution here, some of his results are summarized and compared to an engineering approximation in the subsequent section.

Rosales' solution revealed an interesting dependence of the problem on a new pa-

rameter γ that is proportional to the ratio of normalized impacting mass to normalized velocity

$$\gamma = \frac{\eta}{4\nu} = \frac{c\bar{q}M_o}{4\bar{m}\bar{N}V_o}. \tag{6.8}$$

The solution to this problem becomes further complicated because of the nature of the $\mathcal{U}$- and $\mathcal{L}$- unloading boundaries. Recall that the $\mathcal{U}$-boundary marks the onset of $\dot{\epsilon} = 0$, while the $\mathcal{L}$-boundary corresponds to $\dot{w} = 0$. The solution is given for various ranges of γ as shown in the phase plane of Figure 6-2. The solid and the dashed lines represent the loading and unloading (both types) waves, respectively. To date, only a solution for which $1 < \gamma < 2$ exists in complete form. The expression for transverse deflections has a particularly simple form if γ is in the range $1 < \gamma < 2$,

$$\tilde{w}(\tilde{x},\tilde{t}) = \frac{1}{4}(\tilde{x}^2 - \tilde{t}^2) - \frac{\eta}{4}(\tilde{x} - \tilde{t}) + \frac{\eta\nu}{2}(\gamma - 1)[e^{\frac{2}{\eta}(\tilde{x}-\tilde{t})} - 1] \quad ,\tilde{x} < \tilde{t}. \tag{6.9}$$

Equation (6.9) can be differentiated to give the normalized velocity

$$\tilde{w}_{\tilde{t}} = \frac{-\tilde{t}}{2} + \frac{\eta}{4} - \nu(\gamma - 1)e^{\frac{2}{\eta}(\tilde{x}-\tilde{t})} \quad ,\tilde{x} < \tilde{t}, \tag{6.10}$$

and the normalized slopes

$$\tilde{w}_{\tilde{x}} = \frac{\tilde{x}}{2} - \frac{\eta}{4} + \nu(\gamma - 1)e^{\frac{2}{\eta}(\tilde{x}-\tilde{t})} \quad ,\tilde{x} < \tilde{t}. \tag{6.11}$$

Notice that unloading always starts at the point $\tilde{x} = \tilde{t} = 2\nu$ and that at this point, both $\tilde{w}_{\tilde{t}}$ and $\tilde{w}_{\tilde{x}}$ are identically equal to zero, independent of γ. Also notice that the slope given in Eq. (6.11) is always negative, independent of γ.

A quantity related to the strain rate ($\dot{\epsilon} = w'\dot{w}'$) is the rate of change in slope

$$\tilde{w}_{\tilde{x}\tilde{t}} = -\frac{2\nu}{\eta}(\gamma - 1)e^{\frac{2}{\eta}(\tilde{x}-\tilde{t})} \quad ,\tilde{x} < \tilde{t}. \tag{6.12}$$

Setting Eq. (6.10) equal to zero gives the $\mathcal{L}$-boundary. The $\mathcal{U}$-boundary ($\dot{\epsilon} = 0$) is found by setting Eq. (6.11) equal to zero because Eq. (6.12) is never zero.

The following arguments briefly summarize various ranges of the solution:

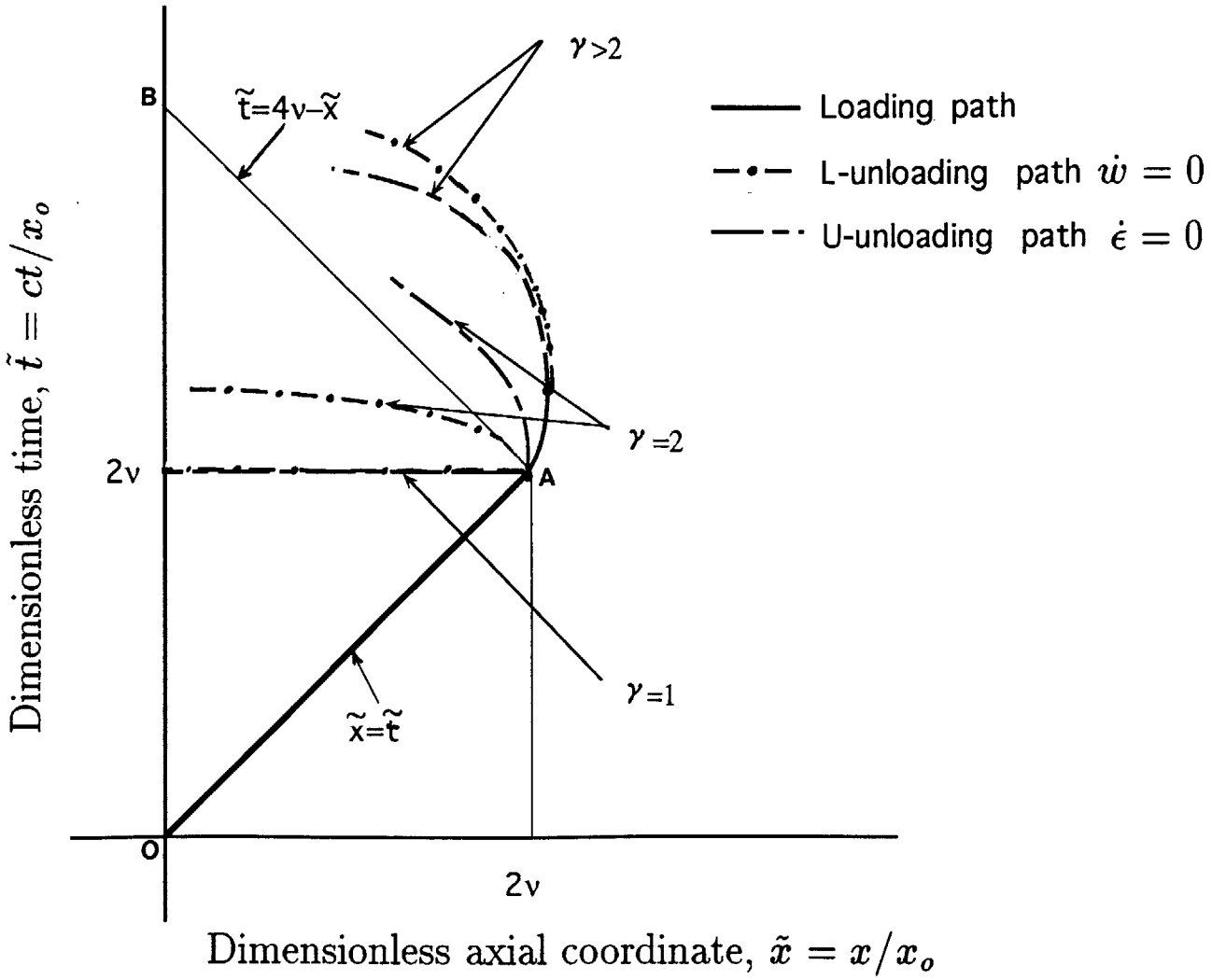

Figure 6-2: Phase plane analysis of impact into cylinder.

1. A solution of the problem does not exist for which $\gamma < 1$. At the point of impact,

$$\tilde{w}_{\tilde{x}\tilde{t}}(\tilde{x}=0) = \frac{-2\nu}{\eta}(\gamma-1)e^{-\frac{2}{\eta}\tilde{t}}. \tag{6.13}$$

   If $\gamma \leq 1$, then $\tilde{w}_{\tilde{x}\tilde{t}}(\tilde{x}=0) > 0$ and the strain rate at the point of impact is negative because $\tilde{w}_{\tilde{x}}(\tilde{x}=0) < 0$. The material cannot undergo plastic flow using our rigid-plastic material assumption. This means that the tensile forces in the string will never reach $\bar{N}$ and thus, transverse plastic waves cannot start to propagate.

2. When $1 < \gamma < 2$, the $\mathcal{L}$-boundary will always occur before the $\mathcal{U}$-boundary, as shown in Fig. 6-2.

3. When $\gamma = 2$ the $\mathcal{L}$-boundary is just tangent to the left- outgoing characteristic, and for $\gamma > 2$ the solution given by Eq. (6.9) results in an $\mathcal{L}$-boundary that lies out of the region OAB. From a set of plausible arguments, Rosales shows that the unloading wave is of the characteristic-type and must therefore travel with a speed less than or equal to the plastic wave speed c. It appears that the conditions $\dot{w} = 0$ and $\dot{\epsilon} = 0$ are governed by local events, not by unloading waves sweeping in from the boundary conditions, as is commonly the case in mechanics. If they were "true" unloading waves, they would travel with an elastic wave of infinite speed. Perhaps the $\mathcal{L}$ and $\mathcal{U}$-unloading waves should be defined here as unloading events to distinguish them from the elastic unloading waves.

   It was proposed to extend the loading path out of the region OAB (ie. into the region $\tilde{x} > 2\nu$ and $\tilde{t} > 4\nu - \tilde{x}$) . A consequence of this extension, however, is a complex interaction between the $\mathcal{U}$- and $\mathcal{L}$-unloading boundaries which is still currently being resolved.

The $\mathcal{L}$-unloading boundary for which $1 < \gamma < 2$ is explicitly

$$\tilde{x} = \tilde{t} + \frac{\eta}{2} \ln[\frac{\eta/4 - \tilde{t}/2}{\nu(\gamma - 1)}]. \tag{6.14}$$

The permanent displacement of the string is obtained by eliminating time between Eqs. (6.9) and (6.14). Normalized permanent deflections of the string for three different values of the parameter γ are shown in Fig. 6-3 (solid lines). The time growth of a central deflection $\tilde{\delta} = \tilde{w}(\tilde{x} = 0, t)$ for the same values of the parameter γ is shown in Fig. 6-4 (solid line).

6.2 An Approximate Solution

A good approximation to this problem can be achieved by assuming all plastic deformation is concentrated at the plastic wave front and that the deformed region, $x \leq \xi$, undergoes rigid body motion. This assumption was proved to be a limiting case ($\gamma = 1$) of the more exact solution [38]. In this case, the velocity and acceleration of the deformed region, $\dot{w}$ and $\ddot{w}$, are independent of x and are functions of time only. A typical description of the velocity field as it propagates in time is shown in Fig. 6-5.

In the interest of allowing the reader more physical insight into the problem, variables will be non-dimensionalized only after derivation. Setting $p = 0$ for impact loading and integrating Eq. (4.24) with respect to x from $x = 0$ to $x = \xi$, one can satisfy equilibrium globally

$$\bar{N}w'|_0^{\xi} - \bar{m}\ddot{w}\xi - \bar{q}\xi = 0 \tag{6.15}$$

Introducing the boundary condition at $x = 0$ into Eq. (6.15) gives

$$2\bar{N}w'|_{x=\xi} - M_o\ddot{w} - 2\bar{m}\ddot{w}\xi - 2\bar{q}\xi = 0. \tag{6.16}$$

This equation can be conveniently written as

$$2c\bar{m}\dot{w} + [M_o + 2\bar{m}\xi]\ddot{w} = -2\xi\bar{q}, \tag{6.17}$$

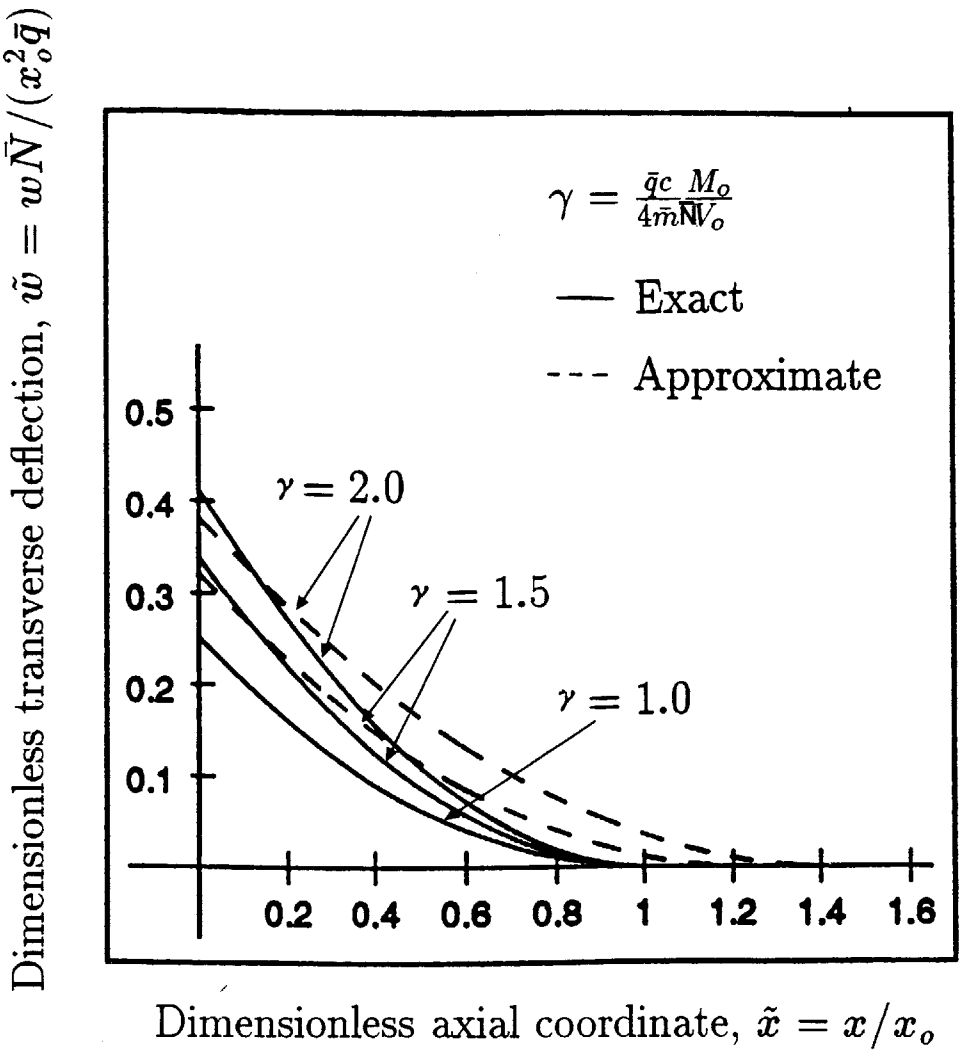

Figure 6-3: Permanent longitudinal deflection profiles of a cylinder for various values of the mass ratio parameter.

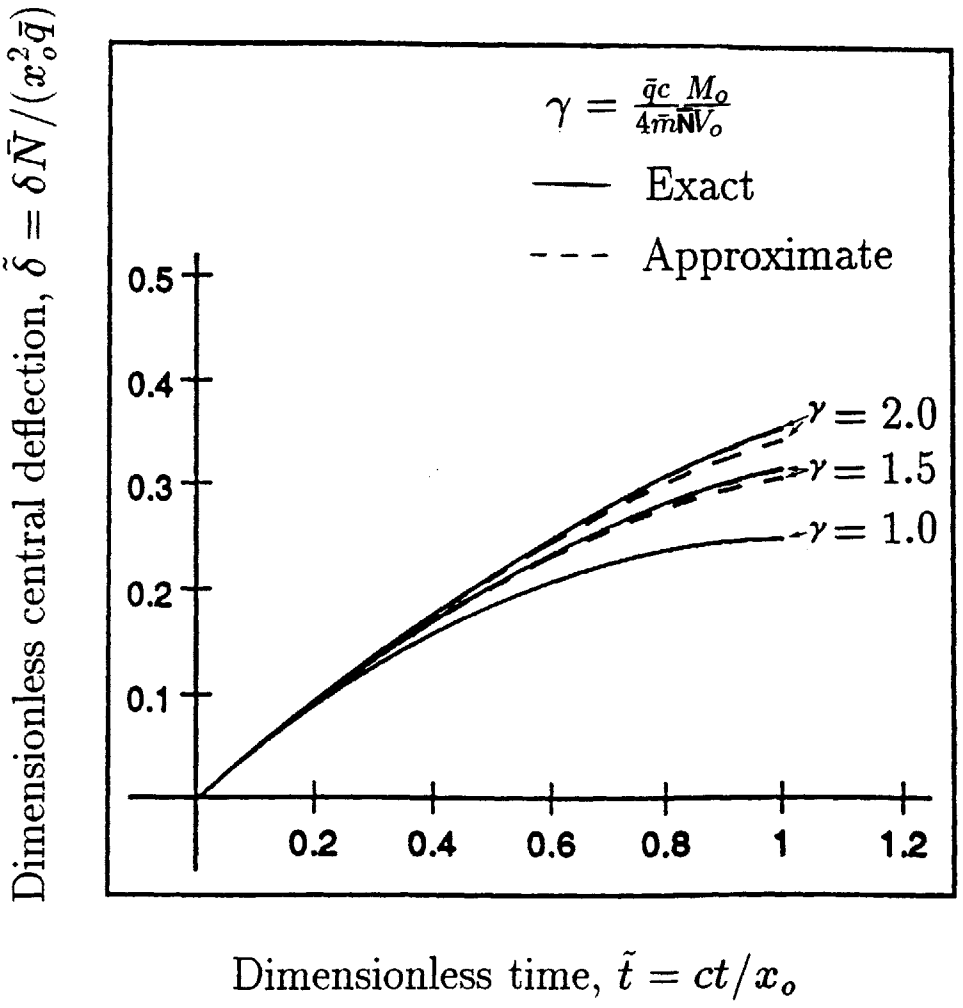

Figure 6-4: Growth of the dimensionless shell deflection with time at the point of impact.

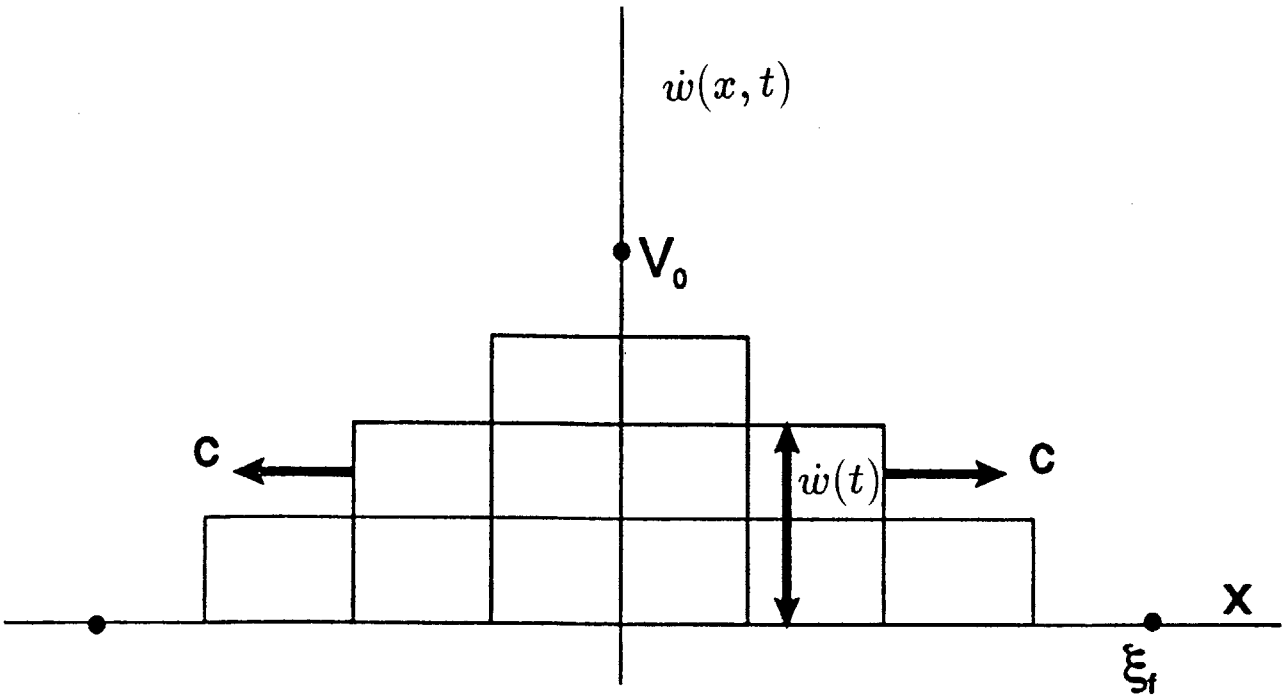

Figure 6-5: Instantaneous velocity profiles of the shell.

where the first term in this equation has been transformed using the condition of dynamic continuity

$$[\bar{N}w_x] + \dot{\xi}[\bar{m}w_t] = 0 \qquad \text{at} \quad x = t. \tag{6.18}$$

Equation (6.17) furnishes a linear, first order ordinary differential equation for $\dot{w}$ and can be re-arranged in standard form

$$\ddot{w} + \frac{2\bar{m}c}{M_o + 2\bar{m}ct}\dot{w} = -\frac{2ct\bar{q}}{M_o + 2\bar{m}ct}, \tag{6.19}$$

subject to the initial condition

$$\dot{w}(0) = V_o. \tag{6.20}$$

It should be mentioned that this formulation satisfies the condition of kinematic and dynamic continuity as well as global equilibrium, expressed via the principle of conservation of linear momentum in the plastically deforming region.

6.2.1 Solutions for velocity and displacement profiles

The solution of the initial value problem, defined by Eqs. (6.19) and (6.20) is

$$\dot{w}(t) = \frac{M_o V_o/(2\bar{m}c) - \bar{q}t^2/(2\bar{m})}{M_o/(2\bar{m}c) + t}. \tag{6.21}$$

The velocity diminishes to zero at

$$t_f = \sqrt{\frac{V_o M_o}{\bar{q}c}}, \tag{6.22}$$

where t_f is the response time of the shell. The transverse displacements can be obtained by integrating the velocity of each deforming point on the cylinder axis with respect to time

$$w(x,t) = \int_{t_1=x/c}^{t} v(t)dt. \tag{6.23}$$

Here a point on the shell located at a distance x from the impact site acquires a displacement after the wavefront arrives at that location at time $t_1 = x/c$.

For $t > t_f$, the string remains rigid and motionless. Because the plastic wave propagates at constant speed c, the maximum extent of the deformation is simply

$$\xi_f = ct_f. \tag{6.24}$$

Introducing η and ν to relate the impacting mass to the shell, one can express Eq. (6.21) in dimensionless from

$$\tilde{w}_{\tilde{t}}(t) = \frac{(\nu - \rho/4)}{(1 + \rho/2\tilde{t})} - \frac{\tilde{t}}{2} + \frac{\rho}{4}. \tag{6.25}$$

From Eq. (6.23), the transverse displacement in normalized coordinates is

$$\tilde{w}(\tilde{x}, \tilde{t}) = \frac{1}{4}(\tilde{x}^2 - \tilde{t}^2) - \frac{\eta}{4}(\tilde{x} - \tilde{t}) + \frac{\eta\nu}{2}(\gamma - 1)\ln[\frac{1 + 2\tilde{x}/\eta}{1 + 2\tilde{t}/\eta}]. \tag{6.26}$$

Note that for $\gamma = 1$ the last term in Eqs. (6.9) and (6.26) vanishes and the approximate solution coincides with the exact solution.

The normalized central displacement $\tilde{\delta}$ is obtained from Eq. (6.26) by setting $\tilde{x} = 0$

$$\tilde{\delta} = \tilde{w}(0) = -\frac{1}{4}\tilde{t}^2 + \frac{\eta}{4}\tilde{t} + \frac{\eta\nu}{2}(\gamma - 1)\ln[1 + 2\tilde{x}/\eta] \tag{6.27}$$

A comparison between the exact and approximate solutions for the central deflection as it grows with time is shown in Fig. 6-4. The solutions coincide for $\gamma = 1$. For other values than $\gamma = 1$ the difference between the approximate central deflection (dotted line in Fig. 6-4) and exact central deflection is small.

Unloading in the approximate solution (the $\mathcal{L}$-boundary) occurs for the entire string at the same time $\tilde{t}_f$

$$\tilde{t} = \tilde{t}_f = \sqrt{\eta\nu}. \tag{6.28}$$

Equation (6.28) is substituted into Eq. (6.26), and a closed-form solution is obtained for the permanent deflection profile $w(x, t_f) = w_f(x)$

$$\tilde{w}_f = \frac{1}{4}\tilde{x}^2 - \frac{\nu\eta}{4} - \frac{\eta}{4}(\tilde{x} - \sqrt{\eta\nu}) + \frac{\eta\nu}{2}(\gamma - 1)\ln[\frac{1 + 2\tilde{x}/\eta}{1 + 2\tilde{t}/\eta}]. \tag{6.29}$$

These are also compared to the exact solution in Fig. 6-3 (dashed line). Notice that the deflections are more localized in the exact solution.

It should be mentioned that the use of momentum conservation with the assumed

velocity profile for the critical case of $\gamma = 1$ (constant in space, variable in time) has also been used and found to be quite accurate in perforation analysis of a circular membrane [39]. Unlike the cylindrical shell, the circular membrane has a homogeneous wave equation because there is no foundation force $\bar{q}$ to represent the ring resistance.

6.2.2 Ballistic limits

It is interesting to note that the maximum slope at the impacted end, calculated from Eq. (6.26) is independent of the mass parameter and is a function of the velocity parameter only

$$w'|_{x=0} = \tilde{w}_{\tilde{x}} = \nu = V_o/c. \tag{6.30}$$

Perforation of the shell can either occur in a shear or tensile mode, Jones [54]. Shear plugging starts when the contact shear force between the impacting mass and the string, $2r_r N_{pl} w'$, is equal to the plastic through-thickness shear resistance $\pi r_p h \sigma_o/\sqrt{3}$ on, say, half of the circumference of the projectile with the radius r_p

$$2r_p N_{pl} w' = \frac{\sigma_o}{\sqrt{3}} h \pi r_p. \tag{6.31}$$

Combining Eqs. (6.30) and (6.31), one may obtain a simple estimate for the onset of the perforation process

$$V^*_{shear} = \frac{\pi}{2\sqrt{3}} \sqrt{\frac{\sigma_o}{\rho}}. \tag{6.32}$$

Note that at the point of fracture the flow stress σ_0 is understood as the tensile strength of the material.

Tensile failure of the shell under the projectile occurs when the maximum axial strain is equal to the critical strain to necking, $\epsilon_{max} = \epsilon_c$. Thus, using the definition of finite axial strain, Eq. (6.30), and a strain concentration factor around the projectile of $\pi^2/4$ gives

$$V^*_{tension} = \frac{\pi}{2}\sqrt{2\epsilon_c}\sqrt{\frac{\sigma_o}{\rho}}. \tag{6.33}$$

Predictions from both criteria are identical if $\epsilon_c = 0.16$. For smaller critical rupture strain tensile necking occurs first, while, for higher values, shear plugging may be dominant. The above equations represent a lower bound on the ballistic limit. An upper bound can be obtained using the methodology developed by Wierzbicki and Hoo Fatt [7] for circular membranes.

Stronge [23] performed a series of projectile impact tests on metal tubes and measured permanent deflection profiles for a range of impact velocities up to the ballistic limit and beyond. The material properties for two different thicknesses of steel plates and experimental ballistic limits are gathered in Table 6.1. Predictions from the formulas given by Eqs. (6.32) and (6.33) are shown in the last two columns. Upper bound calculations could be performed to close the gap between the theory and experiment using the methodology developed by Wierzbicki and Hoo Fatt [7].

6.2.3 Extension of the model

Stronge [23] measured also permanent displacement of the shell under the projectile. Initial attempts to correlate experiments with the theoretical solution (Eq. (6.9) or (6.26)) failed because of exceedingly large error. However, it soon becomes clear that the present model requires important modification to described with some realism high velocity missile impact on cylinders. According to Fig. 6-3 dynamic deflection profiles are much more localized than static ones. The extent of plastic deformation in the axial direction on either side of the symmetry axis is only three to four times greater than the projectile diameter itself. In the existing formulation the resistance of the shell to the process of dynamic denting is derived only from a portion of the shell outside the circumferential strip of width H under the projectile (see Fig. 6-1). Because of a double curvature dimple present in this strip, its crushing resistance may constitute a substantial portion of the resistance of the entire tube. This important effect can be incorporated into the theory by considering impact on an infinite cylinder

Table 6.1: Comparison between the experimental and theoretical ballistic limit in the tests reported by Stronge.

h (mm)	ρ (g/cm^3)	σ_y (N/mm^2)	σ_o	ϵ_c	$\bar{V}^*_{exp}$ (m/sec)	$\bar{V}^*_{shear}$	$\bar{V}^*_{tension}$
1.76	7.8	149	254	0.28	190	162	215
3.2	7.8	191	281	0.28	230	171	223

reinforced by a relatively stiffer ring with a prescribed crushing resistance $\bar{Q}$ and mass $\bar{M}$, Fig. 6-1.

$$\begin{aligned} \bar{Q} &= H\bar{q} \\ \bar{M} &= H\bar{m} \end{aligned} \tag{6.34}$$

Such a modified solution can be derived using the momentum conservation approach but the problem will not be pursued here any further.

6.2.4 Damage of cylinders due to dropped objects

This type of impact is of relatively frequent occurrence in offshore construction, drilling and production activities. Most of the accidents are associated with crane lifting operation although collisions of tubular members with ships also fall in this category. According to Moan [55], the frequency of falling pipes is of the order of 1-5 cases per year per platform during regular drilling operations. One most dangerous object for impact is a drill-collar, a part of the drilling string. A typical drill collar has a mass of approximately 3200 Kg, length 10 m and inner and outer diameters of 76 mm and 241 mm, respectively. Such massive structures may behave as almost rigid bodies under impact conditions and may cause substantial local damage and penetration of the impacted structure.

Because of relatively low impact velocities, a simplified analysis based on a quasi-static indentation solution can be used. Such an analysis was recently presented by Hoo Fatt and Wierzbicki [51], and will be briefly reviewed here.

The relationship between the force and central deflection δ of a rigid punch in-

denting a cylinder is

$$P = 2\sqrt{2\bar{q}\bar{N}\delta} \tag{6.35}$$

This relationship can be obtained by solving Eq. (4.24) and (4.26) with inertia forces set equal to zero, $p(x,t) = 0$ and $\bar{T} = -P$. A good estimate for the maximum central deflection of the impacted shell can be obtained by equating the kinetic energy of the impacting drill-collar to the plastic work of the resisting transverse force $P(\delta)$

$$\frac{1}{2}M_o V_o^2 = \int_0^{\delta_f} P(\delta)d\delta. \tag{6.36}$$

Performing the integration and using Eq. (6.35) the following simple expression is obtained

$$\frac{\delta_f}{h} = 0.47(M_o/(\rho h^3))^{\frac{2}{3}}(V_o/c)^{\frac{4}{3}}. \tag{6.37}$$

The above approach seems reasonable because for low velocity impact, there is time for the plastic deformation to spread farther than in high velocity impact. As a result, the relative contribution of the "ring" just below the impacting mass should be small compared to the resistance of the entire shell.

As an illustrative example, calculations where run for a brace tubular element characterized by the geometry and material given in Table 6.2. The results of calculations are presented in Fig. 6-6, showing the depth of the dent caused by the impacting drill-collar versus the drop height. When the drill-collar drops from a height of 30 m, it produces a dent of 0.376 m, roughly half of the radius of the brace. Such an extreme damage is devastating to the affected structure and the brace will have to be replaced.

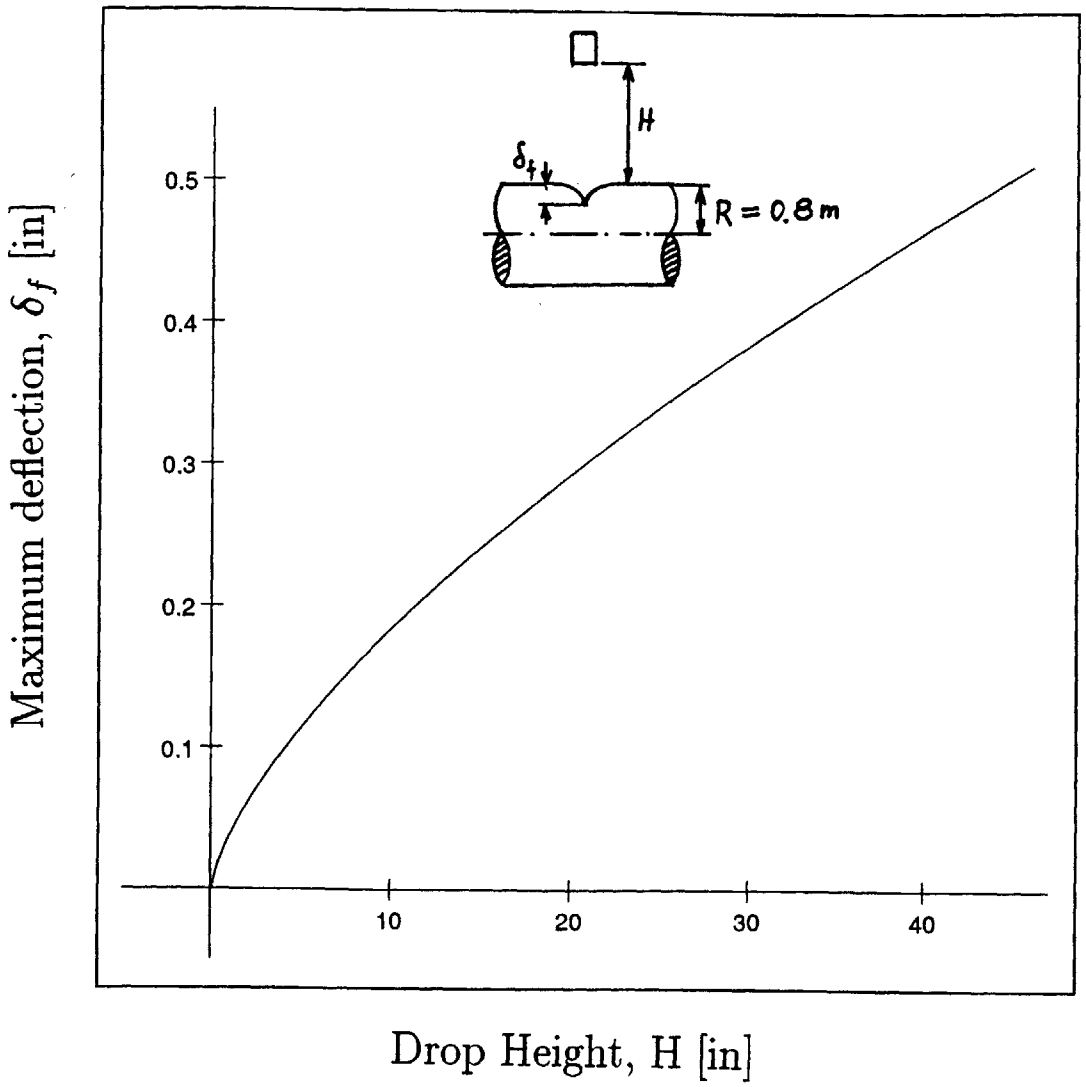

Figure 6-6: Damage of a tubular member caused by a dropped drill-collar as a function of the drop height.

Table 6.2: Geometrical and mechanical parameters of a typical offshore tubular member hit by a drill-collar.

$R\ (m)$	$h\ (mm)$	$\sigma_0\ (MPa)$	$\rho\ (Kg/cm^3)$
0.8	20	360	7.8

The present analysis addresses local deformation only. Global bending deformation occur for slender tubes and some impact energy will be absorbed in this mode. Amongst others, interaction of local and global deformation in tubes was studied by de Oliveira et al [56] and more recently by Paik [57].

Chapter 7

Explosive Loading on Unstiffened Shell

Consider an infinite cylinder subjected to a dynamic pressure pulse with spatial and temporal variation, Fig. 7-1. An approximate equation for the pressure shock and decay [58] which results from an explosion is

$$p(x,\theta,t) = p_o e^{-\frac{t}{\tau}} cos^2(\frac{\pi x}{2L}) g(\theta), \tag{7.1}$$

where p_o is the peak pressure, τ is the decay constant, and L is the extent of pressure load and the characteristic length in normalized parameters.

From the concept of a string-on-foundation, the equation of motion is given by Eqs. (4.30)-(4.32), where ν is calculated as a dimensionless impulse in the following section.

7.1 Impulsive Loading

The total area under the $p-t$ curve is defined as the applied impulse per unit length $\bar{I}$,

$$\bar{I} = \int_0^\infty \bar{p} e^{-\frac{t}{\tau}} dt = \bar{p}\tau. \tag{7.2}$$

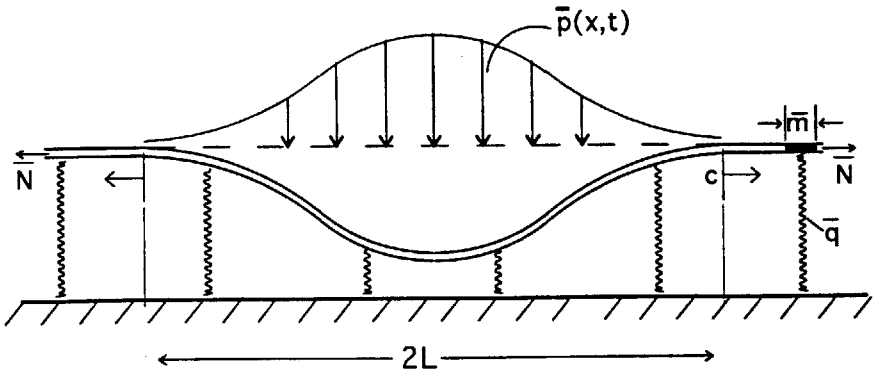

Figure 7-1: Unstiffened shell modeled as a rigid-plastic string on a rigid-plastic foundation.

An ideal impulsive loading is obtained by keeping $\bar{I}$ constant and setting $\tau \to 0$. The peak pressure then tends to infinity. In the case of impulsive loading, the equation of motion, Eq. (4.24), can be directly integrated in time by noting that for short times the string tension and the support forces can be neglected compared to an infinitely large pressure amplitude and acceleration. The result is

$$\bar{m}\dot{w}(x,0) = \bar{I}\cos^2(\frac{\pi x}{2L}). \tag{7.3}$$

Thus, the application of the ideal impulse is equivalent to prescribing an initial lateral string velocity with the amplitude $\bar{I}/\bar{m}$ and specified spatial variation to the string.

The dimensionless initial velocity is

$$\tilde{w}_{\tilde{t}}(\tilde{x},0) = \tilde{I}\cos^2(\frac{\pi}{2}\tilde{x}), \tag{7.4}$$

where $\tilde{I}$ is a dimensionless impulse defined by

$$\tilde{I} = \frac{\bar{I}c}{\bar{q}L} = \frac{\bar{p}}{\bar{q}}\frac{\tau c}{L}. \tag{7.5}$$

The dimensionless impulse $\tilde{I}$ replaces ν in the general form of the initial velocity condition, Eq. (4.32). The string is initially undisturbed so that the first initial condition is given as before by Eq. (4.32).

At the center of the string the shear force vanishes, $\bar{T} = \tilde{f} = 0$ so that the boundary condition (4.31) becomes

$$\tilde{w}_{\tilde{x}}(0,t) = 0. \tag{7.6}$$

The conditions of kinematic and dynamic continuity for w are automatically satisfied at the moving wave front $\tilde{x} = \tilde{t}$.

7.2 Summary of the Exact Solution

A full solution of the initial-boundary value problem was solved by Suliciu et al [42] for the general case of pressure pulse loading as well as the ideal impulse loading. Again only the salient discoveries will be described here. In the impulse case, the expression for the transient deflection is derived again using the method of characteristics

$$\tilde{w}(\tilde{x},\tilde{t}) = \frac{1}{2}[\tilde{t}^2 - \tilde{t}\tilde{I} - \frac{\tilde{I}}{\pi}\sin(\pi\tilde{t})\cos(\pi\tilde{x})] \qquad \text{for} \quad \tilde{t} \leq 1 - \tilde{x}. \tag{7.7}$$

As in Rosales' solution, this solution is only valid within a certain region [42]. One finds from using Eq. (7.7) that the $\mathcal{L}$-boundary always occurs before the $\mathcal{U}$-boundary if $\tilde{I} < 1$. The equation derived from the condition $\dot{w} = 0$ ($\mathcal{L}$-unloading boundary) is

$$2\tilde{t} - \tilde{I} - \tilde{I}\cos(\pi\tilde{t})\cos(\pi\tilde{x}) = 0. \tag{7.8}$$

Furthermore, it turns out that in a phase plane analysis, unloading starts immediately from the point $x = L$ (or $\tilde{x} = 1$) and moves towards the center. Positions of the unloading boundaries ($\mathcal{L}$-boundary) for several values of the dimensionless impulse $\tilde{I}$ are shown in Fig. 7-2. Notice that the solution for the $\mathcal{L}$-unloading boundary is only valid for impulses smaller than $\tilde{I}_{cr} = 0.89$.

By eliminating time between Eqs. (7.7) and (7.8), one can find a solution for permanent deflected shape of the string. The normalized deflected shapes for two values of the dimensionless impulse, $\tilde{I} = 0.1$ and $\tilde{I} = 0.89$, are shown in Fig. 7-3 (dotted lines). For small values of the dimensionless impulse ($\tilde{I} \to 0$), the solution of Eqs. (7.7) and (7.8) can be expanded to give the following simple expression for the permanent deflection

$$\tilde{w}_f(\tilde{x}) = \frac{\tilde{I}^2}{2}\cos^4(\frac{\pi\tilde{x}}{2}). \tag{7.9}$$

This solution is also plotted in Fig. 7-3. Notice that the solution for $\tilde{I} = 0.1$ is almost indistinguishable from the exact solution for $\tilde{I} \to 0$.

Figure 7-3 suggests that for impulses larger than the critical impulse, the string

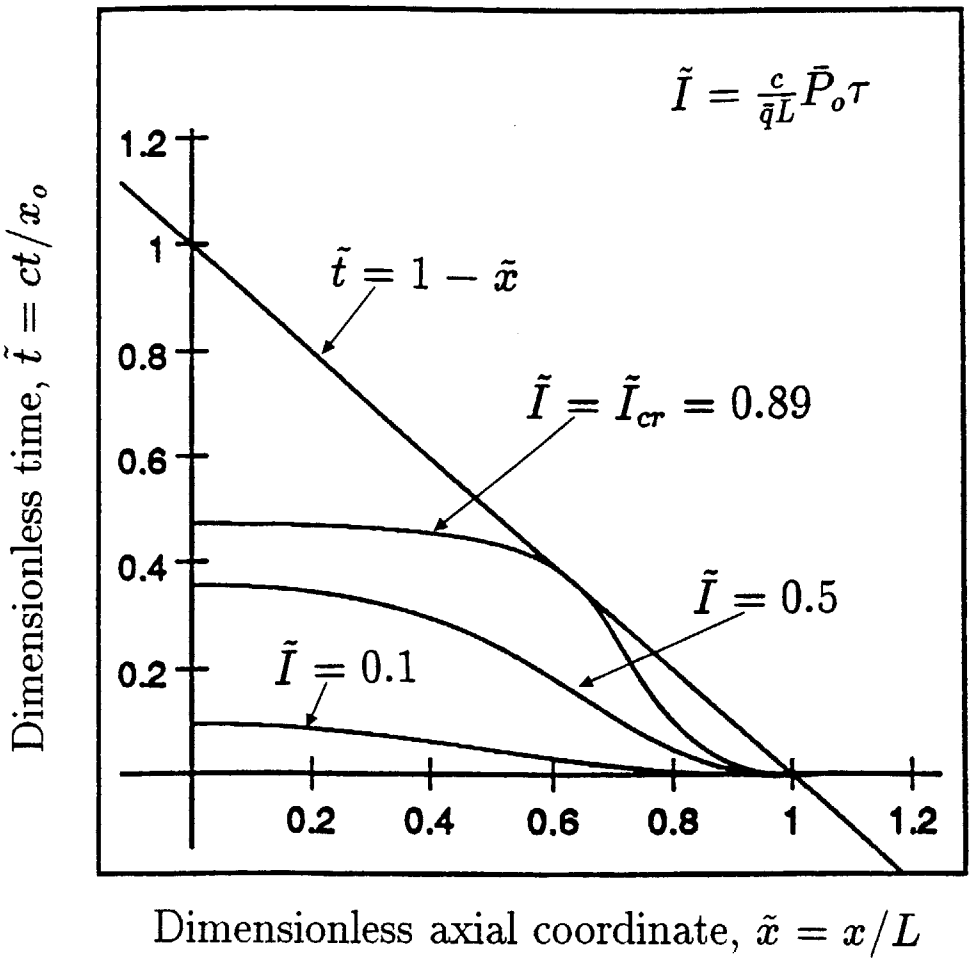

Figure 7-2: Propagation of unloading waves ($\mathcal{L}$-boundaries) in a pressure loaded shell for various values of the dimensionless impulse.

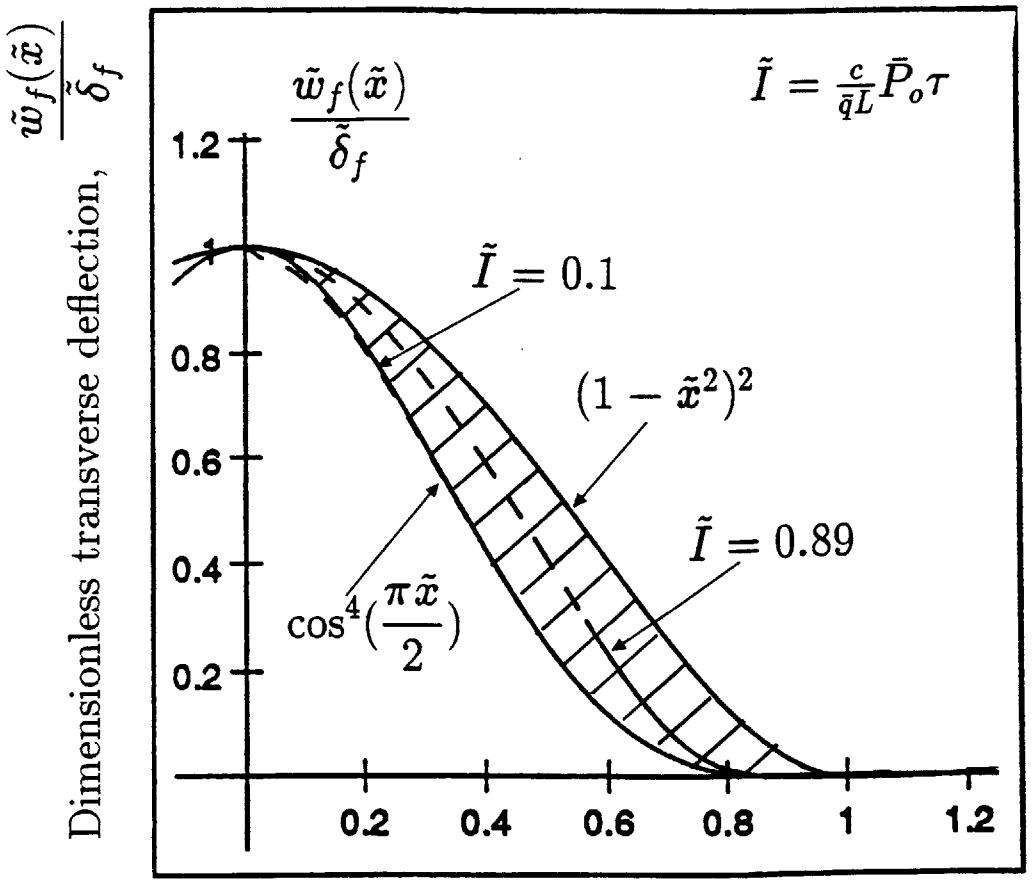

Figure 7-3: Normalized permanent deflection profiles of an unstiffened shell for small ($\tilde{I} = 0.1$) and large ($\tilde{I} = 0.89$) dimensionless impulse.

will tend to the shape of the applied impulse, the function $\cos^2 \frac{\pi}{2}\tilde{x} \approx (1-\tilde{x}^2)^2$. It can thus be concluded that under any circumstances, the deflected shapes will fall within the shaded area bounded by the shape $\cos^4 \frac{\pi}{2}\tilde{x}$, corresponding to small impulses, and the shape $\cos^2 \frac{\pi}{2}\tilde{x} \approx (1-\tilde{x}^2)^2$, corresponding to large impulses. This observation serves as a basis for developing an approximate, engineering solution to the problem.

7.3 An Approximate Solution

Modal solutions (solutions with fixed shapes but variable amplitudes) have been extensively used in the literature, Martin and Symonds [59] and Jones [60]. Typically, a shape function is chosen to fit the experimentally measured permanent deflections of the given structure. Then using this shape function, the partial differential equation is integrated over the characteristic length L thereby reducing it to an ordinary differential equation. The approach presented here is different because the shape function is selected on the basis of a thorough analysis of the exact solution of the problem. The modal method is illustrated by solving the problem for relatively large values of the impulse for which the following approximation of the final deflection profile is within 15 percent

$$w(x,t) = \delta(t)[1-(\frac{x}{L})^2]^2. \tag{7.10}$$

7.3.1 Modal analysis

Because the local equilibrium, expressed by Eq. (4.24) with $\bar{p} = 0$, is in general violated by the separable displacement field, the determination of an unknown, time variable amplitude will be based on the weaker, global equilibrium statement, Eq. (4.23), with $\xi = L$. Note that the solution given by Eq. (7.10) automatically satisfies the boundary conditions at $x = 0$, and with $\bar{T} = 0$, the boundary condition at $x = L$.

Substituting Eq. (7.10) into Eq. (4.24) and integrating with respect to x, one obtains the following second order linear ordinary differential equation

$$a_3\ddot{\delta} + a_2\delta + a_1 = 0, \tag{7.11}$$

where the coefficients a_1, a_2, and a_3 are defined as

$$a_1 = \int_0^L \bar{q}(1-(x/L)^2)^2 dx = \frac{8L\bar{q}}{15}, \tag{7.12}$$

$$a_2 = \int_0^L \bar{N}(-4x(1-(x/L)^2)/L^2)^2 dx = \frac{128\bar{N}}{105L}, \tag{7.13}$$

and

$$a_3 = \int_0^L \bar{m}(1-(x/L)^2)^4 dx = \frac{128L\bar{m}}{315}. \tag{7.14}$$

Equation (7.11) satisfies zero initial condition for displacement, $\delta(t=0)=0$. The initial velocity is calculated from Eq. (C.3) (see Appendix C) and is found as $\dot{\delta}(t=0) = 15\bar{p}/(16\bar{m})$, taking $f(x) = (1-(x/L)^2)^2$.

In the dimensionless coordinates $\tilde{w}(0,\tilde{t}) = \tilde{\delta}(\tilde{t})$ so that

$$\tilde{\delta}_{\tilde{t}\tilde{t}} + c_1\tilde{\delta} + c_2 = 0, \tag{7.15}$$

where the coefficients c_1 and c_2 are defined as

$$c_1 = \frac{a_2L^2}{a_3c^2} = 3 \tag{7.16}$$

$$c_2 = \frac{a_1\bar{N}}{a_3\bar{q}c^2} = \frac{21}{16}. \tag{7.17}$$

The solution in normalized coordinates is

$$\tilde{\delta}(\tilde{t}) = \frac{7}{16}(\cos\sqrt{3}\tilde{t} - 1) + \frac{15}{16\sqrt{3}}\tilde{I}\sin\sqrt{3}\tilde{t}. \tag{7.18}$$

The permanent deflection amplitude is defined by $\tilde{\delta}_f = \tilde{\delta}(\tilde{t} = \tilde{t}_f)$ where $\tilde{t}_f$ is the time at which the central velocity vanishes $\tilde{\delta}_{\tilde{t}}(\tilde{t} = \tilde{t}_f) = 0$. The final deflection shape

is thus

$$\tilde{w}_f = \tilde{\delta}_f[1 - \tilde{x}^2]^2. \tag{7.19}$$

One can differentiate Eq. (7.18) and set $\tilde{\delta}_{\tilde{t}} = 0$, to find the following relationship for $\tilde{t}_f$ and $\tilde{I}$

$$tan\sqrt{3}\tilde{t}_f = \frac{15\tilde{I}}{7\sqrt{3}} \tag{7.20}$$

A simple relationship between $\tilde{\delta}_f$ and the dimensionless impulse $\tilde{I}$ is found by using trigonometric identities and Eqs. (7.20) and (7.18)

$$\tilde{\delta}_f = \frac{7}{16}(\sqrt{[1 + \frac{1}{3}(\frac{15\tilde{I}}{7})^2]} - 1). \tag{7.21}$$

Comparisons between the exact and approximate solution are presented in Figs. 7-4 and 7-5. Figure 7-4 shows the time variation of central deflection amplitude, $\tilde{\delta}$ versus $\tilde{t}$. The approximate solution for the central deflection is at most 10 percent below the exact solution. The permanent central deflection is plotted versus the applied impulse in Fig. 7-5, $\tilde{\delta}_f$ versus $\tilde{I}$. Again the approximate modal solution is found to be within 10 percent of the exact solution. The agreement of exact and modal solutions is remarkable.

The main conclusion drawn from the above analysis is that a suitably chosen modal form solution could be used in transient problems with propagating loading and unloading waves. Furthermore, in the case of impulsive loading, varying according to $(1-(x/L)^2)^2 \approx \cos^2 \frac{\pi}{2}\tilde{x}$, the resulting permanent deflection profile has a shape similar to that of the applied load. This observation has been used to find approximate modal solutions for the deflection profile of the ring-stiffened shell for which equilibrium is considered within a single bay or between two ring stiffeners [46].

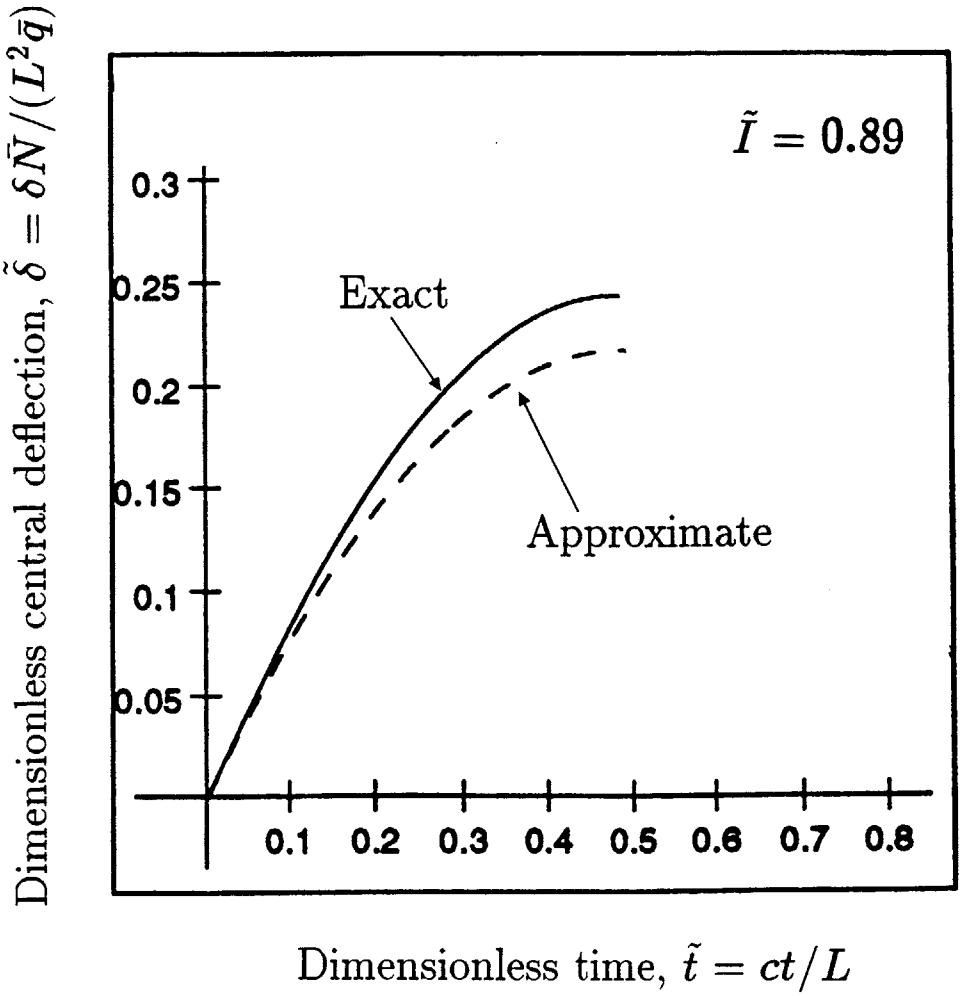

Figure 7-4: Dimensionless central deflection versus time (comparison of the exact and approximate solution).

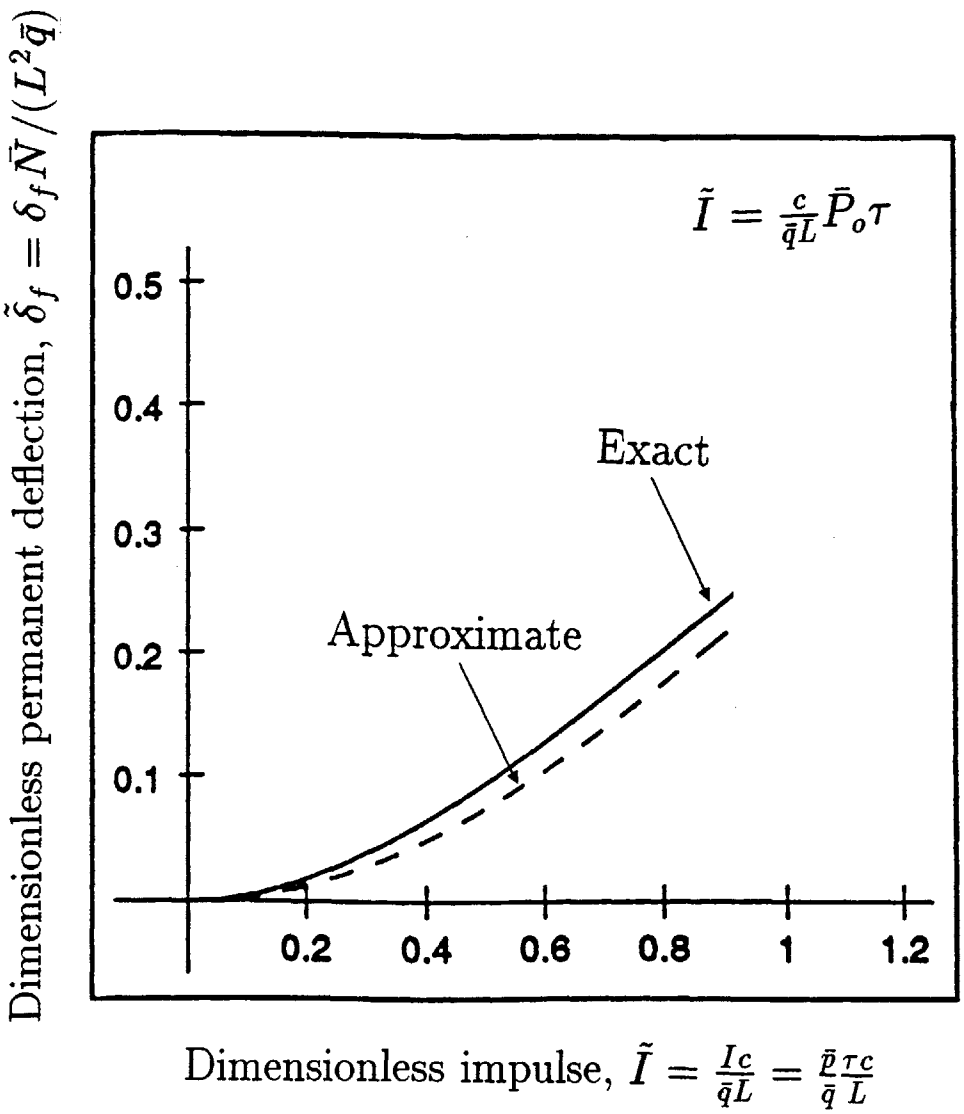

Figure 7-5: Dependence of dimensionless permanent central deflection on the magnitude of impulse.

7.4 Generalization for Different Pressure Distribution

The solution presented so far may also be extended to the impulsive loading of clamped shells of various lengths subjected to the general type of impulsive loading

$$\tilde{w}_{\tilde{t}}(\tilde{x},0) = \tilde{I} f(x), \tag{7.22}$$

where $f(\tilde{x})$ is a spatial distribution of impulse, for example a uniform impulse. The exact solution of the inhomogeneous wave equation, Eq. (4.30) with $\bar{p} = 0$, in the fixed domain $0 < \tilde{x} < 1$ and subjected to homogeneous boundary conditions $\tilde{w}_{\tilde{x}}(0,\tilde{t}) = \tilde{w}(1,\tilde{t}) = 0$ can be obtained using the eigenvalue expansion technique

$$\tilde{w}(\tilde{x},t) = \tilde{I} \sum_{n=1}^{\infty} \bar{H}_n \sin(\frac{\pi n}{2}\tilde{t}) \cos(\frac{\pi n}{2}\tilde{x}) - \frac{\tilde{t}^2}{2}, \tag{7.23}$$

where the $\tilde{t}^2$ term takes care of the inhomogeneity of the governing equation and the initial velocity expansion coefficients are given by

$$\bar{H}_n = \frac{4}{n\pi} \int_0^1 f(\tilde{x}) \cos(\frac{\pi n}{2}\tilde{x}) d\tilde{x}, \qquad n = 1, 2, ... \tag{7.24}$$

The above solution can be used to generate the so called iso-damage curves, determined experimentally by Greenspon et al [17].

Chapter 8

Explosive Loading on Ring-stiffened Shell

Consider again an infinite cylindrical shell, but as shown in Figure 8-1, with ring stiffeners equally spaced apart by a distance $2l$. The bays are numbered with an index i such that $i = 0$ corresponds to the central bay. The deformation of the shell is shown to consist of two components, a local deflection w_l and a global deflection w_g. As before, the extent of the applied load is $2L$. It is convenient to classify shells into three categories:

$l \ll L$ Very densely spaced rings. A smearing technique can be used in which stiffened shell is replaced by a uniform shell with an increased, equivalent thicknesses h_b and h_i when evaluating the bending energy and inertia terms, respectively. These equivalent thicknesses give rise to an elevated bending moment per unit length, $M_{pl} = \sigma_o h_b^2/4$, and a mass per unit area, $m = \rho h_i$. Formulas for h_b and h_i for a T-stiffener are derived in Appendix G.

$l < L$ Moderately densely spaced rings. Such shells are considered to be optimum with respect to strength and stiffness and therefore are most often encountered in industrial application. The present paper is concerned with this type of shells.

$l \approx L$ Sparsely spaced rings. This case is out of the scope of this thesis.

The stiffened shell undergoes several forms of damage depending on the load intensity. Such damage includes large plastic deformations with material or structural failure. This chapter focuses on that mode of failure for which there is incipient fracture at the base plate at the stiffener. In particular, the magnitude of the transient and final deflections of the deformed shell and the crack initiation of the shell are predicted.

Rather than start with the wave equation as in the previous chapters, the statement of global equilibrium will be rederived to show how ring-stiffeners might be incorporated into the problem formulation. As in Chapter 4, assume that at the ends of the loaded region there are rigid motions $\dot{w}$ in the integrated shear force $\bar{T}$. Extend Eq. (4.1) for half of the shell so that M_{pl} and m now vary in the axial direction x to account for ring stiffeners

$$\bar{T}\dot{w}|_{end} + \int_0^L 2R \int_0^\pi p(x,\theta,t)\dot{w}(x,\theta,t)d\theta dx = \int_0^L 2R \int_0^\pi |M_{pl}(x)\dot{\kappa}_{\theta\theta}|d\theta dx$$
$$\int_0^L 2R \int_0^\pi |N_{pl}w'\dot{w}'(x,\theta,t)|d\theta dx + \int_0^L 2R \int_0^\pi m(x)(\ddot{w}\dot{w} + \ddot{v}\dot{v})(x,\theta,t)d\theta dx. \quad (8.1)$$

Ring stiffeners provide localized resistance to circumferential bending and therefore cause less transverse deformation to occur at their locations. If the ring-stiffeners are viewed as point discontinuities as in References [6, 46], then Eq. (8.1) may be conveniently written in terms of the stiffeners parameters $\bar{M}$ and $\bar{Q}$

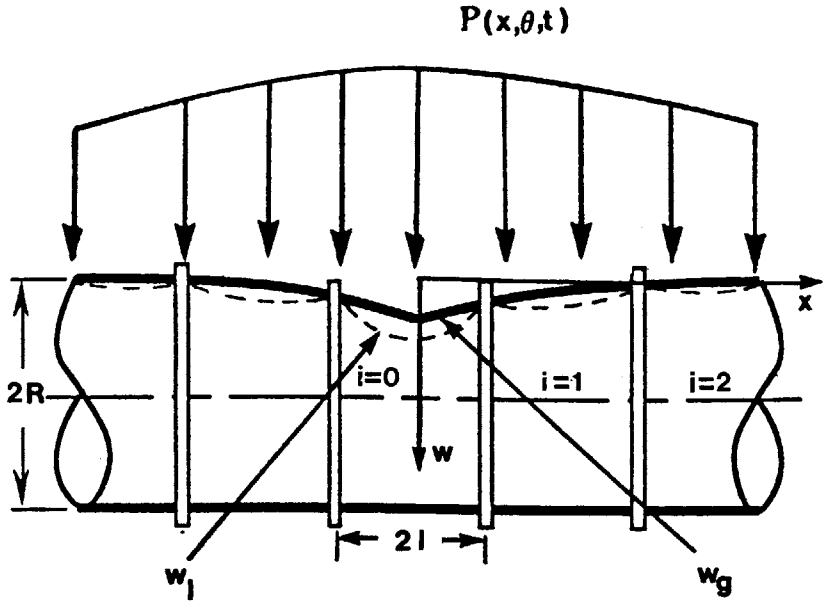

Figure 8-1: Ring-stiffened shell subjected pressure loading.

$$\bar{T}\dot{w}|_{end} + \sum_{i=0}^{N}\{\int_{\Lambda}^{(2i+1)l} 2R\int_0^{\pi} p(x,\theta,t)\dot{w}(x,\theta,t)d\theta dx\} =$$
$$\sum_{i=0}^{N}\{\int_{\Lambda}^{(2i+1)l}[2R\int_0^{\pi}|M_{pl}\dot{\kappa}_{\theta\theta}|d\theta + 2R\int_0^{\pi}|N_{pl}w'\dot{w}'(x,\theta,t)|d\theta +$$
$$2R\int_0^{\pi} m(\ddot{w}\dot{w}+\ddot{v}\dot{v})(x,\theta,t)d\theta]dx + (\bar{Q}+\bar{M}\ddot{w})\dot{w}|_{x=(2i+1)L}\}, \tag{8.2}$$

where,

$$\Lambda = \begin{cases} 0 & \text{for } i = 0 \\ (2i-1)l & \text{for } i = 1,2,3,... \end{cases} \tag{8.3}$$

As shown in Fig. 8-1, i denotes the bay number so that total number of stiffeners is $2N-1$. The lumped mass of the stiffener $\bar{M}$ is defined in terms of the local shell coordinates so that $dA = dxdz$

$$\dot{w}\ddot{w}\bar{M} = \int_A \rho dA[2R\int_0^\pi (\dot{w}\ddot{w} + \dot{v}\ddot{v})d\theta]. \tag{8.4}$$

The integral for the ring resistance $\bar{Q}$ involves a distance z from the neutral axis

$$\dot{w}\bar{Q} = \int_A \sigma_o z dA[2R\int_0^\pi \dot{\kappa}_{\theta\theta} d\theta]. \tag{8.5}$$

With these definitions, $\bar{M}$ and $\bar{Q}$ are calculated in Appendix F for the special case of a T-stiffened shell under explosive loading. Because the bending resistance and mass per unit length, M_{pl} and m, are written only for bays in Eq. (8.2), they no longer vary in x but are constants.

Equilibrium may now be imposed on a more local sense by writing the principle of virtual work between stiffeners or for each separate bay. The pressure distribution within each bay may be considered approximately constant (see Fig. 8-2). Furthermore, a solution will only be found for the central bay for cases in which several adjacent bays are subject to nearly the same pressure and undergo nearly the same deflection. This amounts to modeling the central bay as one in an infinitely long series of bays and stiffeners under uniform pressure loading. The validity of this approximation depends on the axial curvature from bay to bay and should be considered later. Thus, for the central bay,

$$\bar{T}\dot{w}|_{end} + \int_0^l 2R\int_0^\pi p(x,\theta,t)\dot{w}(x,\theta,t)d\theta dx = \int_0^l 2R\int_0^\pi |M_{pl}\dot{\kappa}_{\theta\theta}|d\theta dx + \int_0^l 2R\int_0^\pi |N_{pl}w'\dot{w}'(x,\theta,t)|d\theta dx + \int_0^l 2R\int_0^\pi m(\ddot{w}\dot{w} + \ddot{v}\dot{v})(x,\theta,t)d\theta dx, \tag{8.6}$$

where $\bar{T} = -(\bar{Q} + \bar{M}\ddot{w})/2$ is the shear force on the half bay and half of the stiffener. The solution for the deformation within the central bay is coupled with that for the stiffener via the boundary conditions.

Again using the concept of equivalent parameters, Eq. (8.6) can be reduced to

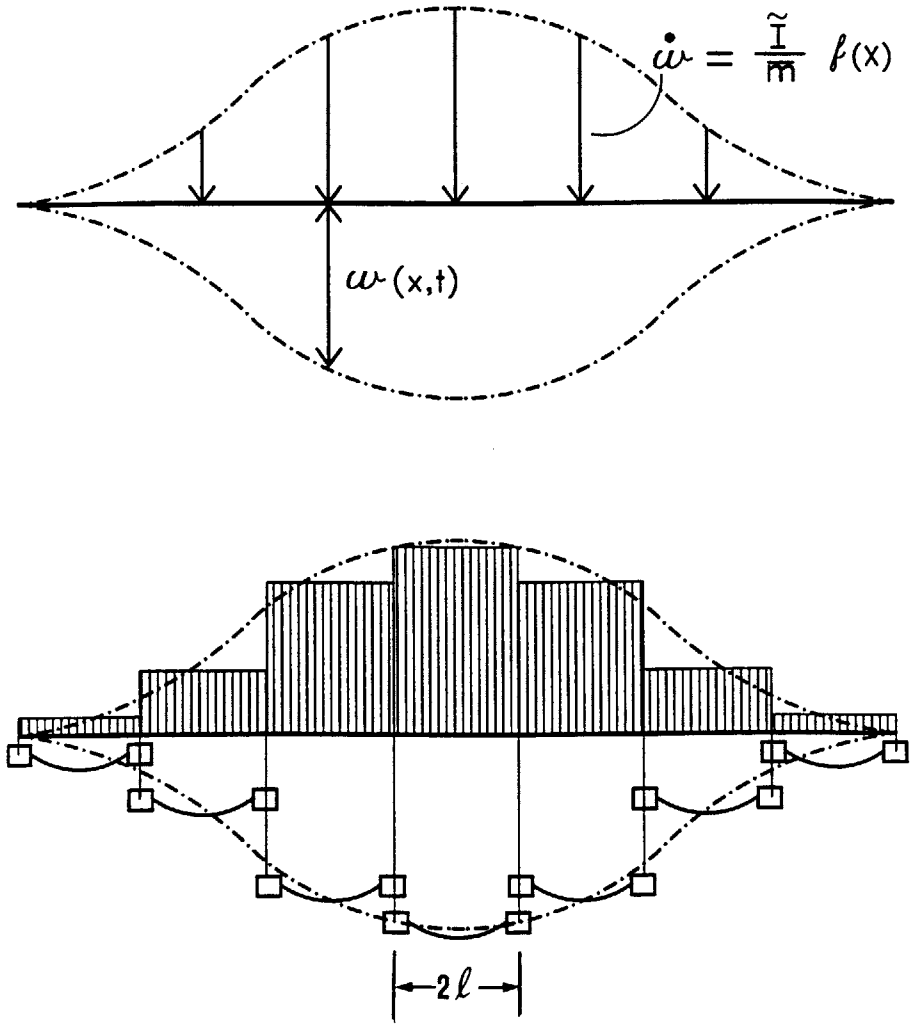

Figure 8-2: Global and local deformations of a ring-stiffened shell subjected an impulsive loading.

$$\bar{T}\dot{w}|_{end} + \int_0^l \bar{p}\dot{w}(x,t)dx = \int_0^l \bar{q}\dot{w}(x,t)dx + \int_0^l \bar{N}w'\dot{w}'(x,t)dx + \int_0^l \bar{m}\ddot{w}\dot{w}(x,t)dx. \tag{8.7}$$

After integrating the term with $w'\dot{w}'$ by parts, one gets

$$(\bar{T} - \bar{N}w')\dot{w}|_{end} + \int_0^l (\bar{m}\ddot{w} - \bar{N}w'' + \bar{q} - \bar{p})\dot{w}dx = 0. \tag{8.8}$$

Then once again the normal procedure of variational mechanics gives the partial differential equation

$$\bar{m}\ddot{w} - \bar{N}w'' + \bar{q} - \bar{p} = 0, \tag{8.9}$$

with boundary conditions

$$w' = 0 \quad \text{at } x = 0 \tag{8.10}$$

and

$$\bar{N}w' = \bar{T} = -(\bar{Q} + \bar{M}\ddot{w})/2 \quad \text{at } x = l. \tag{8.11}$$

Notice that the membrane force is equated to the sum of the inertia and the bending resistance of the stiffener. As in Chapter 7, the pressure load $\bar{p}(x,t)$ is replaced by impulsive loading conditions for which $\bar{p}(x,t) = 0$ and $\dot{w}(x,0) = \bar{V}f(x)$, where $\bar{V}$ is related to both the maximum pressure amplitude p_o and decay constant τ of a pressure pulse shock wave (see Appendix C). The advantage of replacing the pressure load by an impulse load is a one parameter representation of the pressure load.

The initial conditions to Eq. (8.9) are as follows

$$w = 0 \quad \text{at } t = 0 \tag{8.12}$$

and

$$\dot{w} = \bar{V} f(x) \quad \text{at } t = 0, \tag{8.13}$$

where $f(x)$ is a shape function used to describe the initial velocity distribution.

With $\bar{p} = 0$, Eq. (8.9) represents the inhomogeneous wave equation and the motion of the shell between stiffeners can be viewed as a rigid-plastic string resting on a rigid-plastic foundation. The boundary condition at $x = l$ shows the coupling associated with the bay and the stiffener. The stiffener is modeled as a discrete system with lumped mass $\bar{M}$ and foundation resistance $\bar{Q}$ subjected to a forcing input that is equal to the shear force transmitted from the motion of the bay. Formulating the principle of virtual velocities for the central bay has therefore enabled us to view the complex two-dimensional problem as the two coupled sub-systems shown in Figure 8-3.

The computational model of the shell, shown in Fig. 8-3, consists of two discrete elements of mass $\bar{M}$ each supported by a discrete spring of constant force $\bar{Q}$. The mass $\bar{M}$ and the spring $\bar{Q}$ represent the "equivalent" mass and crushing strength of the ring stiffener, respectively. The ring-stiffened shell is therefore modeled as a series of discrete masses and springs connected by a continuous string with an equivalent mass $\bar{m}$ and foundation constant $\bar{q}$ per unit length.

The bending resistance is calculated once a neutral axis has been located. Calculation of the neutral axis is a formidable task because its position is constantly changing and the bay and stiffeners shift relative to it. One way of dealing with this problem is to introduce a new parameter μ which is the ratio of the length of the stiffener footing $2l_1$ to the length of the bay $2l_2$. With the present model, all the bending resistance of the stiffener is lumped into one quantity $\bar{Q}$. This quantity depends on the length of the stiffener footing and how far the stiffener has shifted relative to the neutral axis (Fig. 8-4). Note that eventually the neutral axis of the stiffener coincides with that of the bay as defined by Eq. (8.5). For the stationary hinge model these differing shifts relative to the neutral axis are accommodated by small twists in the "rigid" plates between hinges. It is postulated that the choice of

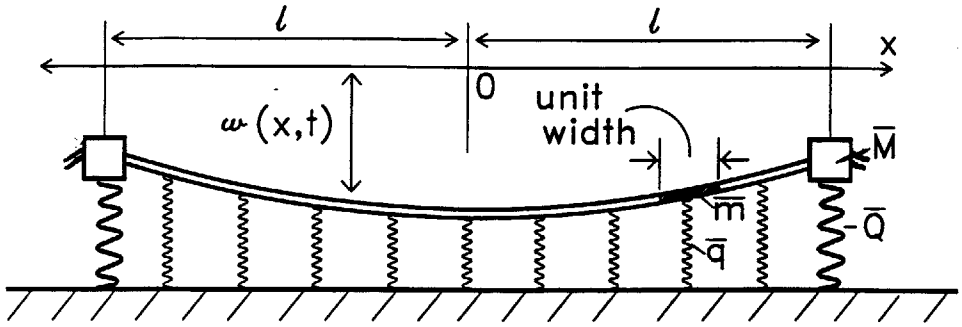

Figure 8-3: A continuous-discrete model of a single bay in the ring-stiffened shell.

parameter μ would account for these errors. However, further research on this topic should be done.

The problem of finding the "effective breadth" l_1 has been solved only for the case of elastic plates under in-plane loading [61]. A similar concept should also applies to plastic, ring-stiffened shells. Therefore, in the development of the continuous-discrete system an important decision must be made as to which part of the shell belongs to the stiffener and which to the string. As shown in Fig. 8-5, the total length of the bay is divided into the width of base of a stiffener $2l_1$ and the length of the string $2l_2$, $2l = 2l_1 + 2l_2$. There is a fair amount of arbitrariness in the division of the shell as this division varies with the deflection of the string, illustrated in Fig. 8-5. For instance, if $l_1 = 0$, then the stiffener is considered to be a "T" stiffener. On the other hand, if $l_1 > 0$, the stiffener becomes more of an "I" stiffener.

It must be pointed out that the partition of initial momentum imparted to the shell between the stiffener and bay also depends on the parameter μ. Therefore,

$$\begin{aligned} 2l_1 I &= \bar{V}_{stiff}\bar{M} \\ 2l_2 I &= \bar{V}_{shell}\bar{m}2l_2, \end{aligned} \tag{8.14}$$

where I is the uniform impulse per unit length, and $\bar{V}_{stiff}$ and $\bar{V}_{shell}$ denote the initial velocity of the stiffener (rigid mass $\bar{M}$) and the string, respectively. Furthermore, the above initial velocity field must be distributed to avoid discontinuities at $x = l_2$, as shown in Fig. 8-6.

8.1 An Exact Solution of the Partial Differential Equation

It is convenient to express the initial-boundary value problem to a set of normalized coordinates. In the normalized coordinate system, Eqs. (8.9)-(8.13) reduce to

$$\tilde{w}_{\tilde{t}\tilde{t}} - \tilde{w}_{\tilde{x}\tilde{x}} + 1 = 0, \tag{8.15}$$

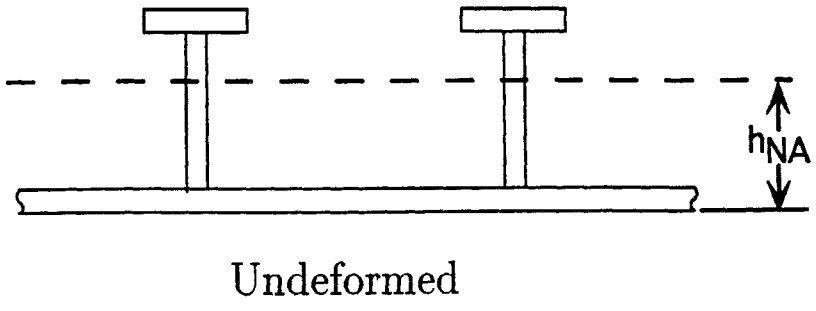

Figure 8-4: Shifting of the neutral axis.

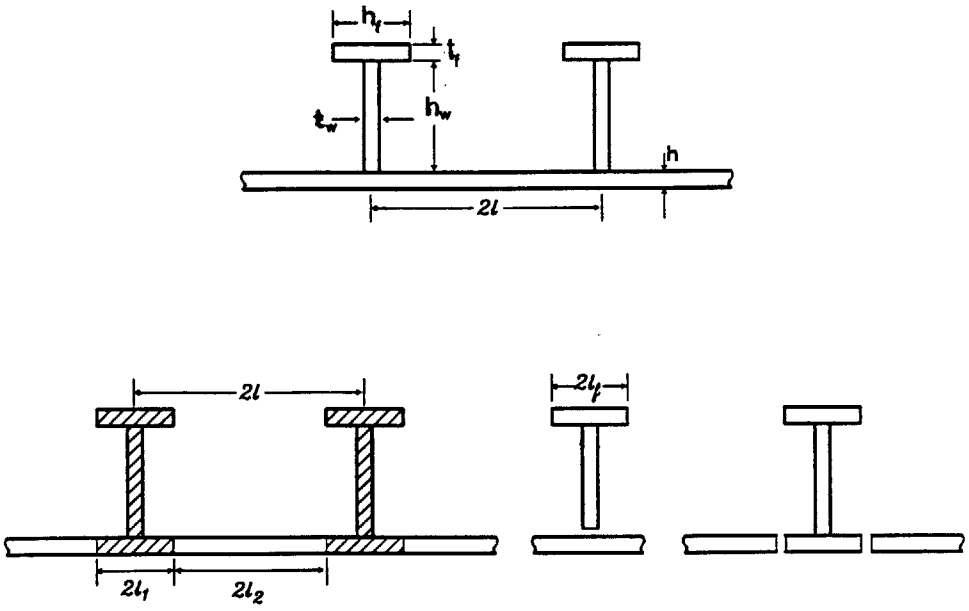

Figure 8-5: Geometry of a ring-stiffener and the concept of an effective breadth of the stiffener footing.

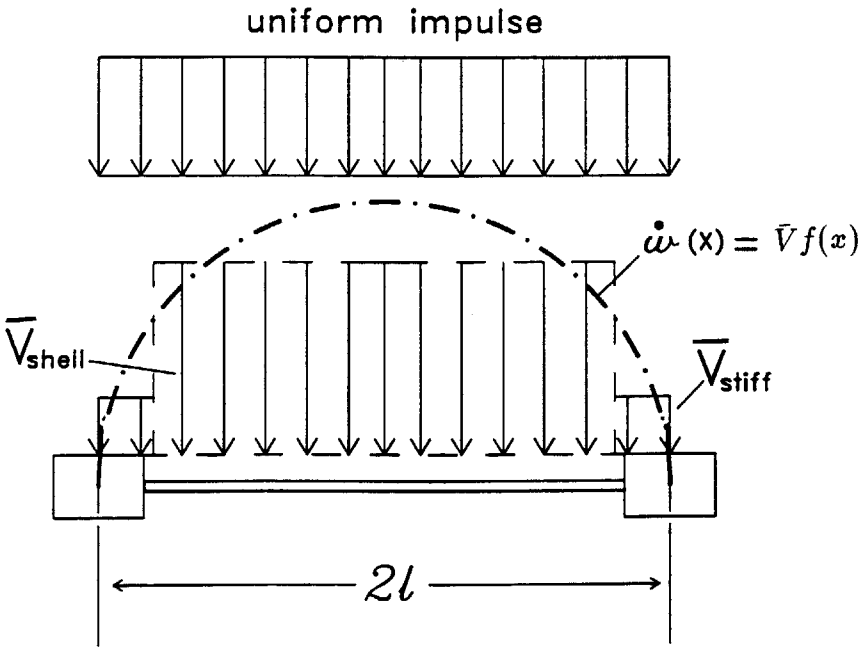

Figure 8-6: Stepwise initial velocities of the stiffener and the shell produced by a uniform impulse.

with boundary conditions

$$\tilde{w}_{\tilde{x}} = 0 \quad \text{at } \tilde{x} = 0 \tag{8.16}$$

and with $\zeta = \bar{Q}/(\bar{q}l)$ and $\eta = \bar{M}/(\bar{m}l)$,

$$\tilde{w}_{\tilde{t}\tilde{t}} + \frac{2}{\eta}\tilde{w}_{\tilde{x}} + \frac{\zeta}{\eta} = 0 \quad \text{at } \tilde{x} = 1, \tag{8.17}$$

and initial conditions

$$\tilde{w} = 0 \quad \text{at } \tilde{t} = 0 \tag{8.18}$$

and

$$\tilde{w}_{\tilde{t}} = \tilde{I} f(\tilde{x}) \quad \text{at } \tilde{t} = 0. \tag{8.19}$$

Insight from Reference [62] as well as an attempt to solve the problem using the method of characteristics reveal that the solution is of the form

$$\tilde{w} = \bar{w} + \alpha_1(1 - \tilde{x}^2) + \beta_1 \tilde{t}^2, \tag{8.20}$$

where the inhomogeneous terms in the partial differential equation and the boundary condition at $\tilde{x} = 1$ are removed if

$$\alpha_1 = \frac{(\zeta - \eta)}{2(2 + \eta)} \tag{8.21}$$

and

$$\beta_1 = \frac{-(2 + \zeta)}{2(2 + \eta)}. \tag{8.22}$$

The following describes the resulting homogeneous partial differential system:

$$\bar{w}_{\tilde{t}\tilde{t}} - \bar{w}_{\tilde{x}\tilde{x}} = 0, \tag{8.23}$$

with homogeneous boundary conditions

$$\bar{w}_{\tilde{x}} = 0 \quad \text{at } \tilde{x} = 0 \tag{8.24}$$

and

$$\bar{w}_{\tilde{t}\tilde{t}} + \frac{2}{\eta}\bar{w}_{\tilde{x}} = 0 \quad \text{at } \tilde{x} = 1, \tag{8.25}$$

and initial conditions

$$\bar{w} = -\alpha_1(1 - \tilde{x}^2) \quad \text{at } \tilde{t} = 0 \tag{8.26}$$

and

$$\bar{w}_{\tilde{t}} = \tilde{I}f(x) \quad \text{at } \tilde{t} = 0. \tag{8.27}$$

This initial-boundary value problem can be solved using the method of Fourier series expansion.

Assume a solution of the form

$$\bar{w} = \sum_{n=0}^{\infty}[F_n sin(\lambda_n \tilde{t}) + G_n cos(\lambda_n \tilde{t})]cos(\lambda_n \tilde{x}). \tag{8.28}$$

where λ_n are the eigenvalues and $cos\lambda_n\tilde{x}$ forms a complete set of symmetric orthogonal functions with respect to a special orthogonality condition. Equation (8.28) identically satisfies the partial differential equation, Eq. (8.23), and the boundary condition at $\tilde{x} = 0$, Eq. (8.24). Satisfying the boundary condition at $\tilde{x} = 1$ gives the eigenvalue equation

$$tan\lambda_n = -\frac{\eta}{2}\lambda_n. \tag{8.29}$$

The first eigenvalue is the trivial case, $\lambda_0 = 0$. All other eigenvalues depend on the mass ratio η. The initial conditions to the partial differential equation specify the coefficients of F_n and G_n. Notice that the boundary condition at $\tilde{x} = 1$ relates the

acceleration to the slope and leads to an important modification of the orthogonality condition. The special orthogonality condition for this type of boundary condition is derived in Appendix D. Therefore from Eq. (8.26), one gets

$$G_0 + \sum_{n=1}^{\infty} G_n cos(\lambda_n \tilde{x}) = -\alpha_1(1 - \tilde{x}^2). \tag{8.30}$$

and from Eq. (8.27), one finds

$$\lambda_0 F_o + \sum_{n=1}^{\infty} \lambda_n F_n cos(\lambda_n \tilde{x}) = \tilde{I} f(\tilde{x}). \tag{8.31}$$

Expressions for G_n and $\lambda_n F_n$ using the special orthogonality condition, Eq. (D.5) are derived in Appendix E.

The coefficients are given by

$$G_0 = \frac{-4\alpha_1}{3(2+\eta)}, \tag{8.32}$$

$$G_n = \frac{4\alpha_1(2+\eta)cos\lambda_n}{\lambda_n^2(2+3\eta cos^2\lambda_n)}, \tag{8.33}$$

$$\lambda_0 F_o = \frac{2\tilde{I}[\int_0^1 f(\tilde{x})d\tilde{x} + \frac{\eta}{2}f(1)]}{(2+\eta)}, \tag{8.34}$$

and

$$\lambda_n F_n = \frac{2\tilde{I}[\int_0^1 f(\tilde{x})cos(\lambda_n\tilde{x})dx + \frac{\eta}{2}cos\lambda_n f(1)]}{(1 + \frac{sin(2\lambda_n)}{2\lambda_n} + \eta cos^2\lambda_n)}. \tag{8.35}$$

Notice that the coefficients $\lambda_n F_n$ depend on the value of $f(1)$. Recall that the actual solution for the initial-boundary value problem in a normalized coordinate system is given by Eq (8.20). Therefore, the actual solution is

$$\tilde{w} = \sum_{n=0}^{\infty}[F_n sin(\lambda_n \tilde{t}) + G_n cos(\lambda_n \tilde{t})]cos(\lambda_n \tilde{x}) + \alpha_1(1 - \tilde{x}^2) + \beta_1 \tilde{t}^2, \tag{8.36}$$

where α_1, β_1, G_n, and F_n, are defined by Eqs. (8.21), (8.22), and (8.32)-(8.35). Notice that the zeroth term of F_n is singular but not $\lambda_0 F_0$. An expanded version of Eq. (8.36) is

$$\tilde{w} = \lambda_0 F_0 \tilde{t} + G_0 + \sum_{n=1}^{\infty} [F_n sin(\lambda_n \tilde{t}) + G_n cos(\lambda_n \tilde{t})] cos(\lambda_n \tilde{x}) + \alpha_1 (1 - \tilde{x}^2) + \beta_1 \tilde{t}^2. \quad (8.37)$$

8.2 Unloading

As seen from experimental profiles [47], the total deflection consists of two parts $w = w_l + w_g$. Furthermore, for the central bay, on which our analysis focuses, the global deflection w_g is described by the motion of the stiffener (see Fig. 8-3),

$$w_g = \delta_g = w(x = l, t), \quad (8.38)$$

and the motion of the bay,

$$w_l = w - w(x = l, t) = w - w_g. \quad (8.39)$$

From Eq. (8.39), one can express the maximum local deflection as $\delta_l = w_l(x = 0, t)$. It is important to keep a distinction between local and global deflections while analyzing unloading in order to understand the interplay of bay and stiffener.

For a perfectly plastic cylinder, deformation reaches its final state when the velocity vanishes, $\dot{w} = 0$, $\mathcal{L}$-boundary. However, tensile forces in the shell may start to unload before the velocity vanishes if $\dot{\epsilon} = 0$, $\mathcal{U}$-boundary. Therefore, several unloading possibilities can be distinguished, and they are summarized as follows:

If in the interval $0 < x < 1$,

1. $\dot{w} = 0$ always before $\dot{\epsilon} = 0$, then the unloading path is described by the $\mathcal{L}$-boundary and every point in the bay reaches final deflection when $\dot{w} = 0$.

2. $\dot{w} = 0$ occurs before $\dot{\epsilon} = 0$ for some but not all x, then the $\mathcal{L}$- and $\mathcal{U}$-boundaries meet at some points. Given a Fourier series expansion for the transient deflec-

tion profiles, a solution for the final deformation profile becomes complicated and will not be pursued any further.

3. $\dot{\epsilon} = 0$ before $\dot{w} = 0$, the $\mathcal{U}$-boundary is met before the $\mathcal{L}$-boundary. Local deflection ceases while global deformation continues. Unloading always starts at $x = 0$ and propagates towards the stiffener at $x = l$. Local motion ceases because the tensile forces N in the bay are less than the fully plastic tensile force $\bar{N}$ so that no additional stretching can take place. The resulting bay must therefore move as a rigid body with constant but reduced tensile force N. When this happens, the deformed shell enters Phase II corresponding to rigid body translation of the string. Phase I is used to describe the deformation history before any unloading takes place. Phase II unloading will be pursued in Section 8.3.2 with a two-term Fourier series approximation for the transient deformation of the shell.

8.3 Experimental Validation

The proposed methodology will now be applied to a ring-stiffened cylinder undergoing explosive or shock wave loading over its entire length $L = 165 \ \ in.$ It is worthwhile to mention that an engineering approximation to this problem using modal analysis has already been proposed [46]. Figure 8-7 shows some experimental profiles of a ring-stiffened cylindrical shell resulting from three consecutive underwater explosion [47]. Since the proposed analysis is based on an undamaged shell, only data from the first of these explosions is used. The second and the third explosions act on an already damaged shell. Notice that after the third explosion, the shell undergoes very large deformation and ruptures. The shell and stiffener dimensions are shown in Figure 8-8.

The assumed pressure distribution is given by Eq. (7.1). The magnitudes of p_o and τ which result from each explosion are given in Table 8.1. The material flow stress σ_o is $52,200 \ \ psi$ and the density ρ is $0.27 \ \ lbm/in^3$.

While the amplitude of the pressure distribution varies in x, it is roughly constant

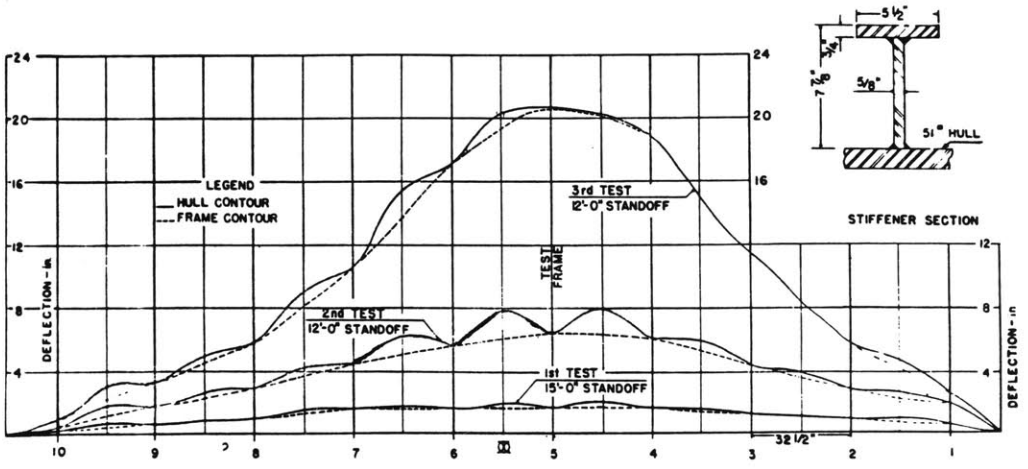

Figure 8-7: Experimental profiles.

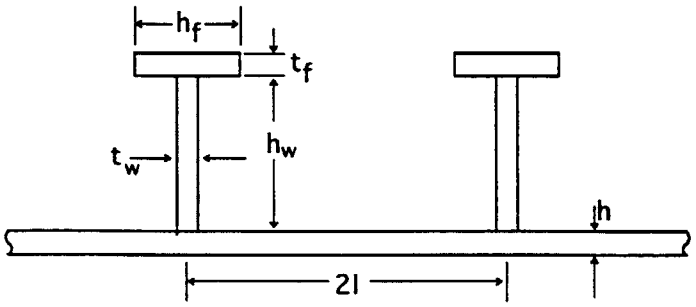

Shell dimensions

R	h	L	l
101.5in	1.25 in	165.0in	16.25 in

Dimensions of T-stiffener

t_w	h_w	h_f	t_f
0.625in	7.125 in	5.5 in	0.75 in

Figure 8-8: Stiffener dimensions.

between stiffeners. The constant local pressure amplitude in the central bay is given by

$$P_l = \frac{p_o}{l} \int_0^l cos^2(\frac{\pi x}{2L}) dx. \tag{8.40}$$

The mass $\bar{M}$ and bending resistance $\bar{Q}$ of the stiffener must be evaluated in order to calculate the deformation of the shell. These depend on the geometry of the stiffeners and are evaluated in Appendix F for the given ring-stiffened shell, taking $l_1 = t_w$.

A parabolic shape function is assumed for the shape of the initial velocity distribution $f(x)$

$$\dot{w} = \bar{V}(1 - (x/l)^2) \quad \text{at } t = 0, \tag{8.41}$$

where $\bar{V} = 3I/2\bar{m}$ is the amplitude of the velocity calculated so that the total momentum imparted to the shell is equal to the initial shell momentum calculated by a parabolic velocity (see Appendix C). A parabolic distribution in the initial velocity is assumed because it is expected that the initial velocity would be small at the stiffener. This is because stiffeners generally have a greater mass than the bay and therefore initially more inertial resistance. Hence, the initial transfer of momentum would be such that the initial velocity at the stiffener is much less than at the center of the bay. Given the initial velocity distribution represented by Eq. (8.41), $f(1) = 0$ and the coefficients for F_n are similar to those of G_n,

$$\lambda_n F_n = \frac{-G_n \tilde{I}}{\alpha_1}. \tag{8.42}$$

Table 8.2 shows some calculated quantities associated with the first explosion. Notice that the calculated value of η is 1.45 so that the mass of the stiffener is only 45 percent greater than that of the bay. The assumption of a parabolic distribution for the initial velocity (zero initial velocity at the stiffener) should therefore lead to some inaccuracies of the model. In a more refined model, a finite velocity should occur at the stiffener. The first ten eigenvalues calculated for a chosen mass ratio $\eta = 1.45$ are

Table 8.1: Pressure loadings

Explosion No.	p_o	τ
1	6359.0 psi	0.367 msec
2	8209.0 psi	0.348 msec
3	8209.0 psi	0.348 msec

given in Table 8.3.

8.3.1 Motion before unloading: Phase I

It was found that a two term approximation (n = 0,1) of the solution for the deflection converges rapidly because the Fourier coefficients G_n are inversely proportional to λ_n^2 (see Eq. (8.33)), and a good approximation (within 15 percent for the value of the maximum central deflection) is

$$\tilde{w} = F_0\lambda_0\tilde{t} + G_0 + [F_1 sin(\lambda_1\tilde{t}) + G_1 cos(\lambda_1\tilde{t})]cos(\lambda_1\tilde{x}) + \alpha_1(1-\tilde{x}^2) + \beta_1\tilde{t}^2. \quad (8.43)$$

The velocity is then

$$\tilde{w}_{\tilde{t}} = F_0\lambda_0 + [F_1\lambda_1 cos(\lambda_1\tilde{t}) - G_1\lambda_1 sin(\lambda_1\tilde{t})]cos(\lambda_1\tilde{x}) + 2\beta_1\tilde{t}. \quad (8.44)$$

Upon differentiating Eq. (8.43) with respect to both time and space, one gets

$$\tilde{w}_{\tilde{t}\tilde{x}} = -[F_1\lambda_1 cos(\lambda_1\tilde{t}) - G_1\lambda_1 sin(\lambda_1\tilde{t})]sin(\lambda_1\tilde{x}). \quad (8.45)$$

This two-term approximation greatly simplifies the unloading analysis and with a two-term approximation (ie. $\dot{\epsilon} = 0$ before $\dot{w} = 0$), the $\mathcal{U}$-boundary always occurs before the $\mathcal{L}$-boundary. In fact, unloading takes place instantaneously at a critical time $\tilde{t}_c$. From the condition that $\dot{\epsilon} = 0$ and Eq. (8.45), the $\mathcal{U}$-unloading boundary occurs instantaneously at

Table 8.2: Calculated quantities for the shell.

$\bar{m}$	$\bar{M}$	$\bar{q}$	$\bar{Q}$	$\bar{N}$	Θ_0	η	ζ	$\bar{I}$
15.38 lbm/in	361.64 lbm	1607.14 lb/in	94588.01 lb	3,467,729.24 lb	1.5	1.45	3.62	17.95

$$\tilde{t}_c = \frac{1}{\lambda_1} tan^{-}1(\frac{-\tilde{I}}{\lambda_1 \alpha_1}). \tag{8.46}$$

This type of unloading leads to rigid body translation because no additional extensional plastic deformation can take place within the bay. For $\tilde{t} > \tilde{t}_c$, motion in Phase II begins.

The normalized transient deflection and velocity profiles for the central bay in Phase I which result after the first explosion are shown in Figs. 8-9 and 8-10. The local deflections increase more rapidly than the global deflection at the stiffener in Phase I because a greater initial velocity is given to the bay than to the stiffener. Notice that the initial velocity distribution in Fig. 8-10 is not precisely a parabolic function as a consequence of the two-term approximation.

8.3.2 Motion after unloading: Phase II

For simplicity, rigid body deflection will be derived in physical variables and later represented in normalized coordinates. If the rigid body deformation of the bay in Phase II is denoted w_b, the new equation of motion for the bay is

$$\bar{m} l \ddot{w}_b - N w_c' + \bar{q} l = 0, \tag{8.47}$$

where w_c' is a constant and depends on the solution of the previous analysis, $w_c' = w'(l, t_c)$, and $N < \bar{N}$ is the new value of the tensile force. Notice that Eq. (8.47) is no longer a partial but a second order ordinary differential equation in time t because w_b is only a function of t. At $t = t_c$, the velocity is given by $\dot{w}_b(t_c) = \dot{w}(l, t_c)$. The final deflection and velocity in Phase I provides initial deflection and velocity in Phase II.

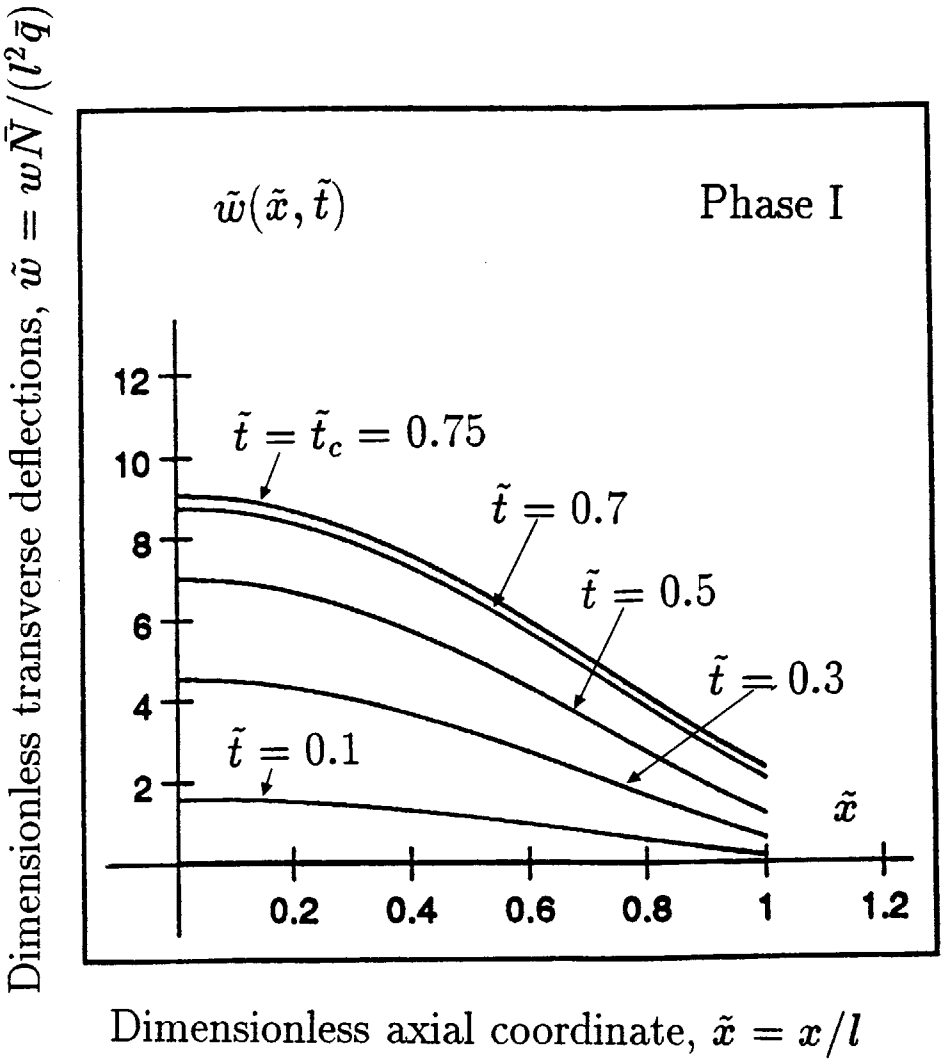

Figure 8-9: Normalized transient deflection profiles within the central bay.

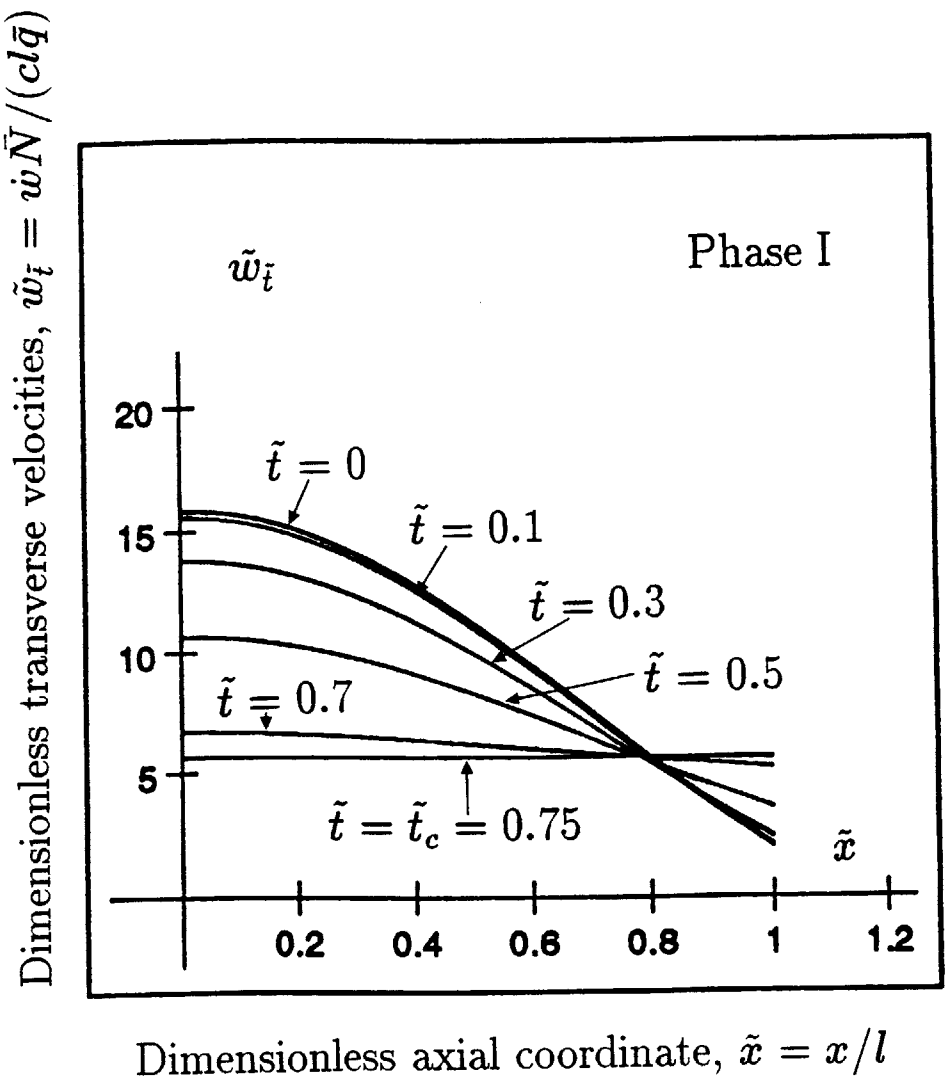

Figure 8-10: Normalized transient velocity profiles within the central bay.

The boundary condition imposed at $x = l$ can also be interpreted as rigid body motion of the stiffener. In Phase II, therefore,

$$\bar{M}\ddot{w}_b + \bar{Q} + 2Nw_c' = 0. \tag{8.48}$$

Eliminating $\ddot{w}_b$ from Eqs. (8.47) and (8.48) gives

$$N = \frac{(\bar{M}\bar{q} - \bar{m}\bar{Q})l}{(\bar{M} + 2\bar{m}l)w_c'} \tag{8.49}$$

or in normalized coordinates,

$$N = \frac{(\eta - \zeta)}{(2+\eta)\tilde{w}_c'}\bar{N}. \tag{8.50}$$

The tensile force between bay and stiffener therefore adjusts itself to a constant value N. A necessary condition for the development of Case 3 ($\dot{\epsilon} = 0$ before $\dot{w} = 0$) is that $N < \bar{N}$ or $\frac{(\eta-\zeta)}{(2+\eta)\tilde{w}_c'} < 1$.

Equation (8.49) is substituted into either Eqs. (8.47) or (8.48), and $\ddot{w}_b$ is integrated twice with respect to time to give in normalized coordinates

$$\tilde{w}_b = \frac{-(2+\zeta)}{2(2+\eta)}\tilde{t}^2 + b_1\tilde{t} + b_2, \tag{8.51}$$

where b_1 and b_2 are evaluated at the end of Phase I so that

$$b_1 = \tilde{w}_{\tilde{t}}(\tilde{t}_c) = \lambda_0 F_0 + \frac{[2\beta_1(2+\eta) + 2 + \zeta]}{(2+\eta)}\tilde{t}_c \tag{8.52}$$

and

$$b_2 = \tilde{w}(\tilde{t}_c) = G_0 - \frac{[2\beta_1(2+\eta) + 2 + \zeta]}{2(2+\eta)}\tilde{t}_c^2 + cos\lambda_1\sqrt{(G_1^2 + F_1^2)}. \tag{8.53}$$

An engineering approximation to this same problem was also done on the basis of modal analysis [46]. The stiffener footing in the modal solution was such that $2l_1 = t_w$ or $\mu = 0.020$. Due to uncertainties in the quoted values of p_o and τ, the actual distribution of the pressure load in the circumferential direction, and an accurate

value for the stiffener width, the value of $\bar{I}$ was adjusted to match the experimental curve. The uncertainties associated with the loading arise from a complicated fluid-solid interaction, not considered in the present model. Caution must be advised when correlating the experimental results from an underwater explosion to a theory that does not consider the fluid-solid interaction. Even though the peak amplitude p_o and time constant τ used in this analysis are believed to represent the contact pressure acting on the shell rather than the free field pressure, more research needs to be done to clarify this point.

The transient profiles of the central bay predicted by modal analysis is compared to the experimental profile resulting from the first explosion in Fig. 8-11. The difference in magnitude of the maximum central deflection of the bay using modal analysis and that of the one presented here is only 8 percent. The same plot using the two-term series approximation would be similar with only about 10 percent difference in deflection at any location. The modal approximation predicted the ratio of maximum local to global deflection rather well for the specified value of $\bar{I}$. The experimental value for the ratio of maximum local to global deflection is 1:3, while the analytical model predicts this ratio to be roughly 1:2. Under the assumption that the adjusted value for the impulse compensated for the fluid-solid interaction, it is speculated that the above discrepancy results from: (1) application of a zero initial velocity to the stiffener (parabolic distribution assumption for the initial velocity distribution), (2) the effect of the stiffener footing, and (3) the neglect of bending work rate of the shell in the longitudinal direction, $M_{xx}\dot{\kappa}_{xx}$. The first and second factors are related to each other. The last two influencing factors will be explained in following sections.

It should also be mentioned that if one were to use the quoted values for p_o and τ, a stiffener width of $2l_1 = t_w$, and the circumferential pressure distribution described in Appendix B, then the model will underpredict the deflection profile by roughly an order of magnitude when compared to the experimental data. Conceivable effects due to a change in the stiffness parameter with defromation do not appear to account for this discrepancy [63].

Table 8.3: First ten eigenvalues calculated for the mass ratio $\eta = 1.45$.

λ_0	λ_1	λ_2	λ_3	λ_4	λ_5	λ_6	λ_7	λ_8	λ_9
0	2.14	4.98	8.02	11.1	14.2	17.3	20.4	23.6	26.7

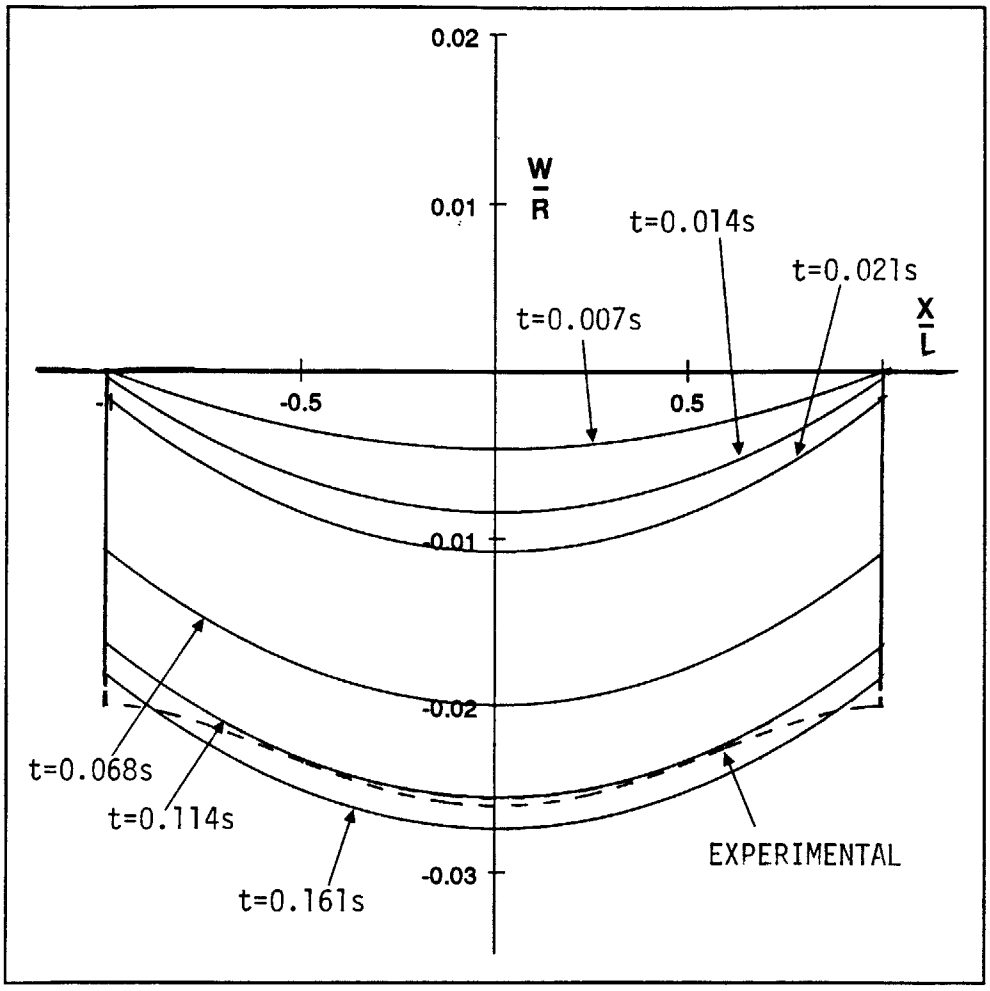

Figure 8-11: Transient deflection profiles for the central bay (using modal analysis).

8.3.3 Effect of stiffener footing

The final deflection profiles for various values of μ are shown in Fig. 8-12. Caution must be taken when performing such a parametric study because the eigenvalues given by Eq. (8.29) depend on η, which in turn is a function of both l_1 and l_2. Furthermore, as more of the shell is allotted to the stiffener, the assumption of a parabolic distribution for the initial velocity should improve the analysis because the stiffener will have a greater initial inertia resistance.

Global amplitudes diminish as the stiffener footing increases. However, notice from Fig. 8-12 that as the stiffener width increases the local deformation increases because the stiffness ratio ζ increases more rapidly than mass ratio η and that by adjusting the stiffener footing such that $2l_1 = 2 \ \ in$, the predicted final displacement can be brought closer to experimental results.

8.3.4 Neglect of bending work rate in the axial direction

The assumption that $\dot{\kappa}_{xx} = 0$ is justified for the overall (or global) shell deformations that extend over several bays. In the global deformation mode, changes in the axial curvature are indeed very small. However, at the level of a single bay, the curvature κ_{xx} changes sign twice within a relative short distance l and this assumption would be violated. A simple estimate of the ratio of the rate of bending work to membrane work in the bay, per unit length in the circumferential direction is

$$\frac{\dot{W}_b}{\dot{W}_m} = \frac{\int_0^l M_{xx}\dot{\kappa}_{xx}dx}{\int_0^l N_{xx}\dot{\epsilon}_{xx}dx} = \frac{h}{2\delta_l}. \tag{8.54}$$

Therefore, for impulses resulting in the local deflection δ_l of the order of shell thickness, the bending work rate may be substantial. This is precisely the case with the experimental data on the first explosion for which $(\delta_l)_{exp} = 0.6 \ \ in = 0.5h$. The inclusion of bending resistance would also cause the prediction of the bay deformation to be closer to experimental results both in terms of the amplitude and shape. However, the error associated with the neglect of longitudinal bending will diminish with large impulses and especially impulses that would cause shell rupture.

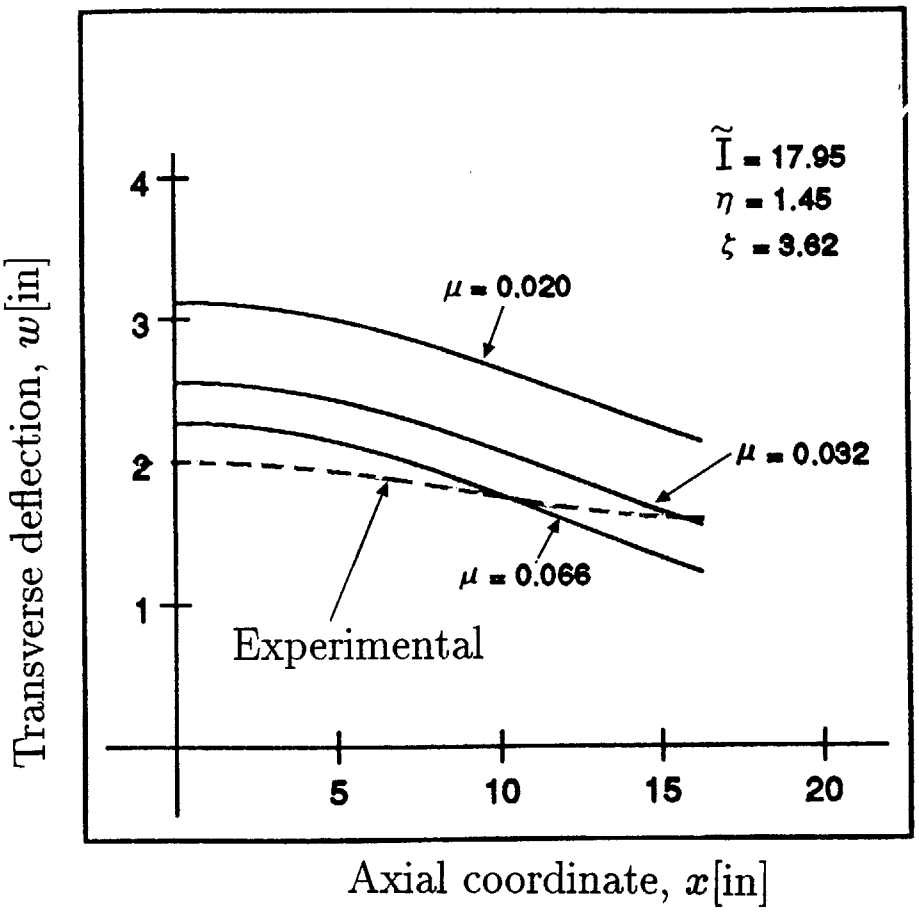

Figure 8-12: Final deflection profiles for varying stiffener footing.

8.4 Calculations of Strain Fields and Fracture Initiation

A criterion for the onset of shell rupture can be based on strains. The tensile strain within each bay is expressed by

$$\epsilon = u' + \frac{1}{2}(w')^2. \tag{8.55}$$

Recall that $u \approx 0$. For the two-term approximation, the normalized strain distribution in the shell is therefore be given as

$$\tilde{\epsilon} = \frac{1}{2}\tilde{w}_{\tilde{x}}^2 \tag{8.56}$$

where $\tilde{\epsilon} = (\frac{l}{x_o})^2\epsilon$. The maximum slope would occur at the stiffener and at time $\tilde{t} = \tilde{t}_c$. Substituting values for the first Fourier coefficients, one finds that

$$\tilde{w}_{\tilde{x}}(\tilde{x} = 1, \tilde{t} = \tilde{t}_c) = \frac{-4(2+\eta)sin\lambda_1 cos\lambda_1 \sqrt{(\tilde{I}^2 + \alpha_1^2\lambda_1^2)}}{\lambda_1^2(2 + 3\eta cos^2\lambda_1)} - 2\alpha_1. \tag{8.57}$$

A simple fracture criterion such as $\epsilon \rightarrow \epsilon_c$, where ϵ_c is a measure of the critical rupture strain, is used to find the condition for first rupture

$$\frac{d}{d\tilde{x}}\tilde{w}(\tilde{x} = 1, \tilde{t} = \tilde{t}_c) = \frac{x_0}{l}\sqrt{2\epsilon_c}, \tag{8.58}$$

From Eqs. (8.57) and (8.58), the following failure criterion is proposed for the stiffened shell

$$\frac{x_0}{l}\sqrt{2\epsilon_c} = \frac{4(2+\eta)sin\lambda_1 cos\lambda_1 \sqrt{(\tilde{I}_c^2 + \alpha_1^2\lambda_1^2)}}{\lambda_1^2(2 + 3\eta cos^2\lambda_1)} + 2\alpha_1, \tag{8.59}$$

where $\tilde{I}_c$ is the critical impulse that would cause the shell to rupture at the stiffener. In the limiting care of $\zeta = \eta$, $\alpha_1 = 0$ and the above criterion reduces to

$$\frac{x_0}{l}\sqrt{2\epsilon_c} = \frac{4\tilde{I}_c(2+\eta)sin\lambda_1 cos\lambda_1}{\lambda_1^2(2 + 3\eta cos^2\lambda_1)}. \tag{8.60}$$

Equations (8.59) and (8.60) relate the critical impulse $\tilde{I}_c$ to all other known parameters of the stiffened shell. Equation (8.60) is coverted to physical quantities, and thus a critical impulse to rupture $\bar{I}_c$ is

$$\bar{I}_c = \frac{\lambda_1^2(2 + 3\eta \cos^2 \lambda_1)}{4(2+\eta) sin\lambda_1 \cos \lambda_1} c\sqrt{2\epsilon_c}. \tag{8.61}$$

Note that the critical strain enters the above expression in the power 1/2. Therefore, the critical impulse to rupture depends weakly on ϵ_c but strongly on geometrical parameters of the problem.

In the general case of $\eta \neq \zeta$, $\bar{I}_c$ depends in a complex way on the mass and stiffness parameters. The definitions of those parameters involve the length of the bay l, the width of the stiffener footing l_1, and the geometry of the ring stiffener. Therefore Eq. (8.59) can be used to optimize an explosively load shell against rupture. This will be the subject of future research.

8.5 A Parametric Study

The simple model will now be tested by performing a parametric study on a few chosen parameters. These parameters include the impulse velocity $\bar{V}$, which incorporates both the pressure amplitude and time constant; the bending resistance of the stiffener $\bar{Q}$; and the mass of the stiffener $\bar{M}$.

It is first necessary to represent both the final local and global deflections in terms of the normalized parameters ν, η, and ζ. The final global deflection occurs at $\tilde{t} = \tilde{t}_f$, where $\tilde{t}_f$ is given by

$$\tilde{t}_f = \frac{b_1(\eta + 2)}{(2 + \zeta)}. \tag{8.62}$$

Hence, the final global deflection $\tilde{\delta}_{gf}$ is

$$\tilde{\delta}_{gf} = \frac{b_1^2(\eta + 2)}{2(2 + \zeta)} + b_2, \tag{8.63}$$

where b_1 and b_2 are defined in Eqs (8.52) and (8.53). Notice that $\tilde{\delta}_{gf}$ will directly

depend on $\bar{I}$, and vary with η and ζ in a complicated manner.

On the other hand, the final local deflection $\bar{\delta}_{lf}$ occurs at $\bar{t} = \bar{t}_c$ or at the end of Phase 1 and is given by

$$\bar{\delta}_{lf} = \alpha_1 + \frac{4(2+\eta)cos\lambda_1(1-cos\lambda_1)\sqrt{(\bar{I}^2+\lambda_1^2\alpha_1^2)}}{\lambda_1^3(2+3\eta cos^2\lambda_1)} \tag{8.64}$$

Again $\bar{\delta}_{lf}$ will depend on $\bar{I}$, η, and ζ.

Figures 8-13 - 8-15 show how the maximum global and local deflections vary for the impulse parameter $\bar{I}$, mass parameter η, and stiffness parameter ζ, respectively. It should be mentioned that for a given ring-stiffener with specified dimensions and material properties (ρ and σ_o) such as the T-stiffener in the experimental data, ζ and η are not totally independent of each other. While ζ is directly proportional to σ_o, η is proportional to ρ, and both depend on the shape of the stiffener. However, for the purpose of a parametric study, each will be fixed while the other is allowed to vary.

As shown in Fig. 8-13, both local and global deflections increase with increasing impulse loading for the given ring-stiffened shell. A minimum impulse is needed to actually start global motion and global deflections increase more rapidly than local deflections for greater impulse values. A minimum impulse is necessary to create tensile forces large enough to drive the stiffener mechanism.

In contrast to Fig. 8-13, the variation in local and global deflections are not the same for increasing mass parameter. Keeping the applied impulse and ζ parameter constant as in Fig. 8-14, shows how the maximum deflections vary for different values of η. As the stiffeners become heavier with respect to the bay, local deformations are more pronounced while global deflections diminish.

Finally, the variation of global and local deformation with stiffness parameter is studied in Fig. 8-15. Again the impulse and η parameter are kept constant, while the stiffness parameter is allowed to vary. When $\zeta = 0$, the stiffener has no resistance to bending and the global deformation is a maximum. Theoretically, local deflections should be negligible at $\zeta = 0$, but this is not shown in Fig. 8-15 because the mass of the stiffeners was fixed, $\eta = 1.45$. When the stiffness ratio is large, local

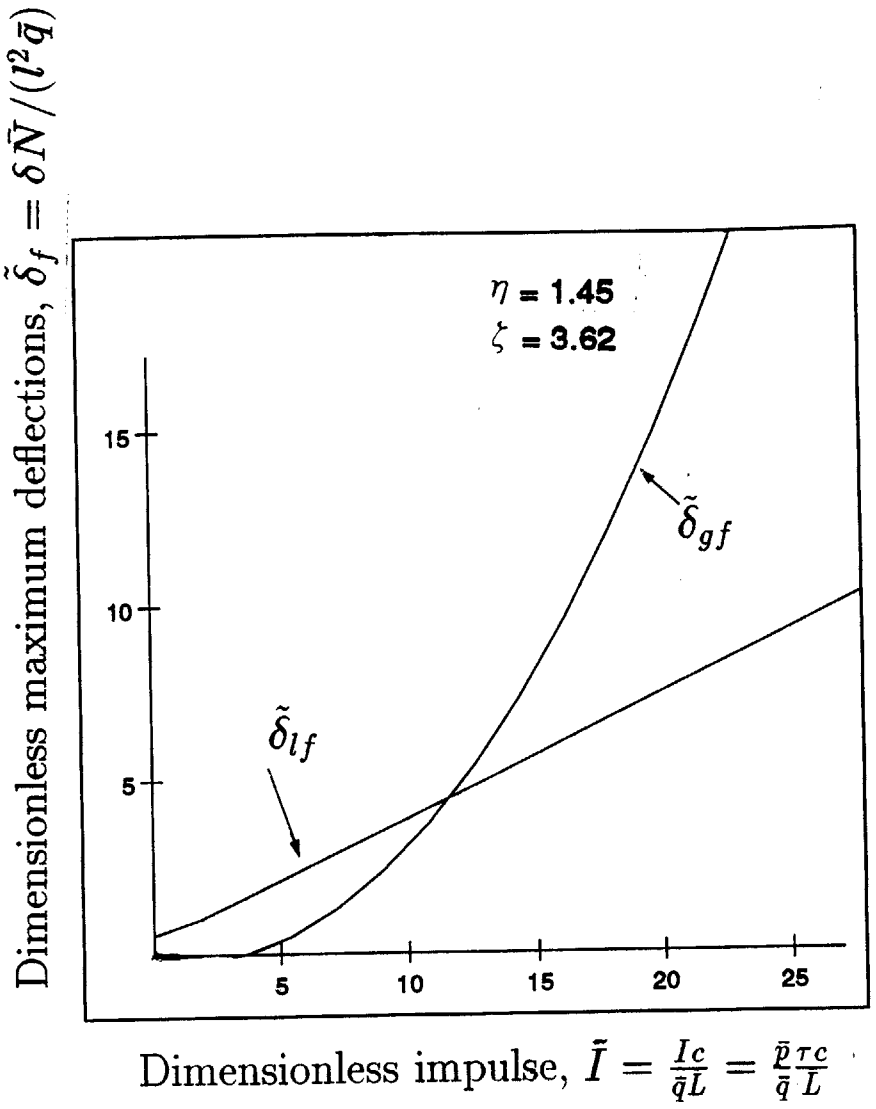

Figure 8-13: Maximum deflection v. impulse parameter.

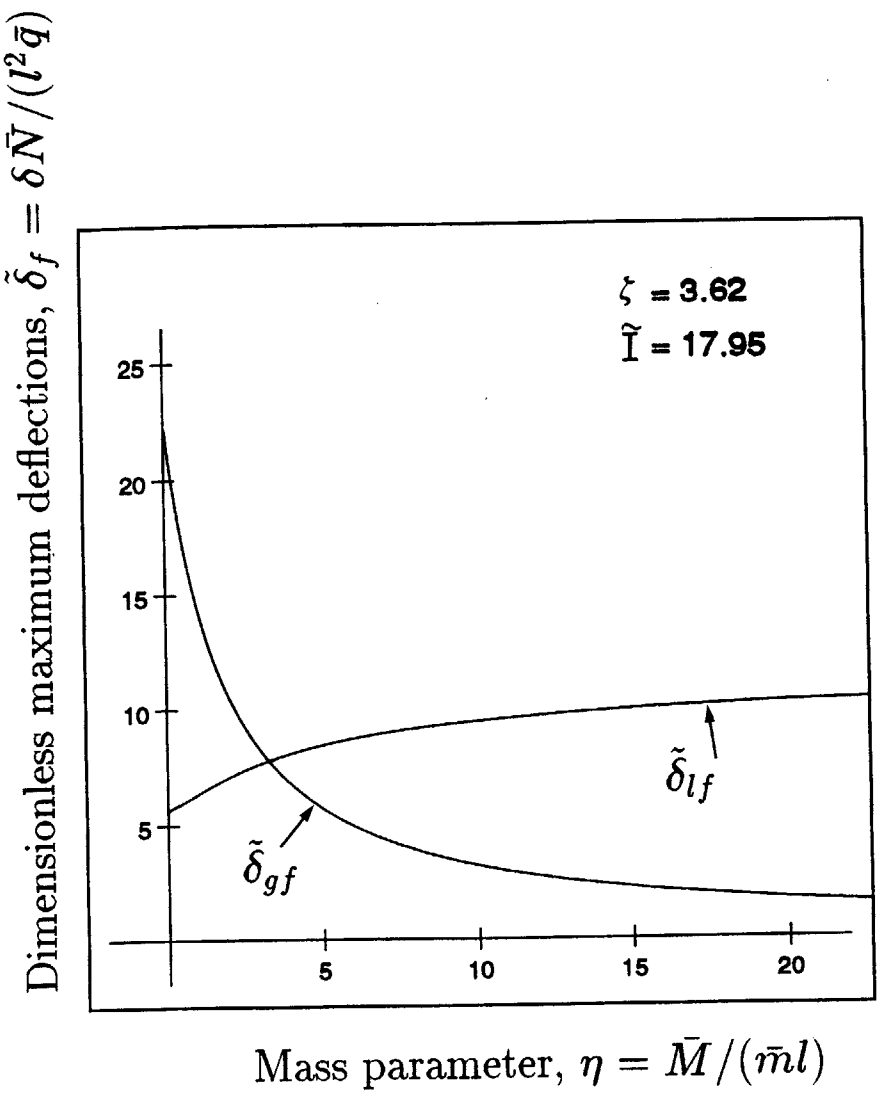

Figure 8-14: Maximum deflection v. mass parameter.

deflections become more prevalent and may even be greater than global deflections. Theoretically, an infinite stiffener resistance would prevent any global deformation and only cause local deformation to take place.

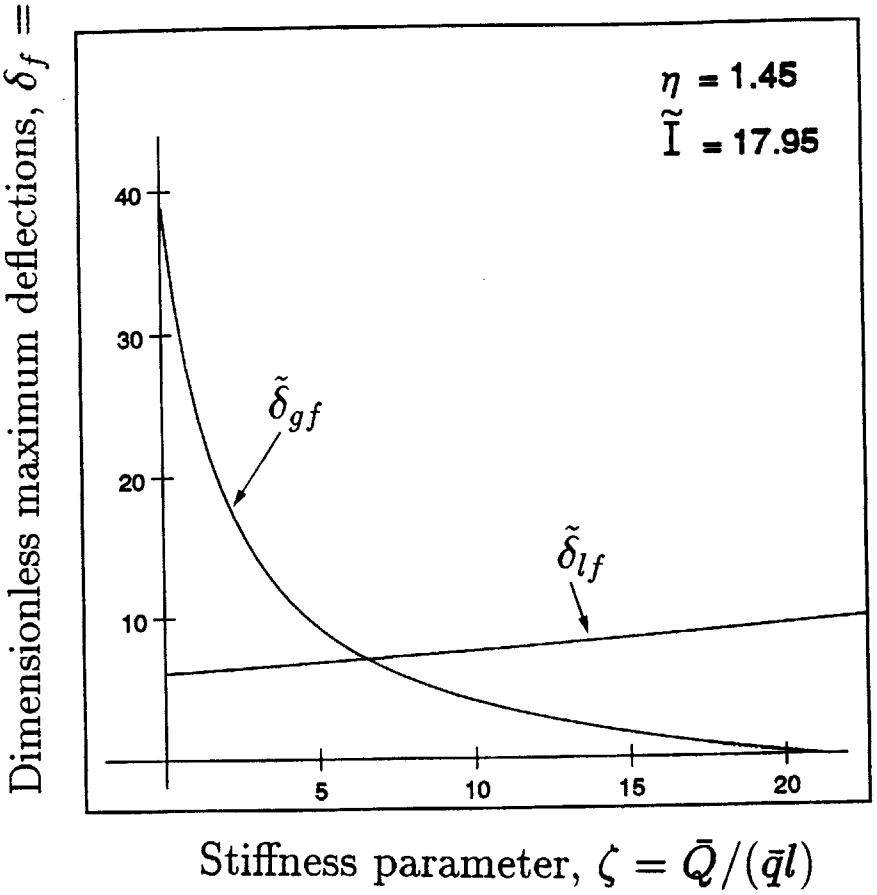

Figure 8-15: Maximum deflection v. stiffness parameter.

Chapter 9

Conclusions

A string-on-foundation model has been developed to study the large local non-axisymmetric plastic deformations of cylindrical shells resulting from impact and explosive loading. As a result of rigorously derived assumptions and simplifications of the shell, the model considers two main load-resisting mechanisms in the shell, stretching in the longitudinal direction and bending in the circumferential direction. An averaging procedure in the circumferential direction of the shell was used to eliminate one spatial variable. This averaging procedure led to the derivation of equivalent functions, which were later realized to be equivalent parameters (constants). The problem was then reduced to the solution of an inhomogeneous, partial differential equation in the axial direction and time. Closed-form solutions to three particular initial-boundary value problems were then derived: rigid mass impact on an infinite cylinder; dynamic pressure pulse loading on an unstiffened shell; impulsive loading on a ring-stiffened shell. In all cases closed-form solutions of the problem were derived and on that basis approximate engineering solutions were developed.

The conclusion drawn from the detailed analysis of all the cases considered is that the string-on-foundation is a powerful model for predicting the transient, plastic response of cylindrical shell. To the best of authors' knowledge, such simple, analytical solutions have never been reported in the open literature. The string-on-foundation model reveals the important groups of parameters that control the behavior of the shell under the prescribed dynamic loading and provides valuable insight into the

physics of the problem. Considering the simplicity of the method, the accuracy of the predicted deflection profiles was surprisingly good. The string-on-foundation model may be used for estimating the amount of structural damage to tubes, pipes, and cylinders and for serving as benchmark solutions to more refined numerical calculations. Furthermore, the fact that the present methodology gave a rather accurate description of the displacement and velocity fields in the shell offers the possibility of predicting the onset of fracture using the shear plugging or tensile necking failure criteria. Simple formulas were derived using these two fracture criteria for the ballistic limit and the critical impulse to rupture. However, further experimental validation of the theory is desirable to confirm and/or improve various approximations made in the development of the model.

One particular area for improvement in the study of projectile impact into the unstiffened shell is to incorporate some of the local energy dissipated in the vicinity of the projectile penetration into the statement of global equilibrium. This is especially important for a cylinder undergoing high velocity impact because the deformation zone tends to become more localized with increasing impact velocity. Given a localized deformation zone, the contribution of local energy would be significant and would lead to large errors if not considered. In regards to the stiffened shell undergoing underwater explosive loading, both the fluid-solid interaction and the effect of a shifting neutral axis (treated here as an effective stiffener width) should undergo further investigation before any reasonable comparison can be made with experimental results.

Appendix A

Kinematics of the Stationary Hinge Model

During deformation each material point in the ring undergoes displacement which will be represented here in vector notation $\vec{w}$, as shown in Fig. 4-4. Therefore,

$$\vec{w} = \Delta x\hat{i} + \Delta y\hat{j}, \tag{A.1}$$

where $\hat{i}$ and $\hat{j}$ are unit vectors in the rectangular coordinates. The magnitude of this vector is given by $|\vec{w}| = w(\theta)$, where θ is the location of each point on the original cross-section.

Displacements are calculated in two regions as follows:

(i) $0 < \theta < (\pi - \alpha_o)/2$

With reference to Fig. 4-4, a point in this region moves from Q to Q'. The final motion in this region consists of two parts, translation and rotation. The deflections due to translation are found by considering the relative motion of point B. The translational components are therefore given by

$$\Delta x_t = l_o(sin\phi - sin\phi_o) \tag{A.2}$$

and

$$\Delta y_t = l_o(cos\phi - cos\phi_o), \tag{A.3}$$

where $l_o = 2Rcos(\alpha_o + \phi_o)$. The components due to rotation about B' is also given by

$$\Delta x_r = -2Rsin(\frac{2\phi_o + \alpha_o - \theta}{2})[cos(\beta + \frac{\theta}{2}) - cos(\beta_o + \frac{\theta}{2})] \tag{A.4}$$

and

$$\Delta y_r = 2Rsin(\frac{2\phi_o + \alpha_o - \theta}{2})[sin(\beta + \frac{\theta}{2}) - sin(\beta_o + \frac{\theta}{2})]. \tag{A.5}$$

The rotation term Δx_r is negative because of clockwise rotation about hinge B. The net displacement is

$$\vec{w} \cdot \vec{w} = w^2 = (\Delta x_t + \Delta x_r)^2 + (\Delta y_t + \Delta y_r)^2 \tag{A.6}$$

or after some algebra, the normalized deflection is given by

$$(\frac{w}{R})^2 = 16cos^2(\alpha_o + \phi_o)sin^2(\frac{\phi - \phi_o}{2}) + 16sin^2(\frac{(2\phi_o + \alpha_o - \theta)}{2})sin^2(\frac{\beta - \beta_o}{2})$$
$$-32cos(\alpha_o + \phi_o)sin(\frac{2\phi_o + \alpha_o - \theta}{2})sin(\frac{\phi - \phi_o}{2})sin(\frac{\beta - \beta_o}{2})sin(\frac{\phi + \phi_o - \beta - \beta_o - \theta}{2}) \tag{A.7}$$

(ii) $(\pi - \alpha_o)/2 < \theta < \pi - \alpha_o$

Material in this region undergoes only rigid body rotation from point P to point P', as shown in Fig. 4-4. The x and y component are thus given by

$$\Delta x = 2Rcos(\frac{\alpha_o + \theta}{2})[sin(\phi + \phi_o - (\frac{\alpha_o - \theta}{2})) - sin(2\phi_o - (\frac{\alpha_o - \theta}{2}))] \tag{A.8}$$

and

$$\Delta y = 2Rcos(\frac{\alpha_o + \theta}{2})[cos(\phi + \phi_o - (\frac{\alpha_o - \theta}{2})) - cos(2\phi_o - (\frac{\alpha_o - \theta}{2}))]. \qquad (A.9)$$

Again the resultant deformation is given by

$$\vec{w} \cdot \vec{w} = w^2 = (\Delta x)^2 + (\Delta y)^2 \qquad (A.10)$$

or

$$(\frac{w}{R})^2 = 16cos^2(\frac{\theta + \alpha_o}{2})sin^2(\frac{\phi - \phi_o}{2}). \qquad (A.11)$$

Appendix B

Evaluation of Θ_0, Θ_1, and Θ_2

The equivalent parameters defined in Chapter 4 are found by integration in the circumferential direction. This introduces three new variables, Θ_0, Θ_1, Θ_2 which are evaluated from the assumed ring model. Again in a more accurate vectorial representation, these values depend on the following integrals:

$$\Theta_1 = \int_0^\pi \frac{\dot{\vec{w}}'}{\dot{w}_o} \cdot \frac{\vec{w}'}{w_o} d\theta \tag{B.1}$$

$$\Theta_2 = \int_0^\pi \frac{\ddot{\vec{w}}}{\ddot{w}_o} \cdot \frac{\dot{\vec{w}}}{\dot{w}_o} d\theta \tag{B.2}$$

$$\Theta_0 = \int_0^\pi \frac{\vec{p}}{p_o} \cdot \frac{\dot{\vec{w}}}{\dot{w}_o} d\theta. \tag{B.3}$$

It was shown from Appendix A that the distribution of $w(\theta)$ depends on the central deflection of the ring. Hence, these integrals vary for each w_o or each x location of the cylinder. Once expressions are found for the product within the integrals, they can be numerically integrated in θ for a given w_o. The following sections derive expressions for the integrand.

B.1 Calculation of Θ_0

The value of Θ_0 depends on the magnitude and direction of the applied pressure. For example we will assume the following form for the non-dimensionalized pressure

$$\frac{\vec{p}}{p_o} = g(\theta)cos\theta\hat{i} + g(\theta)sin\theta\hat{j}, \tag{B.4}$$

where $g(\theta)$ describes the shape of presure distribution in the θ-direction. For simplicity, a step function is introduced

$$g(\theta) = \begin{cases} 1 & for \quad |\theta| \leq \theta_0 \\ 0 & for \quad |\theta| > \theta_0, \end{cases} \tag{B.5}$$

but other functions, such as a cosine could be used without difficulties.

With this definition of the pressure force, the calculation of Θ_o reduces to

$$\Theta_0 = \int_0^{\theta_o} (cos\theta\hat{i} + sin\theta\hat{j}) \cdot \frac{\dot{\vec{w}}}{\dot{w}_o} d\theta. \tag{B.6}$$

The integrand can be easily obtained using the expressions for the derivatives of the x and y components of $\vec{w}/R$ calculated Appendix A. Hence in the two regions, the integrand is given by the following expressions:

(i) $0 < \theta < (\pi - \alpha_o)/2$

The product is

$$\frac{\vec{p}}{p_o} \cdot \frac{\dot{\vec{w}}}{\dot{w}_o} = \frac{-[sin\beta cos(\alpha_o + \phi_o)cos(\phi + \theta) - sin(\frac{2\phi_o + \alpha_o - \theta}{2})sin(\beta + \frac{3\theta}{2})cos\phi]}{cos(\phi + \beta)cos(\alpha_o + \phi_o)}. \tag{B.7}$$

(ii) $(\pi - \alpha_o)/2 < \theta < \pi - \alpha_o$

The product is

$$\frac{\vec{p}}{p_o} \cdot \frac{\dot{\vec{w}}}{\dot{w}_o} = \frac{-sin\beta cos(\frac{\alpha_o + \theta}{2})cos(\phi + \phi_o - \frac{\alpha_o}{2} + \frac{3\theta}{2})}{cos(\alpha_o + \theta)cos(\phi + \beta)}. \tag{B.8}$$

B.2 Calculation of Θ_1

When dealing with a ring of unit width, it is not necessary to include the primes (which denote differentiation in x) in the product $\dot{\vec{w}}'/\dot{w}_o \cdot \vec{w}'/w_o$. The primes will be omitted henceforth.

The product $\dot{\vec{w}}/\dot{w}_o \cdot \vec{w}/w_o$ can be found by using that

$$\frac{\dot{\vec{w}}}{\dot{R}} \cdot \frac{\vec{w}}{R} = \frac{1}{2}\frac{\partial}{\partial t}[(\frac{w}{R})^2]. \tag{B.9}$$

Hence products can be found by taking the derivatives of the expressions calculated in the previous appendix, Eq. (A.7) and Eq. (A.11). These derivatives are again evaluated in the two regions.

(i) $0 < \theta < (\pi - \alpha_o)/2$

The product can be expressed as

$$\frac{\dot{\vec{w}}}{\dot{R}} \cdot \frac{\vec{w}}{R} = \frac{w\dot{w}}{R^2} = f_1\dot{\phi} + f_2\dot{\beta} \tag{B.10}$$

where

$$f_1 = 4cos^2(\alpha_o + \phi_o)sin(\phi - \phi_o)$$
$$-8cos(\alpha_o + \phi_o)sin(\frac{2\phi_o + \alpha_o - \theta}{2})sin(\frac{\beta - \beta_o}{2})sin(\frac{2\phi - \beta - \beta_o - \theta}{2}) \tag{B.11}$$

and

$$f_2 = 4sin^2(\frac{2\phi_o + \alpha_o - \theta}{2})sin(\beta - \beta_o)$$
$$-8cos(\alpha_o + \phi_o)sin(\frac{2\phi_o + \alpha_o - \theta}{2})sin(\frac{\phi - \phi_o}{2})sin(\frac{\phi + \phi_o - 2\beta - \theta}{2}). \tag{B.12}$$

However, $\dot{\beta}$ is related to $\dot{\phi}$ by Eq. (4.12), and Eq. (B.10) can be further expressed in terms of only $\dot{\phi}$

$$\frac{\dot{\vec{w}}}{\dot{R}} \cdot \frac{\vec{w}}{R} = (f_1 - \frac{f_2 cos\phi}{sin\beta})\dot{\phi}. \tag{B.13}$$

Note that $\dot{\vec{w}_o}/\dot{R} \cdot \vec{w_o}/R$ can be obtained by setting $\dot{\vec{w}}/\dot{R} \cdot \vec{w}/R(\theta = 0)$. Therefore,

$$\frac{\dot{\vec{w}}}{\dot{w}_o} \cdot \frac{\vec{w}}{w_o} = \frac{(f_1 - \frac{f_2 cos\phi}{sin\beta})}{(f_{10} - \frac{f_{20} cos\phi}{sin\beta})}, \tag{B.14}$$

where $f_{10} = f_1(\theta = 0)$ and $f_{20} = f_2(\theta = 0)$. Since the distribution of $\dot{\vec{w}}/\dot{w_o} \cdot \vec{w}/w_o$ in the θ-direction is a function of ϕ and β (both of which depend on w_o), it will vary for each deflection w_o.

(ii) $(\pi - \alpha_o)/2 < \theta < \pi - \alpha_o$

The product in this region is

$$\frac{\dot{\vec{w}}}{\dot{R}} \cdot \frac{\vec{w}}{R} = 4cos^2(\frac{\theta + \alpha_o}{2})sin(\phi - \phi_o)\dot{\phi}. \tag{B.15}$$

Hence,

$$\frac{\dot{\vec{w}}}{\dot{w}_o} \cdot \frac{\vec{w}}{w_o} = \frac{cos^2(\frac{\theta+\alpha_o}{2})}{cos^2(\frac{\alpha_o}{2})}. \tag{B.16}$$

B.3 Calculation of Θ_2

The product $\ddot{\vec{w}}/\ddot{w_o} \cdot \dot{\vec{w}}/\dot{w_o}$ can be found by using the following argument. Define a quantity $\bar{W}$

$$\overline{W} = \frac{\partial}{\partial t}(\frac{\dot{\vec{w}}}{R} \cdot \frac{\vec{w}}{R}). \tag{B.17}$$

But,

$$\frac{\partial}{\partial t}(\frac{\dot{\vec{w}}}{R} \cdot \frac{\vec{w}}{R}) = \frac{\dot{\vec{w}}}{R} \cdot \frac{\dot{\vec{w}}}{R} + \frac{\ddot{\vec{w}}}{R} \cdot \frac{\vec{w}}{R} \tag{B.18}$$

and after some algebra, one gets

$$\frac{\ddot{\vec{w}}}{R} \cdot \frac{\dot{\vec{w}}}{R} = \frac{(\frac{\dot{\vec{w}}}{R} \cdot \frac{\vec{w}}{R})(\frac{w}{R})^2 \overline{W} - (\frac{\dot{\vec{w}}}{R} \cdot \frac{\vec{w}}{R})^3}{(\frac{w}{R})^4}. \tag{B.19}$$

Most of the products on the right hand side of Eq. (B.19) were already calculated from previous analyses. All that is new is the quantity $\overline{W}$. Evaluation of $\overline{W}$ follows in two regions.

(i) $0 < \theta < (\pi - \alpha_o)/2$

We can express $\overline{W}$ in terms of complex functions, f_3 and f_4

$$\overline{W} = f_3 \dot{\phi}^2 + f_4 \ddot{\phi}. \tag{B.20}$$

These functions are defined by

$$f_3 = A - B\frac{cos\phi}{sin\beta} + C\frac{cos^2\phi}{sin^2\beta} + f_2[\frac{sin\phi}{sin\beta} - \frac{cos^2\phi cos\beta}{sin^3\beta}] \tag{B.21}$$

and

$$f_4 = f_1 - \frac{f_2 cos\phi}{sin\beta} \tag{B.22}$$

where,

$$A = 4cos^2(\alpha_o + \phi_o)cos(\phi - \phi_o)$$
$$-8cos(\alpha_o + \phi_o)sin(\frac{2\phi_o + \alpha_o - \theta}{2})sin(\frac{\beta - \beta_o}{2})cos(\frac{2\phi - \beta - \beta_o - \theta}{2}), \tag{B.23}$$

$$B = -8cos(\alpha_o + \phi_o)sin(\frac{2\phi_o + \alpha_o - \theta}{2})sin(\frac{2\phi - 2\beta - \theta}{2}), \tag{B.24}$$

and

$$C = 4sin^2(\frac{2\phi_o + \alpha_o - \theta}{2})cos(\beta - \beta_o)$$

$$+8cos(\alpha_o+\phi_o)sin(\frac{2\phi_o+\alpha_o-\theta}{2})sin(\frac{\phi-\phi_o}{2})cos(\frac{\phi+\phi_o-2\beta-\theta}{2}). \quad \text{(B.25)}$$

After substituting this result into Eq. (B.19), one gets

$$\frac{\ddot{\vec{w}}}{R}\cdot\frac{\dot{\vec{w}}}{R}=D\dot{\phi}^3+E\dot{\phi}\ddot{\phi} \quad \text{(B.26)}$$

where,

$$D=\frac{[f_1-\frac{f_2cos\phi}{sin\beta}][(\frac{w}{R})^2f_3-[f_1-\frac{f_2cos\phi}{sin\beta}]^2]}{(\frac{w}{R})^4} \quad \text{(B.27)}$$

and

$$E=\frac{[f_1-\frac{f_2cos\phi}{sin\beta}]f_4}{(\frac{w}{R})^2}. \quad \text{(B.28)}$$

The product $\ddot{\vec{w}}_o/R\cdot\dot{\vec{w}}_o/R$ can be calculated by setting $\theta=0$. Hence,

$$\frac{\ddot{\vec{w}}_o}{R}\cdot\frac{\dot{\vec{w}}_o}{R}=D_o\dot{\phi}^3+E_o\dot{\phi}\ddot{\phi}, \quad \text{(B.29)}$$

where D_o and E_o are D and E evaluated at $\theta=0$. Thus,

$$\frac{\ddot{\vec{w}}}{\ddot{w}_o}\cdot\frac{\dot{\vec{w}}}{\dot{w}_o}=\frac{D+E\frac{\ddot{\phi}}{\dot{\phi}^2}}{D_o+E_o\frac{\ddot{\phi}}{\dot{\phi}^2}}. \quad \text{(B.30)}$$

Notice that $\ddot{\vec{w}}/\ddot{w}_o\cdot\dot{\vec{w}}/\dot{w}_o$ now not only depends on w_o but also on the parameter $\ddot{\phi}/\dot{\phi}^2$.

(ii) $(\pi-\alpha_o)/2<\theta<\pi-\alpha_o$

$$\overline{W}=4cos^2(\frac{\theta+\alpha_o}{2})[\dot{\phi}^2cos(\phi-\phi_o)+\ddot{\phi}sin(\phi-\phi_o)] \quad \text{(B.31)}$$

Equation (B.31) is now substituted into Eq. (B.19) so that

$$\begin{aligned}\frac{\ddot{\vec{w}}}{R}\cdot\frac{\dot{\vec{w}}}{R}&=-sin(\phi-\phi_o)cos^2(\frac{\theta+\alpha_o}{2})\dot{\phi}^3\\&\quad+4cos^2(\frac{\phi-\phi_o}{2})cos^2(\frac{\theta+\alpha_o}{2})\dot{\phi}\ddot{\phi}.\end{aligned} \quad \text{(B.32)}$$

After setting $\theta = 0$, one finds

$$\frac{\ddot{\vec{w}}_o}{R} \cdot \frac{\dot{\vec{w}}_o}{R} = -sin(\phi - \phi_o)cos^2(\frac{\alpha_o}{2})\dot{\phi}^3 + 4cos^2(\frac{\phi - \phi_o}{2})cos^2(\frac{\alpha_o}{2})\dot{\phi}\ddot{\phi}. \tag{B.33}$$

Hence,

$$\frac{\ddot{\vec{w}}}{\ddot{w}_o} \cdot \frac{\dot{\vec{w}}}{\dot{w}_o} = \frac{-sin(\phi - \phi_o)cos^2(\frac{\theta+\alpha_o}{2}) + 4cos^2(\frac{\phi-\phi_o}{2})cos^2(\frac{\theta+\alpha_o}{2})\frac{\ddot{\phi}}{\dot{\phi}^2}}{-sin(\phi - \phi_o)cos^2(\frac{\alpha_o}{2}) + 4cos^2(\frac{\phi-\phi_o}{2})cos^2(\frac{\alpha_o}{2})\frac{\ddot{\phi}}{\dot{\phi}^2}}. \tag{B.34}$$

Again, $\ddot{\vec{w}}/\ddot{w}_o \cdot \dot{\vec{w}}/\dot{w}_o$ also depends on the parameter $\ddot{\phi}/\dot{\phi}^2$. A sensitivity analysis reveals that $\ddot{\vec{w}}/\ddot{w}_o \cdot \dot{\vec{w}}/\dot{w}_o$ depends very weakly on $\ddot{\phi}/\dot{\phi}^2$. For simplification, this ratio is taken as $\ddot{\phi}/\dot{\phi}^2 = 1.0$.

Appendix C

Calculation of the Impulse Velocity

When the response time of the shell is much longer than the loading time, the pressure pulse loading can be replaced by an impulsive loading. Under impulsive loading, the shell has no loads but is given an initial instantaneous velocity. The pressure load is thus introduced into the initial velocity of the shell. The pressure impulse is equated to the initial momentum of the shell

$$\int_0^{t_l}\int_0^{l_c}\int_0^{\pi} p(x,\theta,t)d\theta dx dt = \int_0^{l_c}\int_0^{\pi} m\dot{w}(x,\theta,t)d\theta dx, \tag{C.1}$$

where t_l is the loading time and l_c represents the extent of pressure loading on the unstiffened shell or the distance between stiffeners for the stiffened shell. Equation (C.1) reduces to

$$\int_0^{\infty}\int_0^{l_c} \bar{p}(x)e^{\frac{-t}{\tau}}dx dt = \bar{m}\bar{V}\int_0^{l_c} f(x)dx, \tag{C.2}$$

where $\bar{V}$ is the impulse velocity. Notice that the equivalent parameters are introduced. Denoting the impulse as $\bar{I} = \int_0^{l_c} \tau\bar{p}(x)dx$, one finds the corresponding initial velocity as

$$\bar{V} = \frac{\bar{I} l_c}{\bar{m} \int_0^{l_c} f(x) dx}. \tag{C.3}$$

Appendix D

A Special Orthogonality Condition

The following analysis derives an expression for the special orthogonality condition for the partial differential system given in Chapter 8 with the accelerating boundary at $x = 1$.

The reduced eigenvalue problem for the partial differential equation is

$$w'' + \lambda_n^2 w = 0, \tag{D.1}$$

with the prescribed boundary conditions

$$w'(0) = 0 \tag{D.2}$$

and

$$-\lambda_n^2 w(1) + \frac{2}{\eta} w'(1) = 0. \tag{D.3}$$

Denote the solutions, $w_1 = w(\lambda_1)$ and $w_2 = w(\lambda_2)$. After setting $w = w_1$ in Eq. (D.1), multiplying the entire equation by w_2, and integrating over the interval 0 to 1, one finds that

$$\int_0^1 (w_1'' w_2 + \lambda_1^2 w_1 w_2) dx = 0. \tag{D.4}$$

Then, upon integrating $w_1'' w_2$ twice by parts and using Eqs. (D.2) and (D.3) to

evaluate the boundary conditions, one gets

$$(\lambda_2^2 - \lambda_1^2)[\int_0^1 w_1 w_2 dx + \frac{\eta}{2} w_1(1) w_2(1)] = 0. \tag{D.5}$$

Hence, for $\lambda_1 \neq \lambda_2$,

$$\int_0^1 w_1 w_2 dx + \frac{\eta}{2} w_1(1) w_2(1) = 0. \tag{D.6}$$

Equation (D.6) defines the orthogonality condition that must be satisfied for the eigenvalue problem specified by Eqs. (D.1)-(D.3). Notice that this orthogonality condition is not one in a classical sense because it describes a moving boundary condition and not one that is fixed (commonly found in the literature).

Appendix E

Evaluation of Fourier Coefficients

The variable J_n is used to represent either G_n and F_n in Chapter 8. The Fourier coefficients J_n using the special orthogonality condition are represented as

$$\sum_{n=0}^{\infty} J_n cos(\lambda_n x) = f(x), \tag{E.1}$$

where λ_n are the eigenvalues and $f(x)$ is any function. It is understood that in Eq. (E.1) the first eigenvalue is zero, $\lambda_0 = 0$. Therefore, Eq. (E.1) may be more conveniently expressed as

$$J_0 + \sum_{n=1}^{\infty} J_n cos(\lambda_n x) = f(x). \tag{E.2}$$

Equation (E.1) is multiplied by $cos\lambda_m x$ and intergrated from 0 to 1

$$\sum_{n=0}^{\infty} \int_0^1 J_n cos(\lambda_n x) cos(\lambda_m x) dx = \int_0^1 f(x) cos(\lambda_m x) dx. \tag{E.3}$$

The special orthogonality condition Eq. (D.6) may now be introduced into Eq. (E.3) such that

$$\sum_{n=0}^{\infty} J_n [\int_0^1 cos(\lambda_n x) cos(\lambda_m x) dx + \frac{\eta}{2} cos\lambda_n cos\lambda_m] - \sum_{n=0}^{\infty} J_n \frac{\eta}{2} cos\lambda_n cos\lambda_m = \int_0^1 f(x) cos(\lambda_m x) dx. \tag{E.4}$$

Notice that in using the orthogonality condition derived in Appendix D only the terms for which $n = m$ are non-zero under the first summation. Therefore,

$$J_m[\int_0^1 cos^2(\lambda_m x)dx + \frac{\eta}{2}cos^2\lambda_m] - \sum_{n=0}^{\infty} J_n \frac{\eta}{2} cos\lambda_n cos\lambda_m = \int_0^1 f(x)cos(\lambda_m x)dx. \quad \text{(E.5)}$$

However, by evaluating Eq. (E.1) at $x = 1$, one finds that

$$\sum_{n=0}^{\infty} J_n cos\lambda_n = f(1). \quad \text{(E.6)}$$

After substituting Eq. (E.6) into Eq. (E.5) and performing the necessary integration, one gets

$$J_m = \frac{[\int_0^1 f(x)cos(\lambda_m x)dx + \frac{\eta}{2}cos\lambda_m f(1)]}{[\frac{1}{2}(1 + \frac{sin2\lambda_m}{2\lambda_m}) + \frac{\eta}{2}cos^2\lambda_m]} \quad \text{for } m = 1, 2, 3, ... \quad \text{(E.7)}$$

Similarly, it may be shown that for $m = 0$,

$$J_0 = \frac{2[\int_0^1 f(x)dx + \frac{\eta}{2}f(1)]}{[2 + \eta]}. \quad \text{(E.8)}$$

Appendix F

Lumped Mass $\bar{M}$ and Bending Resistance $\bar{Q}$

Calculations of the lumped mass $\bar{M}$ and foundation force $\bar{Q}$ that represent the T-stiffener, depend on the extent of the shell which will be used for the stiffener, $2l_1$, as well as the shifting of the neutral axis (explained in Chapter 8). The length l_1 is left as free parameter that can be used to describe an effective width effect of the stiffener. A lower bound of l_1 would be the width of the web $t_w/2$. The initial values for $\bar{M}$ and $\bar{Q}$ (before deformation) are derived here.

The lumped mass for the stiffener shown in Figure F-1 is simply

$$\bar{M} = 2\pi\rho R\Theta_2[h_f t_f + h_w t_w + 2hl_1]. \tag{F.1}$$

The lumped bending resistance is more complicated because the neutral axis must first be evaluated. Depending on the stiffener dimensions, the position of the neutral axis may be represented for the two cases shown in Fig. F-1. Case A occurs for large stiffeners and Case B for very small ones. Following the rigid-plastic material assumption, the neutral axes h_{NA} for the two cases are the following:

F.1 Case A : $h_{NA} > h$

The neutral axis in this case is

$$h_{NA} = \frac{h_f t_f + (h_w + 2h)t_w - 2hl_1}{2t_w}. \tag{F.2}$$

After taking moments about this axis, one finds that the total bending moment is

$$M = \sigma_o[h_f t_f(\frac{t_f}{2} + h_w + h - h_{NA}) + \frac{t_w}{2}(h_w + h - h_{NA})^2 + \frac{t_w}{2}(h_{NA} - h)^2 + 2hl_1(h_{NA} - \frac{h}{2})]. \tag{F.3}$$

The total bending moment is used to calculate the bending resistance

$$\bar{Q} = 8\sigma_o[h_f t_f(\frac{t_f}{2} + h_w + h - h_{NA}) + \frac{t_w}{2}(h_w + h - h_{NA})^2 + \frac{t_w}{2}(h_{NA} - h)^2 + 2hl_1(h_{NA} - \frac{h}{2})]/R. \tag{F.4}$$

F.2 Case B : $h_{NA} < h$

The neutral axis in this case is

$$h_{NA} = \frac{h_f t_f + h_w t_w + 2hl_1}{4l_1}. \tag{F.5}$$

Again moments are taken about this axis

$$M = \sigma_o[h_f t_f(\frac{t_f}{2} + h_w + h - h_{NA}) + t_w h_w(\frac{h_w}{2} + h - h_{NA}) + l_1(h - h_{NA})^2 + h_{NA}^2 l_1] \tag{F.6}$$

and hence,

$$\bar{Q} = 8\sigma_o[h_f t_f(\frac{t_f}{2} + h_w + h - h_{NA}) + t_w h_w(\frac{h_w}{2} + h - h_{NA}) + l_1(h - h_{NA})^2 + h_{NA}^2 l_1]/R. \tag{F.7}$$

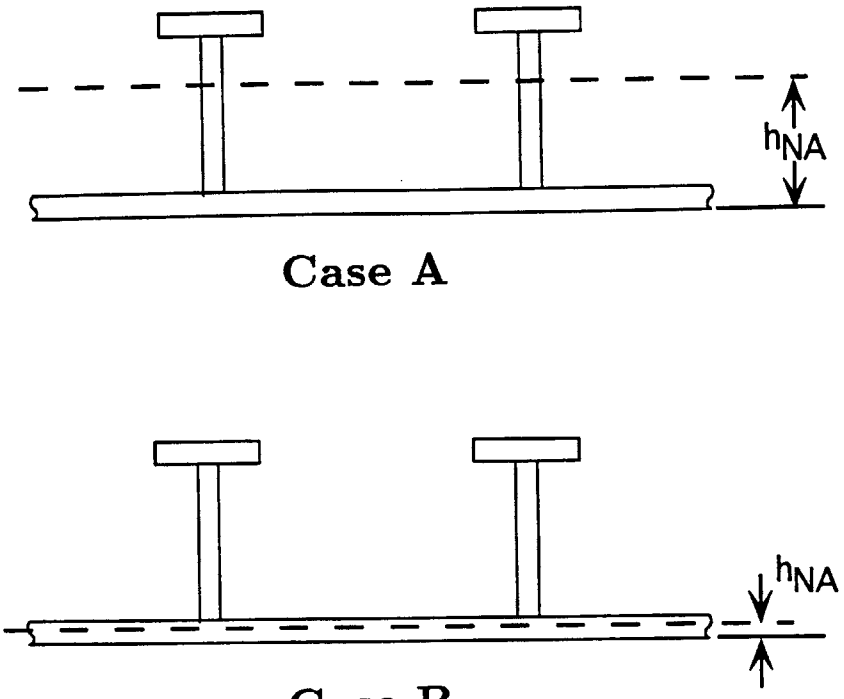

Figure F-1: Location of the neutral axis for T-stiffeners.

Appendix G

Equivalent Thicknesses Based on Inertia and Bending Work

An equivalent inertia resistance can be found by smearing the ring stiffeners so that the shell is replaced by one of equivalent thickness, h_i. The foot of the stiffener is given by $2l_1 = t_w$. For the T-stiffened shell, h_i is found by setting the mass of a representative length of the stiffened shell (taken here to be the length of the bay) equal to an unstiffened shell of equal length but with an elevated thickness. An equation for h_i is

$$h_i = \frac{2hl + h_w t_w + h_f t_f}{2l}. \tag{G.1}$$

The same idea is used to calculate the equivalent thickness due to additional bending resistance of the stiffener. The total bending moment of the stiffened shell M_b is set equal to the total bending moment of the bay

$$M_b = \frac{\sigma_o h_b^2}{4} t_w. \tag{G.2}$$

Again the neutral axis must first be found to calculate M_b. For the perfectly plastic, T-stiffener shown in Fig. F-1 (Case A), the neutral axis is given by

$$h_{NA} = \frac{(h + h_w)t_w + h_f t_f}{2t_w}. \tag{G.3}$$

The total bending moment associated with the circumferential direction may now be taken about h_{NA}

$$M_b = \sigma_o[\frac{h_{NA}^2}{2}t_w + \frac{(h + h_w - h_{NA})^2}{2}t_w + t_f h_f(\frac{t_f}{2} + h + h_w - h_{NA})]. \qquad \text{(G.4)}$$

Upon equating Eq. (G.2) to Eq. (G.5),

$$h_b = 2\sqrt{[\frac{h_{NA}^2}{2} + \frac{(h + h_w - h_{NA})^2}{2} + \frac{t_f h_f}{t_w}(\frac{t_f}{2} + h + h_w - h_{NA})]}. \qquad \text{(G.5)}$$

Bibliography

[1] H. E. Lindberg and A. L. Florence. Dynamic pulse buckling: Theory and experiment. Technical Report 6503H, Defense Nuclear Agency, Washington, DC, 1983.

[2] T. A. Duffey. Dynamic rupture of shells. In *Structural Failure, edited by T. Wierzbicki and N. Jones*, pages 161–192. Wiley and Sons, 1989.

[3] J. Huang and T. Wierzbicki. Plastic tripping of ring stiffeners. To be published in Journal of Structural Engineering, Proc. ASCE., 1992.

[4] D. E. Grady and M. Kipp. Fragmentation of solids under dynamic loading. In *Structural Failure, edited by T. Wierzbicki and N. Jones*, pages 1–40. Wiley and Sons, 1989.

[5] T. Wierzbicki and M. S. Suh. Indentation of tubes under combined loading. *Int. J. Mech. Sci.*, 30:229–248, 1987.

[6] M. S. Hoo Fatt and T. Wierzbicki. Denting analysis of ring stiffened cylindrical shells. *International Journal of Offshore and Polar Engineering*, 1(2):137–145, 1991a.

[7] T. Wierzbicki and M. S. Hoo Fatt. Deformation and perforation of a circular membrane due to rigid projectile impact. In *the Proc. of Symp. on the Dynamic Response of Structures to High-Energy Excitations, 112th ASME Winter Annual Meeting*, volume PVP-225, pages 73–83, Atlanta, Georgia, December 1-6 1991.

[8] W. J. Schuman. The response of cylindrical shells to external blast loading. Technical Report 1461, Ballistic Research Laboratories, March 1963.

[9] J. A. DeRuntz and F. A. Brogan. Underwater shock analysis of nonlinear structures: A reference manual for the USA-STAGS code (Version 3). *Report DNA 5545F*, 1980.

[10] G. F. Carrier. The interaction of an acoustic wave and an elastic cylindrical shell. *Brown University Technical Report No. 4*, 1951.

[11] R. D. Mindlin and H. H. Bleich. Response of an elastic cylindrical shell to a transverse step shock wave. *J. Appl. Mech.*, 20:189–195, 1953.

[12] M. L. Baron. The response of a cylindrical shell to a transverse shock wave. In *the Proceedings of the Second U. S. National Congress of Applied Mechanics*, pages 201–212, 14-18 June 1954.

[13] W. W. Murray. Interaction of a spherical acoustic wave with a beam of circular cross section. *Underwater Explosion Research Division Report 1-55*, June 1955.

[14] R. G. Payton. Transient interaction of an acoustic wave with a circular cylindrical elastic shell. *J. Acoust. Soc. Am.*, 32:722–729, 1960.

[15] R. S. Haxton and J. H. Haywood. Linear elastic response of a ring stiffened cylinder to underwater explosion loading. In *Advances in Marine Structure, edited by C. S. Smith and J. D. Clarke*, pages 366–389. Elsevier Applied Science Publishers, London, 1986.

[16] R. S. Haxton, J. H. Haywood, and I. T. Hunter. Nonlinear inelastic response of an infinite cylindrical shell to underwater shock wave loading. In *Advances in Marine Structure, edited by C. S. Smith and J. D. Clarke*, pages 334–351. Elsevier Applied Science Publishers, London, 1991.

[17] W. J. Schuman. Theoretical calculation of iso-damage characteristics. Technical Report TR-10, J. G. Eng. Res Assoc., February 1970.

[18] H. Huang. An exact analysis of the transient interaction of acoustic plane waves with a cylindrical elastic shell. *J. Appl. Mech.*, 37:1091–1106, 1970.

[19] T. L. Geers. Excitation of an elastic cylindrical shell by a transient acoustic wave. *J. Appl. Mech.*, 36:459–469, 1969.

[20] T. L. Geers. Scattering of a transient acoustic wave by an elastic cylindrical shell. *J. Acoust. Soc. Am.*, 51:1640–1651, 1972.

[21] T. L. Geers and C.-L. Yen. Inelastic response of an infinite cylindrical shell to transient acoustic waves. *J. Appl. Mech.*, 56:900–909, 1989.

[22] P. R. Gefken, S. W. Kirkpatric, and B. S. Holmes. Response of impulsively loaded cylindrical shells. *Int. J. Impact Engng.*, 7(2):213–228, 1988.

[23] W. Stronge. Impact on metal tubes: Indentation and perforation. In *Structural Crashworthiness and Failure, edited by N. Jones and T. Wierzbicki.* Elsevier Science Publishers, 1993.

[24] G. G. Corbett, S. R. Reid, and S. T. S. Al-Hassani. Static and dynamic penetration of steel tubes by hemispherically nosed punches. *Int. J. Impact Engng.*, 9(2):105–190, 1990.

[25] S. W. Kirkpatrick and B. S. Holmes. Structural response of thin cylindrical shells to impulsive external loads. *AIAA Journal*, 26(1):96–103, 1988.

[26] V. C. Prantil, S. W. Kirkpatrick, B. S. Holmes, and J. O. Hallquist. Response of a very thin shell under and impulsive load. In *the Finite Element Methods for Plate and Shell Structures 2: Formulations and Algorithms, edited by T. J. R. Hughes and E. Hinton.* Pineridge Press, Swansea, U.K., 1986.

[27] B. S. Holmes, Kirkpatrick S. W., and J. W. Simons. Application of material failure models to structural problems. In *Structural Crashworthiness and Failure, edited by N. Jones and T. Wierzbicki.* Elsevier Science Publishers, 1993.

[28] K. V. Trinh and J. D. Gruda. Failure resistance of thin shells against projectile penetration. In *the Proc. ASME 1991, Pressure Vessel and Piping Conference*, June 1991.

[29] D. J. Bammann, M. L. Chiesa, M. F. Horstemeyer, and Weingarten L. I. Failure in ductile materials using finite element methods. In *Structural Crashworthiness and Failure, edited by N. Jones and T. Wierzbicki.* Elsevier Science Publishers, 1993.

[30] J. P. Den Hartog. *Advanced Strength of Materials.* McGraw-Hill, New York, 1952.

[31] C. R. Calladine. Thin-walled elastic shells analysed by a Rayleigh method. *Int. J. Sol. Struct.*, 13:515–530, 1977.

[32] S. R. Reid. Influence of geometrical parameters on the mode of collapse of a "pinched" rigid-plastic cylindrical shell. *Int. J. Sol. Struct.*, 14:1027–1043, 1978.

[33] T. X. Yu and W. Stronge. Large deflection of a rigid-plastic beam-on-foundation from impact. *Int. J. Impact Engng.*, 9:115–126, 1990.

[34] W. J. Stronge. Impact and perforation of cylindrical shells by blunt missiles. In *Metalforming and Impact Mechanics, edited by S.R. Reid.* Pergamon Press, Oxford, 1985.

[35] A. Gurkok and H. G. Hopkins. The effect of geometry changes on the load carrying capacity of beams under transverse load. *SIAM J. Appl. Math*, 25(3):500–521, 1973.

[36] K. A. Rakhmatulin. On propagation of unloading waves [in Russian]. *Prikl. Mat. Mekh*, 9:1, 1945.

[37] N. Cristescu. *Dynamic Plasticity.* North Holland, Amsterdam, 1967.

[38] R. R. Rosales, M. S. Hoo Fatt, and T. Wierzbicki. Large amplitude plastic wave propagation in a string-on-foundation caused by mass impact. To be submitted to the Quarterly of Applied Mathematics, 1992.

[39] T. Wierzbicki and M. S. Hoo Fatt. Impact response of a string-on-foundation. *Int. J. Impact Engng.*, 12(1):21–36, 1992.

[40] M. S. Hoo Fatt and T. Wierzbicki. Impact damage of long plastic cylinders under dynamic pressure loading. In *the Proceeding of the First International Conference of Offshore and Polar Engineering*, volume IV, pages 172–182, Edinburgh, Scotland, 11-15 August 1991.

[41] C. B. Sweeney. Post-perforation analysis of subordnance projectile impact on thin flat plates. Master's thesis, Massachusetts Institute of Technology, 1992.

[42] M. Suliciu, M. S. Hoo Fatt, and T. Wierzbicki. Large deflection dynamic plastic response of long cylinders under local pressure pulse. To be submitted to the Int. J. Impact Engng., 1992.

[43] A. Onoufriou and J. E. Harding. Residual strength of damaged ring-stiffened cylinders. In *the Proc. 4th Int. Symp. Offshore Mech. and Arctic Eng.*, volume 2, pages 537–545, Houston, Texas, 1985.

[44] A. S. Onoufriou, A. S. Elnashai, J. E. Harding, and P. J. Dowling. Numerical modeling of ring stiffened cylinder denting. In *the Proc. 6th Int. Offshore Mech and Arctic Eng. Symp.*, volume 1, pages 281–289, Houston, Texas, 1987.

[45] B. F. Ronalds and P. J. Dowling. A denting mechanism for orthogonally stiffened cylinders. *Int. J. Mech. Sci.*, 29(10/11):743–759, 1987.

[46] M. S. Hoo Fatt and T. Wierzbicki. Damage of ring-stiffened cylinders under pressure loading. In *the Proceedings of the Second International Offshore and Polar Engineering Conference*, San Francisco, June 14-19 1992.

[47] W. McDonald. Experimental results of a ring-stiffened shell undergoing underwater explosive loading. Private Communications, 1992.

[48] M. Moussouros, M. S. Hoo Fatt, and T. Wierzbicki. Effect of shear on the plastic denting of cylinders. To be submitted to Int. J. Mech. Sci., 1992b.

[49] M. S. Suh. *Plastic Analysis of Dented Tubes Subjected to Combined Loading.* PhD thesis, Massachusetts Institute of Technology, 1987.

[50] T. Wierzbicki and W. Abramowicz. On the crushing mechanics of thin walled structures. *J. Appl. Mech.*, 50:727–734, 1983.

[51] M. S. Hoo Fatt and T. Wierzbicki. Damage of plastic cylinders under localized pressure loading. *Int. J. Mech. Sci.*, 33(12):999–1016, 1991b.

[52] M. Moussouros and M. S. Hoo Fatt. Static rigid-plastic analysis of unstiffened cylindrical shells. Part 4: Model No. 4 for the cylinder. *NSWCDD/TR-92/188*, 1992a.

[53] J. A. DeRuntz and P. G. Hodge. Crushing of tubes between rigid plates. *J. Appl. Mech.*, 30:391–395, 1963.

[54] N. Jones. Plastic failure of ductile beams loaded dynamically. *J. Engng. for Industry*, 98 (B):131–136, 1976.

[55] T. Moan. Loads and safety of marine structures. NIF-Course at the Norwegian Institute of Technology, January 7-9 1985.

[56] J. De Oliveira, T. Wierzbicki, and W. Abramowicz. Plastic behavior of tubular members under lateral concentrated loading. Technical Report 82-0708, DnV, July 1982.

[57] J. K. Paik. Damage estimation for offshore tubular members under quasi-static loading. *J. Society Naval Architect of Korea*, 26(4):81–93, 1989.

[58] R. H. Cole. *Underwater Explosions.* Dover Publications Inc., New York, 1948.

[59] J. B. Martin and P. S. Symonds. Mode approximations for impulsively loaded rigid-plastic structures. *J. Engng. Mech. Div., Proc. ASCE*, 92(EM5):43–66, 1966.

[60] N. Jones. *Structural Impact.* Cambridge University Press, U.K., 1990.

[61] H. A. Schade. The effective breadth concept in ship structure design. *Trans. SNAME*, 61:410–430, 1953.

[62] J. M. Kelly and T. Wierzbicki. Motion of a circular viscoplastic plate subject to projectile impact. *J. Appl. Math. Phys.(ZAMP)*, 18:236–246, 1967.

[63] F. A. McClintock. Other possible mechanisms for the stiffened shell. Private Communications, 1992.